Tatjana Djurić

Molecular crystals on crystalline surfaces: examples of organic rod-like and plate-like molecules

DOCTORAL THESIS

For obtaining the academic degree of
Doktor der technischen Wissenschaften

Doctoral Programme of Technical Sciences
Technical Physics

Graz University of Technology

Supervisor:

Ao.Univ.-Prof. Dipl.-Ing. Dr.techn. Roland Resel
Institute of Solid State Physics

Graz, April 2012

Deutsche Fassung:
Beschluss der Curricula-Kommission für Bachelor-, Master- und Diplomstudien vom 10.11.2008
Genehmigung des Senates am 1.12.2008

EIDESSTATTLICHE ERKLÄRUNG

Ich erkläre an Eides statt, dass ich die vorliegende Arbeit selbstständig verfasst, andere als die angegebenen Quellen/Hilfsmittel nicht benutzt, und die den benutzten Quellen wörtlich und inhaltlich entnommene Stellen als solche kenntlich gemacht habe.

Graz, am ……………………………   …………………………………………………..
(Unterschrift)

Englische Fassung:

STATUTORY DECLARATION

I declare that I have authored this thesis independently, that I have not used other than the declared sources / resources, and that I have explicitly marked all material which has been quoted either literally or by content from the used sources.

……………………………   …………………………………………………..
date   (signature)

Mojim roditeljima
i Ferdinandu.

Acknowledgements

The years I have spent working on my PhD studies comprise much more experience and insights than can be reflected in this thesis. This work was possible only by close collaboration and discussions with many others.

I want to thank Mike Ramsey and his student Thomas Ules who prepared great samples and have performed the LEED measurements. They have always been open to discussions and willing to respond to my every question - they make a great team to work with.

Many thanks to Christian Teichert, Gregor Hlawacek, Quan Shen and Harald Plank for their nice AFM measurements and the dedicated discussions - they have been an important link to the *real* space.

During my stay in Strasbourg in the group of Martin Brinkmann, I was captivated by his enthusiasm of being a TEM microscopist. I am grateful for his willingness to teach me his knowledge. I want to thank his student Lucia Hartmann for spending nice breakfasts, lunches and dinners with me - and for sneaking me into French-guided aerobic classes.

It was a pleasure to work with Clemens Simbrunner; his candid character contributed to a very fruitful collaboration and also to many interesting off-topic conversations.

I have truly enjoyed the great atmosphere in this working group. I am pleased to have become acquainted with Markus Koini, Oliver Werzer, Heinz-Georg Flesch, Armin Moser, Karolf Marguc, Jirí Novák, Alfred Neuhold, Markus Neuschitzer, Reinhold Hetzel, Michael Dohr and Alexander Pichler - you have lightened and brightened my everyday work and after-work time. Because of you, entering the office often was like starting a philosophic journey through $\boldsymbol{k}$-space and time. I want to thank Alfred and in particular Armin who has been my companion for the longest time. I am grateful for their instantaneous help whenever I needed it.

My biggest thanks go to my supervisor Roland Resel. I have enjoyed his patient and courteous manner, and I particularly appreciate his outside-the-box thinking. He enabled my FWF funding and made many conference visits possible. Above all, he gave me space to find my own way of working - and he was always there for any kind of concerns.

Abstract

Understanding and controlling the molecular orientation and crystallographic structure of organic thin films is not only interesting from a scientific point of view, but also of a particular importance for applications in electronic devices. The weak van-der-Waals interactions between organic molecules render different molecular packings equally likely and give rise to highly pronounced polymorphism in organic crystals. The present work elucidates the determinants for the specific phases and molecular orientations occurring in organic thin films. To this aim, thermally deposited thin films of a variety of organic *small-molecules* are investigated on various substrates.

On the first example of *tetraphenyl-porphyrin* molecules substrate selected polymorphism is demonstrated. By selecting two different substrate surfaces (KCl(100) and Cu(110)-(2x1)O) it is shown that the substrate surface determines not only the molecular arrangement but also the polymorphic phase that grows on it. For *pentacene* thin films grown on identical substrates (Cu(110)) distinctively different structural properties were observed: films crystallizing either in the “thin film” phase with standing molecules or in the “single crystal” phase with lying molecules (see Chapter 6). By studying the evolution of the film structure from the mono- to the multilayer regime it is shown, that there not the substrate but subtle differences in the monolayer structures are decisive for the specific alignment of the molecules. A more complex system results from alternate deposition of *α-sexithiophene* and *para-hexaphenyl* molecules on muscovite mica(001) surface. Even for a stack of 120 alternate layers no phase-mixing occurs and the molecules crystallize in their respective equilibrium structures. Furthermore, the two molecular species align parallel with their long molecular axes which leads to a perfect adoption of their herringbone packings. Finally, also an all-organic heterostructure is presented, namely bilayer films composed of *zinc-phthalocyanine* and fullerene C_{60} on polycarbonate alignment layers. By adjusting the substrate temperature during the thin film deposition, different zinc-phtalocyanine polymorphs were obtained and their impact on the interface structure of the C_{60}/zinc-phthalocyanine heterostructures was elucidated.

Kurzfassung

Ein detailiertes Verständnis des Kristallisationsverhaltens sogenannter organischer *small molecules* in dünnen Schichten, ist nicht nur aus der wissenschaftlichen Perspektive erstrebenswert. Vielmehr kann durch gezielte Kontrolle der Kristallisation ein effizienter Einsatz dünner Schichten in organischer Elektronik ermöglicht werden. Da zwischen Molekülen eines Molekülkristall nur schwache Van-der-Waals-Kräfte wirken, können sich verschiedene, energetisch vergleichbar günstige, Kristallstrukturen ausbilden (Polymorphismus). Dieses Phänomen ist wesentlich für die Orientierung der Moleküle in Bezug auf die Substratoberfläche mitbestimmend. Im Rahmen dieser Dissertation wird untersucht, welche Faktoren für die Ausbildung einer bestimmten Kristallstruktur sowie ihrer spezifischen Ausrichtung bezüglich der Substratoberfläche entscheidend sind. Zu diesem Zweck, wurden dünne Schichten anwendungsrelevanter Moleküle aus der Gasphase auf verschiedenen Substratoberflächen aufgebracht und auf ihre kristallographischen sowie morphologischen Eigenschaften untersucht.

Zuerst wurden dünne Schichten des Moleküls *Tetraphenyl-Porphyrin* diskutiert. Es wird gezeigt, dass die verwendeten anorganischen Substratoberflächen nicht nur die Molekülorientierung auf der Substratoberfläche determinieren sondern darüber hinaus auch die energetisch günstigste polymorphe Phase bestimmen. Am Beispiel des Moleküls *Pentacen* wird aufgezeigt, dass es prinzipiell möglich ist am demselben Substrat kristallographisch unterschiedliche dünne Schichten zu wachsen: sowohl Filme in der "thin film" Phase mit aufrechter Molekülorientierung als auch Filme in der "single crystal" Phase mit liegender Molekülorientierung wurden untersucht und der Grund ihrer Entstehung diskutiert. Noch komplexere Systeme entstehen durch Mischung von Materialien zu organischen Heterostrukturen. Dünne Schichten des Moleküls α-*Sexithiophene*, welche auf dünnen Schichten des Moleküls *Para-hexaphenyl* (die ihrerseits wiederum auf Glimmer(001) aufgebracht wurden) wurden untersucht. Es konnte gezeigt werden, dass selbst in Heterostrukturen die aus 120 alternierenden Schichten bestehen, die Moleküle phasenseparieren und in ihren jeweiligen Gleichgewichtsstrukturen kristallisieren. Vielmehr, bleibt die relative Molekülorientierung durch alle 120 Schichten hindurch erhalten. Die Arbeit schließt mit der Diskussion eines Vielkomponenten-System, das ausschließlich aus organischen Verbindungen besteht. Eine nanostrukturierte Polycarbonat-Oberfläche dient als Substrat für das Wachstum dünner Schichten des Moleküls *Zink-Pththalocyanin*, auf welche wiederum Schichten des Moleküls Fulleren verdampft wurden. Es wird gezeigt wie die Temperatur des Substrats den Polymorphismus der darauf absorbierten Heterostruktur bestimmt.

Contents

I Thin films of organic small molecules - An Introduction 1

1 Organic Semiconductors 3
- 1.1 Organic Field Effect Transistors 4
- 1.2 Organic Photovoltaics 4
- 1.3 Importance of the structure 6

2 Organic molecular crystals 9
- 2.1 Basics of crystallography 9
- 2.2 Peculiarities of molecular crystals 11
- 2.3 Polymorphism 13
- 2.4 Polymorphism of molecules under study 15
  - 2.4.1 Pentacene 15
  - 2.4.2 α-Sexithiophene and para-Hexaphenyl 17
  - 2.4.3 Tetraphenyl-porphyrins 18
  - 2.4.4 Phthalocyanines 19
  - 2.4.5 Fullerene C_{60} 21

3 Epitaxy 23
- 3.1 Epitaxy of organic molecules 23
  - 3.1.1 Modes of epitaxy 24
- 3.2 Fabricating thin films 26
  - 3.2.1 Physical vapour deposition 26
  - 3.2.2 Hot Wall Epitaxy 26

4 Investigation of crystallographic properties 29
- 4.1 Diffraction theory 29
  - 4.1.1 Laue equations 29
  - 4.1.2 Reciprocal lattice 32
  - 4.1.3 Bragg equation 33
- 4.2 X-Ray diffraction 34
  - 4.2.1 Specular scans 34
  - 4.2.2 Pole figure measurement 35
- 4.3 Transmission electron microscopy 37
  - 4.3.1 Imaging modes 38

II Results 41

5 Substrate selected polymorphism of epitaxially aligned tetraphenyl-porphyrin thin films 43
- 5.1 Introduction 44
- 5.2 Experimental section 46
  - 5.2.1 Sample preparation 46
  - 5.2.2 Low energy electron diffraction measurements 46
  - 5.2.3 X-ray diffraction measurements 47
  - 5.2.4 Transmission electron diffraction measurements 47
  - 5.2.5 Atomic Force Microscopy Measurements 47
- 5.3 Results 48
  - 5.3.1 Powder diffraction 48
  - 5.3.2 Structure and alignment of tetraphenyl-porphyrins on KCl(100) 50
  - 5.3.3 Structure and Alignment of Tetraphenyl-Porphyrins on Cu(110)-(2x1)O 56
- 5.4 Discussion 61
- 5.5 Conclusions 63

6 Epitaxially grown films of standing and lying pentacene molecules on Cu(110) surfaces 65
- 6.1 Introduction 65
- 6.2 Experimental Section 67
  - 6.2.1 Sample preparation 67
  - 6.2.2 X-ray diffraction measurements 68
  - 6.2.3 Atomic force measurements 69
- 6.3 Results 69
  - 6.3.1 Upright Pentacene Films 69
  - 6.3.2 Lying Pentacene Films 71
  - 6.3.3 Monolayer Base for Upright Molecules 72
  - 6.3.4 Monolayer Base for Lying Molecules 72
  - 6.3.5 Film morphologies 73
- 6.4 Discussion 74
- 6.5 Conclusion 76

7 Periodically deposited heterostructures of α-sexithiophene/para-hexaphenyl thin films on muscovite mica(001) surfaces: crystallographic structure and morphology 77
- 7.1 Introduction 78
- 7.2 Experimental Section 80
  - 7.2.1 Sample preparation 80
  - 7.2.2 X-ray diffraction measurements 81
  - 7.2.3 Transmission electron microscopy 81
  - 7.2.4 Atomic force microscopy 82
- 7.3 Results 82
  - 7.3.1 Growth of α-6T molecules on p-6P template layers 82

7.3.2 Periodic α-6T/p-6P multilayer heterostructures 87
7.4 Conclusions 95

8 Impact of zinc phthalocyanine polymorphism on the interface structure of C_{60}/ZnPc heterojunctions 97
8.1 Introduction 98
8.2 Experimental 98
8.2.1 Preparation of bisphenol A polycarbonate alignment layers 98
8.2.2 Deposition of ZnPc/C_{60}-bilayers 99
8.2.3 Investigation techniques 100
8.3 Results 101
8.3.1 Case 1 – ZnPc: T_{sub}= 115 °C, C_{60}: T_{sub}= 115 °C 101
8.3.2 Case 2 – ZnPc: T_{sub}= 170 °C, C_{60}: T_{sub}= 115 °C 104
8.3.3 Case 3 – ZnPc: T_{sub}= 200 °C, C_{60}: T_{sub}= 115 °C 106
8.3.4 Case 4 – ZnPc: T_{sub}= 200 °C, C_{60}: T_{sub}= 200 °C 108
8.4 Summary 110

Bibliography 111

Part I

Thin films of organic small molecules - An Introduction

Chapter 1

Organic Semiconductors

Due to their delocalized π-electrons, conjugated small molecules and polymers (macro-molecules) have become subject to extensive research in the field of semiconductors. Just like in inorganic materials, organic semiconductors (OSC) are classified into hole (p-type) and electron (n-type) carriers. However, the vast majority organic molecules shows p-type behaviour. Having a significantly lower charge carrier mobility (highest mobility is measured rubrene single crystals: 40 $cm^2V^{-1}s^{-1}$), organic molecules are not aimed to replace their inorganic counterparts (Si at 300 K: 1500 $cm^2V^{-1}s^{-1}$);[1,2] rather, they offer inexpensive alternatives for specific applications. Thin films of organic materials can be easily prepared at low temperatures and also on large areas making their manufacturing less expensive than for inorganic semiconductors. In particular, they enable preparation on flexible substrates, which are relevant for up-to-date applications like flexible display backplanes or radio frequency identification tags. Moreover, OSCs are successfully applied in organic light-emitting diodes (OLEDs), photodiodes, photovoltaic cells and organic field effect transistors (OFETs).[3,4]

The chemical structure of organic molecules strongly affects their electronic, optical and structural properties. Therefore, they are typically classified according to their molecular structure: rod-like, plate-like and (nearly) spherical. In the framework of the present thesis the crystallization behaviour of promising organic small molecules of all three classes has been examined. The rod-like molecule *pentacene* ($C_{22}H_{14}$) belongs to the group of acenes and consists of five fused benzene rings in a row. It was amongst the first p-type semiconductors used in thin film OFETs; after many years of research charge carrier mobilities > 5.0 $cm^2V^{-1}s^{-1}$ with I_{on}/I_{off} ratios of 10^6 were reached.[4,5] Another class of rod-like molecules are oligothiophenes; a prominent molecule of this class is α-*sexithiophene* which consists of six thiophene units. In single-crystalline films mobilities up to 0.075 $cm^2V^{-1}s^{-1}$ were measured.[4,6] It has also evoked much research interest due to its large and highly polarized photoluminescence, just like the related rod-like molecule *para-hexaphenyl* (p-6P) studied in this work. Hence, both molecules are perfect candidates for optically active elements in organic light-emitting diodes. Two representative and highly related classes of plate-like molecules observed in this work are porphyrins and phthalocyanines.

For both classes mobilities of approximately 0.02 $cm^2V^{-1}s^{-1}$ were reported.[4,7] A great advantage of plate-like molecules is their tendency to crystallize in columnar stacks with a large π-π overlap. In addition, they show good thermal and chemical stability.

The nearly spherical fullerene molecule C_{60} is one of the rare n-type organic materials; mobilities up to 0.3 $cm^2V^{-1}s^{-1}$ were obtained in thin films.[8] Using fullerene C_{60} molecules as electron acceptors a remarkable increase in efficiency of organic photovoltaics was achieved.[9–11]

A number of comprehensive review articles has been written reflecting the research advances in this most actual segment of semiconducting devices, on which the following executive summary is based.[12–16] Since the present thesis is based on organic thin films used in organic field effect transistors and organic photovoltaics, the operating principles of these two devices are schematically explained in the following.

1.1 Organic Field Effect Transistors

In organic field effect transistors (OFETs) thin films of organic molecules are used as active layers. Figure 1.1 shows three different device configurations of thin-film transistors, where the configuration shown in Fig. 1.1 a is the most commonly used.[15] Here, the semiconducting organic thin film is deposited on a dielectric which isolates the underlying gate electrode. On top of the semiconducting layer source (S) and drain (D) gold contacts are applied. This configuration is referred to as *top-contact, bottom-gate*. Other configurations differ the positions of the S, D, G electrodes and are shown in Fig. 1.1 b (*bottom-contact, bottom-gate*) and Fig. 1.1 c (*bottom-contact, top-gate*). At zero voltage between the source and gate electrode there is no current flow; the device is switched off. Voltage applied to the gate electrode (V_{SG}) induces charge carriers at the semiconductor/dielectric interface (channel) and a S-D current is measured ('on' state). To activate a p-type (hole transport) semiconductor a negative gate voltage ($V_{SG} < 0$) has to be applied. For this purpose, the Fermi level of the source/drain electrode has to be close to the HOMO level of the semiconductor. This way the injected positive charges can easily overcome the energy barrier at the semiconductor/electrode interface, due to the D-S voltage ($V_{DS} < 0$). Analogously, to activate an n-type (electron transport) semiconductor a positive gate voltage ($V_{SG} > 0$) has to be applied which induces electrons to the channel. If the Fermi level of the electrodes is close to the LUMO level of the organic semiconductor, electrons can be extracted by applying the drain voltage ($V_{DS} > 0$). Ambipolar organic semiconductors can be operated by applying both polarities of voltage.

1.2 Organic Photovoltaics

Solar cells are electronic devices based on the inner photoelectric effect and convert electromagnetic radiation in the IR-VIS-UV range into electrical po-

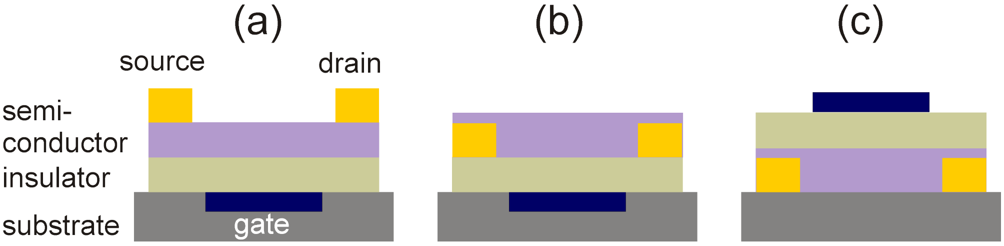

Figure 1.1: *Three different thin-film transistor structures: a) top-contact, bottom-gate b) bottom-contact, bottom-gate c) bottom-contact, top-gate. Based on Ref. [15]*

.

tential energy. The first generation of commercially realized solar cells is based on a single p-n junction of crystalline silicon. As manufacturing costs for silicon wafers are rather high there is need for less expensive, alternative active materials. Second generation devices use thin films of inorganic semiconductor materials, like amorphous silicon, semiconductors belonging to the II-VI group (CdS, CdTe) and chalcogenides $CuInSe_2$, $CuInGaSe_2$, which are suitable for large-area applications.
Organic-based devices are considered as the third-generation and comprise different classes of materials:[13] a) dye-sensitized solar cells, b) multijunction cells, c) hybrid approaches, combining inorganic semiconductors with organic materials and d) purely organic active layers.

In this work thin films of organic molecules which act as active materials for the group (d) of organic solar cells are investigated. Figure 1.2 shows a typical photovoltaic device based on the simplest purely organic architecture: a bilayer organic thin film. It consists of a transparent electrode (e.g. indium-tin oxid, ITO), a thin film of donor molecules, a thin film of acceptor molecules and a second electrode (e.g. Ag). Electron donor molecules (D) have a high-lying HOMO (highest occupied molecular orbital) and the acceptor molecules (A) a low-lying LUMO (lowest unoccupied molecular orbital) level. Here, a Zinc Phthalocyanine (ZnPc) molecule as donor material and Buckminsterfullerene (C_{60}) as electron acceptor are depicted. Exactly such structures will be discussed in Chapter 8 of the present theses.

The interface between the two layers is called the D/A heterojunction, and is crucial for the charge separation in organic solar cells. When the device is illuminated by light, following processes occur (see Fig. 1.2):

1. An incident photon excites an electron from the HOMO to the LUMO level. The electron in the LUMO and the hole in the HOMO level are electrostatically bound and form a quasi-particle called exciton. Contrary, to the situation in crystalline silicon, here, the thermal energy is not high enough to dissociate the exciton.

2. The internal field which is build in the vicinity of the donor/acceptor interface is large enough to dissociate the exciton. Only, if the exciton

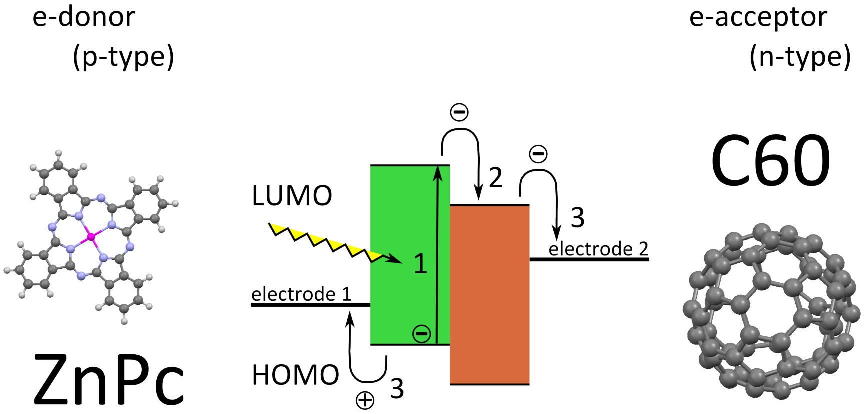

Figure 1.2: *Energy diagram of a donor-acceptor heterojunction. On the left (right) side representative organic molecules used as electron donor (acceptor) are depicted: Zinc Phthalocyanine (ZnPc) and Buckminsterfullerene* (C_{60})*.*

reaches the interface, the charges can be separated: the electron "drops" into the LUMO of the acceptor material while the hole remains in the donor material.

3. Given a high charge carrier mobility of the p-type and n-type layer, the separated charges can reach the electrodes and build-up a potential difference.

1.3 Importance of the structure

In general, the critical quantity for the performance of organic (opto)electronic devices is the charge carrier mobility of the used materials. The dependence of the charge carrier mobility on the diffusion coefficient D is described by the Einstein-Smoluchowski equation:

$$\mu = \frac{eD}{k_B T}. \tag{1.1}$$

Alternatively, the mobility μ is described by the ratio between the velocity of the charges v and an applied external field F, which induces a drift of the charge carriers:

$$\mu = \frac{v}{F}. \tag{1.2}$$

In this definition the unity of the charge carrier mobility μ is $\mathrm{cm^2V^{-1}s^{-1}}$ corresponding to velocity over electric field.[14] High mobility is ensured when charge carriers are able to move freely from molecule to molecule, without being trapped. The frequency of such events crucially depends on the quality of the thin films, i.e., the order and the specific packing of the molecules. This is lucidly exemplified by the fact that the mobility varies tremendously between disordered amorphous films (10^{-6} to 10^{-3} $\mathrm{cm^2V^{-1}s^{-1}}$) and highly crystalline films ($\geq 0.1\mathrm{cm}^2\mathrm{V}^{-1}\mathrm{s}^{-1}$).[13,14]

In an organic molecular system the electrons are highly delocalized along the backbones of single molecules, but between adjacent molecules charge transport relies on overlapping π-orbitals. Hence, structural order has a tremendous effect on the efficiency of the charge transport. The direction of π-stacking is perpendicular to the long molecular axes (LMA) in the case of rod-like molecules[14] and for plate-like molecules the direction of maximum orbital overlap is perpendicular to the macrocycle plane. Consequently, the electronic properties of such layers are highly anisotropic and - in addition to the need of growing highly crystalline thin films - it is absolutely crucial to control the particular orientation of the molecules with respect to the substrate surface. In the case of applications in OFETS, the π-stacking of the molecules has to be oriented perpendicular to the dielectric surface to provide sufficient current in the conducting channel. For applications in opto-electronics the π-stacking parallel to the contact is the most advantageous.[17]

The approach of epitaxial growth suits well to induce and control the order of organic molecules in thin films. With this method, organic molecules are thermally deposited on highly anisotropic surfaces which act as templates for the growth of organic crystallites.

Chapter 5 focuses on the crystallization behaviour of platelike molecules tetraphenyl-porphyrins and discusses the selectivity of the substrate surfaces on the formed polymorphic phase. As crystalline substrate surfaces KCl(100) and Cu(110)-(2×1)O were used.

In Chapter 6 thin films of rod-like molecule pentacene deposited on Cu(110) surfaces are investigated. In particular, the role of the very first layers on the alignment and the crystal structure of the molecules in the multilayer is elucidated.

Different to Chapters 6 & 5, which discuss the capability of inorganic single crystalline substrate surfaces as templates for the growth of organic molecules, Chapter 7 studies organic/organic heteroepitaxy of the rod-like molecules α-sexithiophene (α-6T) and para-hexaphenyl (p-6P): a highly oriented p-6P layer (obtained by epitaxial growth on the inorganic single crystal mica(001)) acts as alignment layer for α-6T molecules.

The last investigated systems is an all-organic system (see Chapter 8). Oriented layers of the polymer polycarbonate are used as substrate surfaces for the deposition of the plate-like molecules Zinc Phthalocyanine (ZnPc). The oriented ZnPc thin films themselves act as alignment layers for the subsequent deposition of buckminsterfullerene molecules C_{60}.

Chapter 2

Organic molecular crystals

2.1 Basics of crystallography

The aim of this section is to give a short overview of concepts and nomenclature used for the description of crystalline matter. For further reading, the interested reader is referred to the relevant literature on this topic [18–20].

Crystals are solid state materials, whose constituents show long range order with periodicity in three dimensions. The arrangement of its packing units can be described by a three dimensional unit cell, which is a parallelepiped spanned by three vectors ($\boldsymbol{a}$, $\boldsymbol{b}$, $\boldsymbol{c}$: unit cell vectors). Usually, a unit cell with the smallest possible volume is chosen. A macroscopic crystal is then described by an infinite repetition of the unit cell in three dimensions. Lattice vectors $\boldsymbol{R}$ describe a translational operation in the direction of unit cell vectors:

$$\boldsymbol{R} = n_1\boldsymbol{a} + n_2\boldsymbol{b} + n_3\boldsymbol{c}, \tag{2.1}$$

where n_1, n_2, n_3 are integers; relation 2.1 defines a crystal lattice.

The unit vectors are usually given by their magnitudes (a, b, c: lattice constants) and the three angles (α, β, γ) they are enclosing. Depending on this parameters, all crystals can be classified into seven crystal systems. By additionally taking possible lattice centrings into account (simple, base-centered, body-centered, face-centered) 14 different so-called *Bravais lattices* are distinguished. The periodically arranged material units can be composed of one or more atoms and as well of molecules. Formally, the Bravais lattices describe a three dimensional arrangement of lattice points (see Eq. 2.1), and it is thus necessary to assign lattice points to these units. The stacking unit assigned to a lattice point is called the *basis*. We can therefore write: *Crystal structure* = *Bravais lattice* + *basis*.[21,22]

Besides the inherent translational symmetry, there are groups of *symmetry operations* which leave the system invariant. These symmetry operations are inversions, rotations, reflections and their combination. Rotoinversions are obtained by a combination of the inversion operator with rotation operators; a special case of rotoinversion is the mirror reflection operator.[20,21,23] The assembly of symmetry operators which leaves at least one point fixed is called a

Table 2.1: *The 32 crystallographic point groups*

lattice systems	international tables	Schoenflies
triclinic	1	C_1
	$\bar{1}$	C_i
monoclinic	2	C_2
	m	C_s
	$2/m$	C_{2h}
orthorhombic	222	D_2
	$mm2$	C_{2v}
	$2/m\ 2/m\ 2/m$	D_{2h}
tetragonal	4	C_4
	$\bar{4}$	S_4
	$4/m$	C_{4h}
	$4mm$	C_{4v}
	422	D_4
	$\bar{4}2m$ or $\bar{4}m2$	D_{2d}
	$4/m\ 2/m\ 2/m$	D_{4h}
trigonal	3	C_3
	$\bar{3}$	C_{3i}
	32 or 321 or 312	D_3
	$3m$ or $3m1$ or $31m$	C_{3v}
	$\bar{3}\ 2/m$ or $\bar{3}\ 2/m\ 1$ or $\bar{3}\ 1\ 2/m$	D_{3d}
hexagonal	6	C_6
	$\bar{6}$	C_{3h}
	$6/m$	C_{6h}
	622	D_6
	$6mm$	C_{6v}
	$\bar{6}m2$ or $\bar{6}2m$	D_{3h}
	$6/m\ 2/m\ 2/m$	D_{6h}
cubic	23	T
	$2/m\ \bar{3}$	T_h
	432 or 312	O
	$\bar{4}3m$	T_d
	$4/m\ \bar{3}\ 2/m$	O_h

point group. Crystal symmetries can be classified into *32 point groups*, which are listed in Table 2.1.

In *International Tables for Crystallography*[18] so-called *Hermann-Mauguin* symbols are used to denote the point groups (central column of the table 2.1). They are to be read as follows:

- $\bar{1}$: inversion
- n: rotation about an n-fold axis (n … 1,2,3,4 and 6; $\frac{2\pi}{n}$)
- $\overline{n}$: rotoinversion (rotation about an n-fold axis followed by inversion)
- m: reflection through a plane of symmetry (mirror plane)
- $\frac{n}{m}$: rotation about an n-fold axis and a mirror plane perpendicular to it

- nm: rotation about an n-fold axis and a mirror plane parallel to it

In Table 2.1 the short notation is used, where axes without symmetry properties are omitted. For the monoclinic system, for instance, only [010] is an axis of symmetry and $1\frac{2}{m}1$ is abbreviated as $\frac{2}{m}$. One must pay attention that different lattice systems exhibit different high-symmetry directions, which are, for example, listed in *International Tables of Crystallography.* The rightmost column of Table 2.1 lists the so-called *Schoenflies* symbols; they are preferentially used in molecular spectroscopy.

When so-called *improper symmetry operations* (glide planes and screw axes) are taken into account as well, *230 space groups* result. Space groups and point groups are related, and this is reflected by the respective notations. The *Herman-Mauguin* notation for space groups consists of four parts. The first part is a capital letter denoting the type of the lattice centring (P (primitive); I (body-centered); F (all-face centered); A, B, C (one-face centered; (b,c), (c,a), (a,b)); R (hexagonal cell, rhombohedrally centered)). The other 3 parts describe the most prominent symmetry operations along the 3 high-symmetry directions of the crystal lattice. In addition to the symmetry operations already used for the description of the point groups, *screw axes* are denoted by a subscript n (rotation by $\frac{2\pi}{n}$ followed by a translation along the given axis) and a *glide plane* is denoted by a, b, or c depending on the glide axis. In the Schoenflies notation, space groups are distinguished by a superscript applied to the point group symbol. As an example, space groups belonging to the C_s point group are denoted as following: C_s^1, C_s^2, C_s^3, C_s^4.

2.2 Peculiarities of molecular crystals

Having discussed the basics about crystal symmetries and their notations, it is important to emphasize that the maximum number of symmetry operations of a space group is given by the respective lattice. In general, the symmetry of the crystal structure will be reduced when additionally the basis is taken into account[21,22] and in case of molecular crystals the basis is rather complex.

Brock et al. (1994)[24] stress that the main difference in the packing behaviour of inorganic and organic materials is due to the shapes of their packing units. Their analysis of the Cambridge Structural Database (CSD) entries has revealed that 38% of the 31770 organic structures crystallize in the $P2_1/c$ space group and 20% are classified into the $P\bar{1}$ space group. Contrary, in inorganic materials there is no single specific space group, which makes up more than 8%. When the distribution according to the lattice systems is considered, about 55% of organic structures account to the monoclinic system; in total, 75% belong either to the monoclinic or the triclinic system.

Kitajgorodskij[25,26] has made essential contributions to describing the intermolecular forces which govern the packing behaviour in organic crystals. He has reduced the interaction between two molecules to a sum of atom-atom interactions, which are pairwise additive. The potential between two atoms (1,2) is described by the following equation:[25,27]

$$V_{12} = \frac{A_{12}}{r^{12}} - \frac{C_{12}}{r^6} + \frac{q_1 q_2}{r} \tag{2.2}$$

The first two terms represent the *Lennard-Jones potential*; in the first term the exchange repulsion between overlapping electron clouds is taken into account, while the second one is the attractive van der Waals potential between fluctuating dipole moments which also exists between nonpolar atoms. The last term in Eq. 2.2 takes into account Coulomb interactions between partial charges of the two atoms. When summed over all atoms in the two molecules, last term gives their dipol-dipol interaction. The lattice energy is obtained when Eq. 2.2 is summed over all atoms in all molecules constituting the crystal:

$$E = \frac{1}{2} \sum_i \sum_j \frac{A_{ij}}{r_{ij}^{12}} - \frac{C_{ij}}{r_{ij}^6} + \frac{q_i q_j}{r_{ij}}, \tag{2.3}$$

where i sums over all atoms of the i-molecule and j sums over atoms in other molecules.

An energetically stable crystal structure is given by a minimum of the free energy ($F = E - TS$); however, it was shown that the entropy term (TS) can be neglected and the lattice energy can be approximated by:[27]

$$\frac{\partial E}{\partial a_i} = 0 \quad i = 1, \ldots, n. \tag{2.4}$$

Here, a_i denote all degrees of freedom in a crystal lattice, i.e., lattice constants and the position of the molecules in the crystal lattice.

The larger the van der Waals interaction between molecules (cf. Eq. 2.3), the lower the lattice energy; close-packing of the molecules thus leads to an energy minimum (of course, for distances < r* (potential minimum), the repulsion potential predominates). For organic molecules, the lattice energy E exhibits many quasi-equal local minima giving rise to the phenomenon of polymorphism, discussed in the next Section 2.3.

The endeavour of organic molecules to maximize van der Waals interactions, in combination with their anisotropic shape leads to the specific space groups being favoured (as discussed before). Moreover, two specific motifs can be identified which are predominantly present in their crystal packing: glide favoured or stack favoured (see Fig. 2.1).[28] The glide favoured motif is the so-called *herringbone packing* (Fig. 2.1 a). Here, the C$\cdots$C intermolecular interactions between closest non-parallel neighbours are dominant. A related structure is the sandwich herringbone structure where pairs of molecules arrange in a herringbone motif. In *stacked packing*, the C$\cdots$C interactions between neighbouring parallel molecules are dominant (Fig. 2.1 b). Within the stacked structures one can further distinguish between two classes, depending on whether C$\cdots$H interactions additionally contribute significantly to the lattice energy (γ-type) or not

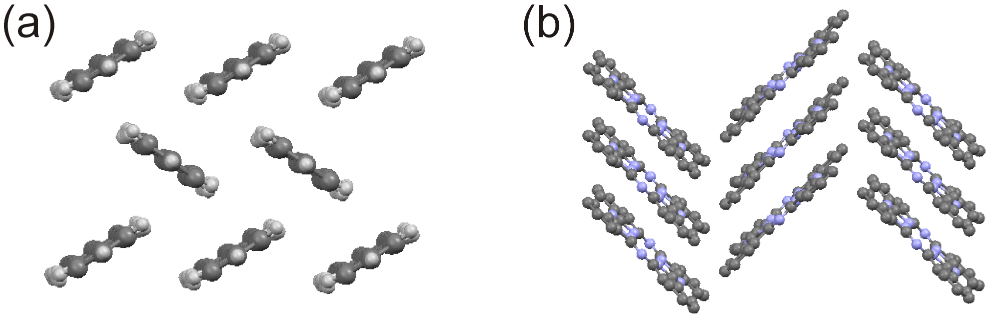

Figure 2.1: *Preferred packing motifs of organic small molecules: a) herringbone arrangement and b) stacked packing.*

(β-type). As a rule of thumb, one observes that many rod-like molecules pack in a herringbone arrangement while for plate-like molecules the stacked motif is energetically more favourable.

The weakness of intermolecular interactions in molecular crystals is evidenced by their physical properties as well. Their sublimation and melting temperatures are low as well as their mechanical strength. Another consequence of the weak bonding is that the electronic bands are narrow, which is highly attractive for optical applications like light emitting diodes.

2.3 Polymorphism

Polymorphism is the property of a material to adopt different packings in the solid state and thus exhibit different crystal structures. In other words, two structures are polymorphic when their arrangement in the solid state differs although their composition is the same in a melt. The consequence of different arrangements in the solid state are different physical and chemical properties of the compound, like its solubility, density, (photo)chemical reactivity or electrical and optical properties etc. Further properties which may differ between different polymorphs are listed in Tab. 2.2 (according to Braga et al. (2009)[29]). The surely most prominent example of a compound which adopts different polymorphic phases is carbon: depending on the circumstances it can crystallize in a hcp structure yielding the brittle, black graphite or in a fcc structure of diamond.[30] Nowadays, the most efforts in revealing the phenomenon of polymorphism are made by the pharmaceutical industry as the effectiveness of drugs crucially depends on their polymorphic phase.[29,31–34]

Organic molecules are in particular prone to polymorphism. Due to their weak and non-directional van der Waals intermolecular interactions different packings can reveal quasi-equal lattice energies (cf. previous Chapter).[35] Different trade-offs between close packing, π-π-stacking and hydrogen bonding give rise to various polymorphic phases.[33]

An instructive way of describing polymorphic phases are phase diagrams. In a free energy vs. temperature phase-diagram the stable phase has the lowest free-energy F (p, V beeing fixed); phases having a higher free energy are called metastable. In an F-T phase-diagram the point of intersection between two phases defines the transition temperature, given that it is lower than the respective melting temperatures.

Starting with the inequality:

$$F_I < F_{II}, \tag{2.5}$$

where F_I is the free energy of the stable and F_{II} of the metastable phase, a very important inequality can be derived:

$$C_I < C_{II}, \tag{2.6}$$

where C is the molar concentration of the respective polymorph in solution.[31] This means that the most stable polymorph has the lowest solubility in a solvent. Unfortunately, many organic small molecules used in this work are not soluble and a distinction between metastable and stable phases is not easily performed. Therefore, systematic investigations of structural properties upon changing the growth parameters (like temperature or growth rate) are crucial for determining the properties of different phases and their transition temperatures.

According to the phenomenological *Ostwald rule of stages* which was formulated already in 1897, the initially formed phase is usually not the thermodynamically most favourable one, but the one with the fastest crystallization rate.[36] Thus, the stable phase is often denoted as “thermodynamic” or “equilibrium” phase, whereas “kinetic” or “non-equilibrium” phase are terms used for metastable phases. However, due to a high activation energy in most cases there is no spontaneous phase transition from a metastable to a stable phase - it only occurs when energy is externally supplied.[32]

Especially in thin films, where molecules crystallize from the vapour phase onto substrates, there are many parameters which can hamper the crystallization in the equilibrium phase. Haleblian et al. (1969)[30] showed that in particular the temperatures involved during the crystal growth are crucial. Usually, the powder of organic molecules is sublimated at a much higher temperature than

Table 2.2: *An overview of properties which may differ between polymorphic phases (according to Ref. [29]).*

physical properties	**chemical properties**	**mechanical properties**	**surface properties**
density	reactivity	hardness	surface free energy
refraction	solubility	compression	surface area
conductivity	hygroscopicity	thermal stability	crystal habit
melting points	vapour pressure	thermal expansion	particle size distribution

the substrate surface temperature it is condensed on. The higher the difference between the sublimation temperature and the substrate temperature, the higher the probability for the adoption of a metastable phase. Further, for the hetero-nucleation on a substrate the involved surface energies as well as their interface energy come into play. In this thesis, it is shown that also the substrate surface (see Chapter 5) and alternatively the first monolayer (see Chapter 6) is able to induce a growth of a specific polymorphic phase. In addition, investigations on crystal structures of thin films have enriched polymorphism of organic molecules by an additional phenomenon: the so-called *surface induced phases*, which exclusively occur in thin films.

Most of the organic molecules investigated in this thesis are in the focus of research for many years and as an often cited quotation by McCrone (1963) says "*Virtually all compounds are polymorphic and the number of polymorphs of a material depends on the amount of time and money spent in research on that compound.*". In the following chapter the diversity of reported polymorphic phases for the respective molecules are listed and discussed.

2.4 Polymorphism of molecules under study

The comparison of crystallization behaviour of different organic molecules used in this work reveals that the shape of the molecule influences the symmetry of its crystal structure. The highly anisotropic rod-like molecule pentacene (5A) exclusively crystallizes in triclinic crystal structures, exhibiting the herringbone packing. Nevertheless, many different polymorphic were observed (with admittedly rather subtle differences). Rod-like molecules para-hexaphenyl (p-6P) and α-sexithiophene (α-6T) pack in a herringbone arrangement as well, but only occur in monoclinic structures. Contrary, the more symmetric plate-like molecule tetraphenyl-porphyrine adopts a huge variety of different crystal structures - ranging from triclinic to tetragonal phases. Phthalocyanines are also highly prone to polymorphism; however, contrary to the eclectic phases of porphyrins, here most structures are monoclinic. The nearly spherical molecule C_{60} - as expected - preferentially adopts close-packed hcp or fcc structures.

2.4.1 Pentacene

Pentacene (5A, $C_{22}H_{14}$) is one of the most investigated rod-like molecules and is composed of five benzene rings. An overview of the most important polymorphs found for pentacene is given in Table 2.3. All listed structures are triclinic herringbone arrangements with rather similar lattice constants. For the unambiguous distinction between these phases, the interplanar spacing along the c*-axis (d_{001}) is often used (see Fig. 2.2). Structures found in single crystals exhibit either a d_{001} of ~1.45 nm (Campbell-phase,[37,40] Fig. 2.2 b) or ~1.41 nm (Holmes-phase,[38–40,44] Fig. 2.2 a). More recently, a polymorphic phase exclusively occurring in thermally evaporated thin films has been observed. In this so-called thin-film (TF) phase the d_{001} spacing is significantly larger having a value of ~1.54 nm (see Fig. 2.2 c).[41–43] This large interlayer spacing is

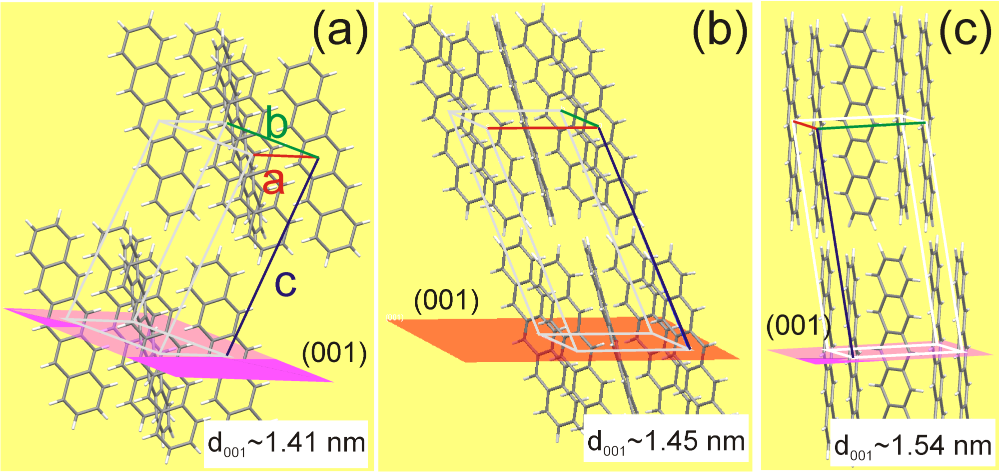

Figure 2.2: *Different polymorphic phases of the pentacene molecule. a) Holmes-phase and b) Campbell-phase are single crystalline phases. c) Thin film-phase occurs exclusively in thin films.*

reflective of a nearly parallel alignment of the long molecular axis (LMA) along the c*-direction. Pentacene thin films aligning with the (001) lattice plane of this specific phase parallel to a substrate surface are highly advantageous for applications in OFETs. They yield molecules oriented with their LMAs perpendicular to the substrate surface and provide an efficient charge carrier transport parallel to the substrate surface.

Calculations based on (quasi) Monte-Carlo simulations show that the single crystal phases (i.e. d_{001} ~1.41 nm or ~1.45 nm) correspond to the equilibrium structures with the lowest energy minima.[45] Therefore, the thin film structure is often considered as a metastable phase which is only favoured in kinetically trapped systems.[40] It is suggested to occur when the molecules do not have enough energy or time to reach the lowest energy minimum, e.g. at low substrate temperatures and high depositions rates. Another phenomenologically found requirement for a occurrence of the thin-film phase is a small thickness of the film (< 50 nm). This is in line with the properties of a metastable phase, as it is known that large crystallites of a metastable phase are less stable than small crystallites.[46] Temperature-dependent in-situ XRD experiments support the assumption that the thin film phase is a metastable one. Moser et al.[47] have shown that pentacene films which have crystallized in the thin film phase undergo a phase transition to a single crystal phase when annealed to a substrate temperature of 480 K.

Results obtained for epitaxially grown pentacene molecules on Cu(110)-(2×1)O surfaces (see Chapter 6) show that the growth parameters mentioned above do not offer a complete explanation.[48] There it is shown that both polymorphic phases (single crystal and thin film) can be obtained for thin films prepared on the same substrate surface, at the same substrate temperature, same deposition rate and the same thickness of the films. There it is also sug-

Table 2.3: *Unit cell parameters of different polymorphic phases observed for pentacene molecules. Phases are named after the corresponding author and the temperature at which the phase was observed (where the information was available). RT stands for room temperature, TF for thin film phase.*

polymorphic phase	a(Å)	b(Å)	c(Å)	α(deg)	β(deg)	γ(deg)	ref. no
Campbell	7.90	6.06	16.01	101.90	112.60	85.80	[37]
Holmes	6.275	7.714	14.442	76.75	88.01	84.52	[38]
Mattheus RT	6.266	7.775	14.530	76.475	87.682	84.684	[39]
Mattheus 90K	6.239	7.636	14.330	76.978	88.136	84.415	[39]
Siegrist 120K	6.292	7.690	14.410	76.66	88.16	84.36	[40]
Siegrist RT	6.287	7.806	14.5799	76.46	87.63	84.36	[40]
Siegrist 414K	6.275	7.888	14.709	76.01	87.23	84.996	[40]
Siegrist 478K	6.119	8.058	15.097	80.88	76.68	85.89	[40]
Schiefer TF	5.958	7.596	15.6096	81.25	86.56	89.8	[41]
Yoshida TF	5.93	7.56	15.65	98.6	93.3	89.8	[42]
Nabok TF	5.92	7.54	15.653	81.5	87.2	89.9	[43]

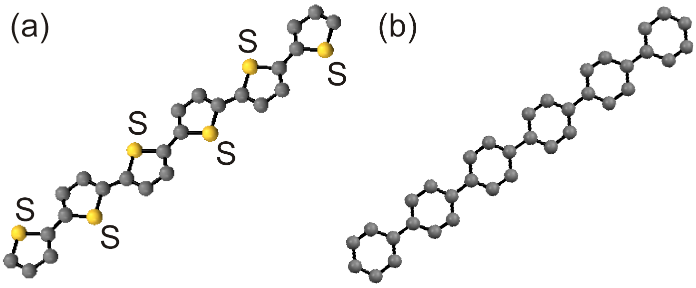

Figure 2.3: *Molecular structure of the small molecules a) α-sexithiophene and b) para-hexaphenyl*

gested, that the formation of the thin film phase is a consequence of a system being kinetically trapped . We show that the reason for kinetical "trapping" can also be an unfavourable geometry of the first monolayer, which significantly hampers the diffusion of the molecules and prevents a stable phase to be formed.

2.4.2 α-Sexithiophene and para-Hexaphenyl

Another important rodlike small molecule is α-sexithiophene (α-6T; $C_{24}H_{14}S_6$) which consists of six thiophene units (see Fig. 2.3 a). Different polymorphic phases of α-sexithiophene are reported, all of which are herringbone- packed monoclinic structures. The polymorphs are preferentially distinguished by the (200) interlayer spacing (d_{200}). Servet et al. (1994)[49] reported on various polymorphic phases formed in vacuum-evaporated films, which are denoted as α-, β-, γ- and δ-phase. The α-phase is formed by low deposition rate and is considered to be the stable phase, exhibiting d_{200}= 23.7 Å. Contrary, the β-phase is formed for fast deposition rates and is therefore considered as the metastable (kinetically favoured) phase. The corresponding interplanar spacing is d_{200}= 24.4 Å. At high temperature phases γ (d_{200}= 22.42 Å) and δ (d_{200}= 36.3 Å) are formed. Note that none of these phases is listed in the Cambridge Structural Database (CSD). The only full structural solutions contained in CSD are the so-called high-temperature[50] (HT; d_{001}= 20.48 Å) and the low temperature[51] phase (LT; d_{200}= 22.352 Å - similar to the γ-polymorph). The corresponding lattice constants are listed in Table 7.1. In thin films on various substrates exclusively the LT phase is observed.

Similarly, there is a predominant phase in thin films of para-hexaphenyl (p-6P). This so-called Baker phase is a monoclinic structure often observed in single crystals, with the typical herringbone-arrangement.[52] Like for α-6T, a high temperature phase was observed as well.[53] The lattice parameters for both phases are listed in Table 2.4.

Table 2.4: *Unit cell parameters of different polymorphic phases observed for α-sexithiophene (6T) and para-hexaphenyl (6P) molecules. High temperature phases are denoted by HT and low temperature by LT.*

polymorphic phase	a(Å)	b(Å)	c(Å)	α(deg)	β(deg)	γ(deg)	ref. no
6T - LT	44.708	7.851	6.029	90	90.76	90	[51]
6T - HT	9.140	5.684	20.672	90	97.78	90	[50]
6P - Baker	8.091	5.568	26.24	90	98.17	90	[52]
6P - HT	7.98	5.54	27.64	90	99.8	90	[53]

2.4.3 Tetraphenyl-porphyrins

The platelike tetraphenyl-porphyrin (H_2TPP) molecules comprise two electronically decoupled parts: a highly-conjugated macrocycle of 4 pyrrol rings and 4 phenyl side groups (see Fig. 2.4). Porphyrin molecules are known to be easily deformable. Depending on their actual surrounding or the specific crystal structure they form, phenyl rings adopt different angles in respect to the macrocycle. The macrocycle is not rigid as well and can deviate from its planar conformation. This gives rise to the phenomenon of conformational polymorphism: because in different crystal structures the packing forces imposed on molecules are different, the molecular conformation adopted in different crystal structures varies.

The center of the macrocycle comprises 4 nitrogen atoms, two of them being bound to hydrogen atoms. These two hydrogen atoms are easily substituted by a metal atom. Due to the huge versatility of the (metallo-)porphyrins many different system were investigated, and many different crystal structures were found. In the course of this investigations another phenomenon is often observed: isomorphism, denoting the fact that chemically different compounds crystallize in the same or a very similar structure.

In Chapter 5 will discuss the structural properties of H_2TPP and PtTPP

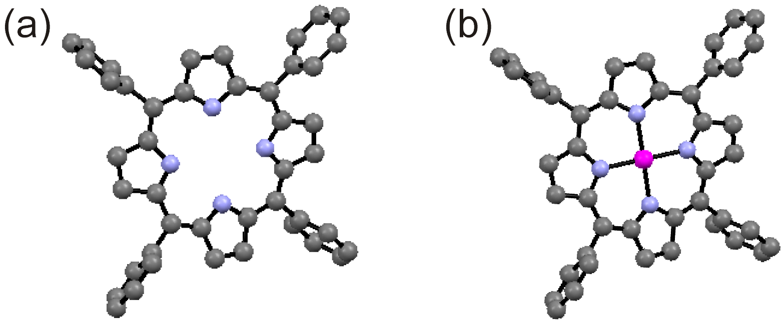

Figure 2.4: *Molecular structure of the a) Tetraphenyl-porphyrin (H_2TPP) molecule and b)Platinum Tetraphenyl-porphyrin PtTPP.*

thin films deposited on KCl(100)- and Cu(2x1)O-surfaces. The polymorphic phases for these two compounds are summerized in Table 2.5. Additionally, a CuTPP crystal structure is listed as well, which is isomorphous with the one we have observed for PtTTP molecules deposited on KCl(100) substrate (cf. Chapter 5)

Table 2.5: *Unit cell parameters of different polymorphic phases observed for (metallo-)tetraphenyl-porphyrine molecules.*

polymorphic phase	a(Å)	b(Å)	c(Å)	α(deg)	β(deg)	γ(deg)	ref. no
H_2TPP	6.44	10.42	12.41	96.06	99.14	101.12	[54]
H_2TPP	12.0	19.0	14.7	90	90	90	[55]
H_2TPP	15.125	15.125	13.94	90	90	90	[56]
PtTPP	15.073	15.073	13.988	90	90	90	[57]
CuTPP	13.375	13.375	9.735	90	90	90	[58]

2.4.4 Phthalocyanines

Phthalocyanine molecules are structurally very similar to porphyrins; they also consist of four connected pyrrol rings which form a large macrocycle. As in the case of porphyrins, for the metal-free phthalocyanines (H_2Pc) two out of four nitrogen atoms are bound to hydrogens (Fig. 2.5 a), and substituting them by a metal atom, leads to a huge variety of metallo-phthalocyanines (PcM): more than 70 different PcMs have been reported up to now.[59]

Consistent with McCrone's statement (s. page 15), many different polymorphic phases have been found. They are preferentially denoted by lower-case Greek letters and so far α-, β-, γ-, δ-, ϵ-, π-, τ- and χ- polymorphs have been reported (Hoshino et al.(2003)[62] and references therein). Some of these structures are listed in Table 2.6.[60–67] The mostly observed phases are the α- and β-polymorphs. The main difference between these two structures is the tilting of the molecules in respect to each other. This difference is best reflected in the

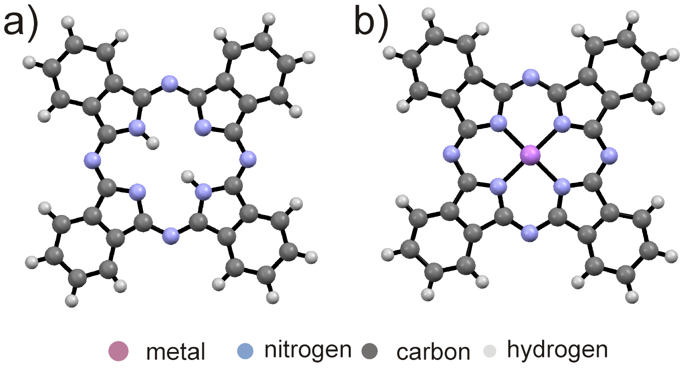

Figure 2.5: *a) Molecular structure of a metal-free phthalocyanine (*H_2Pc*) b)Molecular structure of a metalo-phthalocyanine PcM.*

Table 2.6: *Unit cell parameters of different polymorphic phases observed for phthalocyanine molecules.*

polymorphic phase	a(Å)	b(Å)	c(Å)	α(deg)	β(deg)	γ(deg)	ref. no
α_I-H_2Pc, $\alpha(\times)$	26.124	3.801	23.889	90	94.18	90	[60]
α_I-PtPc, $\alpha(\times)$	26.29	3.818	23.92	90	94.6	90	[61]
α_{II}-CuPc, $\alpha(+)$	12.886	3.769	12.061	96.22	90.62	90.32	[62]
α_{II}-ZnPc, $\alpha(+)$	12.3	3.8	12.8	90	90	96	[63]
β-H_2Pc, $\beta(\times)$	19.85	4.72	14.80	90	122.25	90	[64]
β-CuPc, $\beta(\times)$	19.407	4.790	14.628	90	120.93	90	[65]
β-ZnPc, $\beta(\times)$	19.274	4.854	14.553	90	120.48	90	[66]
γ-PtPc, , $\alpha(+)$	25.780	3.969	23.16	90	94.6	90	[61]
χ-H_2Pc, $\beta(+)$	14.796	4.733	17.357	90	104.32	90	[67]

length of the b-axis which is characteristic for the specific polymorphic phase: 3.8 Å for the α-phase and 4.8 Å for the β-phase. Here, the b-axis corresponds to the shortest crystal axis and gives the stacking direction of the Pc molecules. Most commonly, this parameter is used for discrimination between different polymorphic phases, but it does not suffice.

Hoshino et al (2003)[62] have suggested an alternative denotation, arguing that structures exhibiting similar lattice constants (similar b-axis) can in fact reveal a significantly different molecular stacking. Therefore, they distinguish the structures by the molecular offset directions between two molecules in a stack: the difference between α_I and α_{II} (which is in fact identical to γ) are 45°. These two configurations are then denoted by $\alpha(\times)$ and $\alpha(+)$, where the symbols × and + correspond to the relative stacking direction in molecular columns. The same differences are found in β-phases, which are correspondingly denoted by $\beta(\times)$ and $\beta(+)$. This nomenclature has the advantage of revealing the similarities and differences between different structures and is therefore included in Table 2.6.

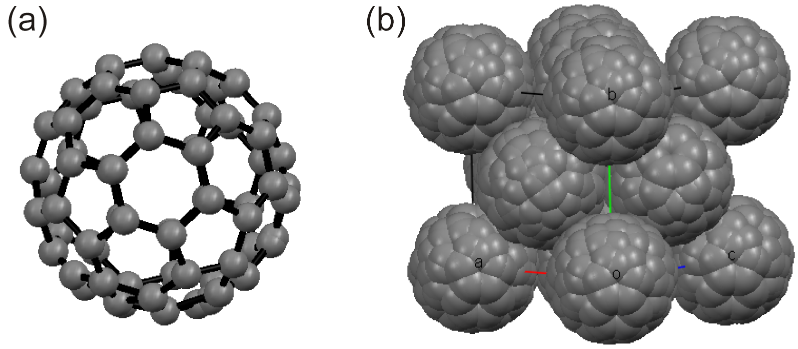

Figure 2.6: *Molecular structure of the a) Buckminsterfullerene (C_{60}) molecule and b) its packing in a fcc structure.*

2.4.5 Fullerene C_{60}

Although C_{60} fullerenes (because of their soccer-ball-shape they are also called buckyballs) are highly isotropic molecules of a nearly spherical shape they can adopt different crystallographic phases. Contrary, to the anisotropic organic molecules discussed before, symmetric C_{60} molecules crystallize mainly in face-centred cubic (fcc) or hexagonal close-packing (hcp) structures. Basically, three different lattices were found so far (s. Table 2.7). Krätschmer et al. (1990) reported on a "somewhat disordered" hexagonal close-packing.[68] The structure of C_{60} single crystals grown from a hexane solution was determined to be hexagonal but not close-packed.[69] The fcc phase observed by Bürgi et al. with a lattice constant $a = 14.061$ Å[70] was reported with slight variations also by many others.[71,72]

In deposited C_{60} thin films often a mixture of fcc and hcp crystallites occurs.[73,74] The hexagonal (close) packing is considered as a metastable phase, as it preferential occurs in thin films, powders and single crystals grown from solution, where high purity is not assured. Contrary, single crystals grown by sublimation of highly purified material mainly exhibit the fcc-phase.[75]

Table 2.7: *Unit cell parameters of different polymorphic phases observed for fullerene* C_{60} *molecules.*

polymorphic phase	a(Å)	b(Å)	c(Å)	α(deg)	β(deg)	γ(deg)	ref. no
Krätschmer, hcp	10.02	10.02	16.36	90	90	90	[68]
Hawkins	33.540	33.540	10.113	90	90	120	[69]
Bürgi, fcc	14.061	14.061	14.061	90	90	90	[70]

Chapter 3

Epitaxy

Epitaxy is a commonly used technique to grow inorganic thin films in registry with underlying crystalline substrates. The idea of epitaxy is to transfer the order of a crystalline substrate surface onto the deposited material. The deposited atoms endeavour to adopt an arrangement which coincides as well as possible with the order of the substrate. In terms of crystallography, a long-range order is described by crystallographic lattices (cf. 2.1); in case of surfaces two dimensional lattices are used. Using this nomenclature, epitaxial growth means that the surface lattice formed by the overlayer coincides with the lattice of the substrate surface. Epitaxial growth is successfully used for the growth of crystalline thin films of semiconductor materials like silicon-germanium or gallium arsenide. In such inorganic material, already a lattice-mismatch of 1 % yields unordered films.[76]

3.1 Epitaxy of organic molecules

Epitaxial growth of organic molecules differs from that of inorganic materials in many respects. This is due to the above discussed peculiarities of organic molecular crystals (cf. 2.2). The interaction between the molecules within the organic overlayer is governed by weak non-covalent forces; usually, the interactions between the overlayer and the substrate are of the same type. A consequence of weak interactions are shallow potential functions, which make different molecular arrangements equally favourable.[77] Aside from that, due to the high anisotropy of organic molecules, the formed crystal structures are low in symmetry and exhibit significantly larger lattice constants than their inorganic counterparts. These properties make it more difficult for organic molecules to adopt an arrangement in registry with the substrate surface lattice. Nevertheless, well-ordered, organic films can be grown by epitaxy. A broader theory than used in inorganic epitaxy is needed to account for types of arrangement specific to inorganic/organic epitaxy as discussed in the following.

3.1.1 Modes of epitaxy

The following classification of epitaxial modes of organic overlayers in respect to substrate lattices is based on a review of Hooks et al. (2001).[77] The epitaxial interface is fully determined by lattice parameters of the substrate surface (a_1, a_2, α), the lattice parameters of the overlayer (b_1, b_2, β) and the azimuthal angle (θ) between the lattice vectors $\boldsymbol{a}_1$ and $\boldsymbol{b}_1$. The epitaxial matrix $\mathbf{M}$ gives the transformation between the substrate and overlayer lattice vectors:

$$\begin{bmatrix} \boldsymbol{b_1} \\ \boldsymbol{b_2} \end{bmatrix} = [C] \begin{bmatrix} \boldsymbol{a_1} \\ \boldsymbol{a_2} \end{bmatrix} = \begin{bmatrix} p & q \\ r & s \end{bmatrix} \begin{bmatrix} \boldsymbol{a_1} \\ \boldsymbol{a_2} \end{bmatrix}. \tag{3.1}$$

The coefficients of the matrix $[C]$ are defined as follows:

$$p = \frac{b_1 sin(\alpha - \theta)}{a_1 sin(\alpha)}, \tag{3.2}$$

$$q = \frac{b_1 sin(\theta)}{a_2 sin(\alpha)}, \tag{3.3}$$

$$r = \frac{b_2 sin(\alpha - \theta - \beta)}{a_1 sin(\alpha)}, \tag{3.4}$$

$$s = \frac{b_2 sin(\theta + \beta)}{a_2 sin(\alpha)}. \tag{3.5}$$

Depending on the values of these coefficients, different epitaxial modes can be distinguished. They are listed below and sorted from the energetically most to the least favourable arrangement.

A) Commensurism (POP) In this case, the four matrix coefficients p, q, r, s are all integers. This mode is also denoted as *“point-on-point”* (POP) coincidence, as every lattice point of the overlayer matches a lattice point of the substrate surface unit cell. Because, the periodicity of a surface potential is predetermined by the periodicity of the surface, a commensurate interface is energetically the most favourable (only in this case the potentials of the substrate and the overlayer are phase coherent).

B) Coincidence I (POL) At least two matrix coefficients in the same column are integers. Illustratively, this means that every lattice point of the overlayer coincides with one primitive lattice direction of the substrate surface. Therefore, this epitaxial mode is also called *“point-on-line”* coincidence. Depending on the values of the non-integer coefficients, this mode is divided into two following classes.

Coincidence IA The remaining two coefficients in the epitaxial matrix are rational numbers. Hence, it is possible to construct a *supercell* (defined as a multiple of the initial unit cell) which then forms a commensurate structure with the underlying substrate.

Coincidence IB At least one of the two coefficients is an irrational number; therefore, no supercell can be constructed which is commensurate with the substrate.

C) Coincidence II Here, all coefficients are rational and no column contains only integers. Due to the rational coefficients a supercell can be constructed which is commensurate with the substrate surface. This epitaxial mode is also referred to as *"geometrical coincidence"*.

D) Incommensurism There is no column containing integers and at least one of the coefficients is an irrational number. This means, there is no coincidence between the overlayer and substrate.

The arrangement of molecules on a substrate surface (resulting in a specific epitaxial mode) can be described by energetic balancing. On the one hand, there is the interaction between the overlayer molecules, denoted as the intralayer energy $E_{\mathrm{mol-mol}}$. As described in Section 2.2, these are the non-covalent van der Waals interactions which determine the packing of the molecules in a crystal structure. On the other hand, the interaction between the overlayer molecules with the underlying substrate results in an interface energy $E_{\mathrm{mol-sub}}$. This interaction controls the alignment of the molecules on the substrate surface within the first few layers. From here on, a bulk structure with a preferential lattice plane oriented parallel to the substrate surface (contact plane) is formed.
For describing the various alignment scenarios it is useful to look at the curvature c of the corresponding potentials is considered:

$$\frac{dE^2}{dx^2} = c. \tag{3.6}$$

For strong molecule-substrate interactions the curvature of the $E_{\mathrm{mol-sub}}$ potential will be larger than that of $E_{\mathrm{mol-mol}}$: $c_{\mathrm{mol-mol}} < c_{\mathrm{mol-sub}}$. Given there is a possibility of adopting a *commensurate* structure with the substrate surface, this will lead to the most favourable arrangement.

Contrary, when $c_{\mathrm{mol-mol}} >> c_{\mathrm{mol-sub}}$, an *inherent* molecular arrangement will be formed, which generally corresponds to a low-energy lattice plane arrangement of the most likely crystal structure under given conditions. The $E_{\mathrm{mol-sub}}$ potential is too weak to induce an alignment of the molecules in registry with the substrate surface and therefore, here *incommensurate* structures are expected.

However, for cases where $c_{\mathrm{mol-mol}} > c_{\mathrm{mol-sub}}$ the *inherent* molecular arrangement can lead to a registry with the substrate surface as well. For the case where $c_{\mathrm{mol-mol}} \sim c_{\mathrm{mol-sub}}$ slight changes of the overlayer lattice constants to better fit are observed to the lattice of the substrate surface.

Organic/organic heteroepitaxy

In addition to the above discussed epitaxial modes, often well-ordered organic thin films are observed which cannot be classified using this scheme. Mannsfeld et al. (2005)[78] reported on a new type of epitaxy they have observed on organic/organic heterolayers (but which also occurs in inorganic/organic systems). This is the so-called *line-on-line (LOL)* coincidence which is characterized by an alignment of *non-primitive* lattice directions of overlayer and substrate surface parallel to each other. Although, there is no geometrical match between the respective surface lattices, such an alignment can correspond to a minimum of the interface energy between the overlayer and substrate.

Related to this "weakened" epitaxial relationship are observations that surface corrugations of the substrate induce preferential alignment of deposited molecules as well. Particularly, in the case of rod-like molecules preferentially the long molecular axis is oriented (nearly) parallel to the tranches caused by surface corrugation.[79,80]

3.2 Fabricating thin films

Organic conjugated molecules are characterized by low solubility, which is rationalized by strong π-π-interactions and their molecular rigidity.[4] However, they show a high thermal stability and therefore organic thin films are preferentially prepared from vapour phase. Solvent-free preparation from the gaseous phase ensures low impurity rate and thus yields well-ordered thin films. An additional advantage of evaporative deposition is the precise control of the film thickness. Two thermal evaporative techniques which have been used for the preparation of thin films within the scope of this thesis are described in the following.[81]

3.2.1 Physical vapour deposition

Organic molecules used in this work were purchased in powder form. Evaporation chambers operated under high vacuum (HV; $p < 10^{-6}$ mbar) as well as under ultra high vacuum (UHV; $p < 10^{-9}$ mbar) were used. The source material is filled into a crucible and evaporated by electrically resistive heating. The required source temperature for organic molecules lies usually between 200-300 °C. Due to the low pressure, particles propagate freely to the substrate where they finally condense. The substrate temperature can be adjusted as well, which usually is a parameter having a high impact on the crystallization behaviour of thin films. A quartz microbalance is placed next to the substrate at the same distance from the source crucible. It determines the deposition rate and thus the film thickness.[82]

3.2.2 Hot Wall Epitaxy

The main characteristic of the hot wall epitaxy (HWE) system shown in Figure 3.1 is a closed growth reactor. The growth reactor is a cylindrical quartz tube placed between three resistance ovens and the whole system is kept in high

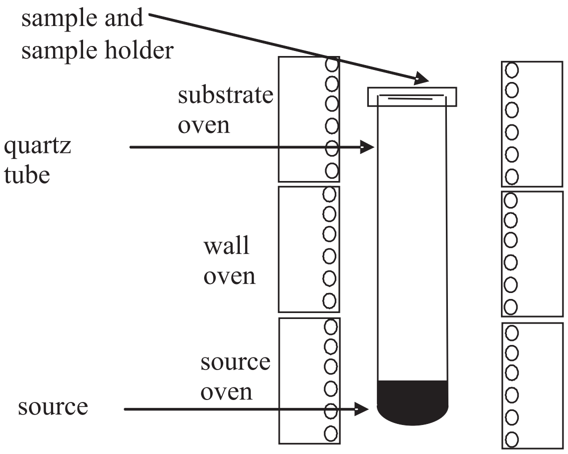

Figure 3.1: *Schematic cross-section of a Hot Wall Epitaxy system.*

vacuum. At the bottom of the quartz tube the source material is placed and heated by the source oven. The open end of the tube is closed by the substrate whose temperature is regulated by the substrate oven. The part between source and substrate is called the wall, and it is heated separately as well. Source and wall temperature are used to control the growth rate.

The great advantage of HWE is the closed growth reactor. It is beneficial for several reasons. It allows a uniform flow of evaporated molecules onto the substrate surface and prevents material loss. Furthermore, it enables a thin film growth near to the thermodynamic equilibrium; this is of great importance for epitaxial growth in general, and in particular for weakly bound organic molecular crystals.

Chapter 4

Investigation of crystallographic properties

4.1 Diffraction theory

The main investigation techniques used in this work are based on elastic scattering of monochromatic electromagnetic (EM) waves. The interaction of EM waves with crystalline matter gives rise to diffraction, provided their wavelength is comparable to the dimensions of crystal periodicities. This requirement is fulfilled by x-rays; because of the wave-particle duality, one is not restricted to EM waves and electrons and neutrons are frequently used matter waves. In this work, we have used x-ray and electron diffraction to probe crystallographic properties of organic thin films. Before discussing the used investigation techniques in detail, a short introduction on the principles of diffraction will be given in the following. This chapter is based on Ref. [83] and references therein.

4.1.1 Laue equations

A monochromatic electromagnetic wave is characterized by its energy W, which is easily related to the frequency ν or the wavelength λ:

$$W = h\nu = \hbar\omega = \hbar\frac{2\pi c}{\lambda}. \tag{4.1}$$

When describing diffraction phenomena, the propagation direction of the wave $\boldsymbol{s}$ has to be taken into account; this is done by the definition of the wave vector $\boldsymbol{k}$:

$$\boldsymbol{k} = |\boldsymbol{k}|\boldsymbol{s} = \frac{2\pi}{\lambda}\boldsymbol{s}. \tag{4.2}$$

Only elastic scattering (Thomson scattering) gives rise to diffraction, meaning that the energy of the interacting EM wave is conserved. This means, the direction of the wave vector changes but not its magnitude:

$$|\boldsymbol{k}| = |\boldsymbol{k'}|, \tag{4.3}$$

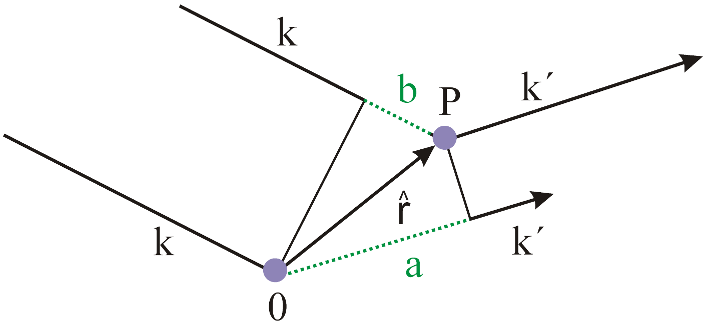

Figure 4.1: *Path difference between two waves scattered at **0** and **P**, respectively.*

where $\boldsymbol{k}$ is the wave vector of the incoming wave, and $\boldsymbol{k'}$ of the scattered (cf. Fig. 4.1).

The electric field strength of the incoming wave $\boldsymbol{E}$ is described by a plane wave, where $\boldsymbol{E}_0$:

$$\boldsymbol{E}(\boldsymbol{r}) = \boldsymbol{E}_0 \exp i(\boldsymbol{k} \cdot \boldsymbol{r} - \omega t), \tag{4.4}$$

and induces at each scattering center an oscillation of crystal electrons with the same frequency. The induced dipoles emit spherical waves, which in the far-field approximation are described by a plane wave as well:

$$\boldsymbol{E'}(\boldsymbol{r}) = \boldsymbol{A} \exp i(\boldsymbol{k} \cdot \boldsymbol{r} - \omega t) \exp i\phi. \tag{4.5}$$

Here, A denotes the scattering amplitude. Diffraction is a cooperative phenomenon resulting from a superposition of waves diffracted by different scattering centres. The resulting interference of emitted waves depends on their phase angles ϕ. Here, the path difference between two scattering centres (0, P) is derived (Fig. 4.1). It is further assumed that the incoming wave is scattered only at one center (kinematical approximation). The path difference of the waves which are scattered at centres 0 and P are given by a difference between a and b; these distances are projections of $\hat{\boldsymbol{r}}$ onto the incoming $\boldsymbol{k}$ and outgoing wave vector $\boldsymbol{k'}$, respectively:

$$\phi = \hat{\boldsymbol{r}}(\boldsymbol{k} - \boldsymbol{k'}) = \hat{\boldsymbol{r}}\Delta\boldsymbol{k}. \tag{4.6}$$

The difference between the incoming and the outgoing wave vector is crucial for interference phenomena and is therefore introduced as a physical quantity denoted as scattering vector $\boldsymbol{q}$:

$$\boldsymbol{q} := (\boldsymbol{k} - \boldsymbol{k'}) = \Delta\boldsymbol{k} \tag{4.7}$$

The second quantity which has to be taken into account (cf. Eq. 4.6) is the distance between the two scattering centres $\hat{\boldsymbol{r}}$. Accounting for all scattering centres (by integration) leads to the intensity diffracted from the whole crystal ($I \propto |\boldsymbol{E'}(\boldsymbol{r})|^2$). Note that diffraction only occurs in case of *coherent* scattering. Only if the relative phases of the scattering centres are preserved, does the integration over all scattering centres lead to constructive and destructive interference. As discussed in Sec. 2.1, only a discrete number of lattice points exists and they can be described by lattice vectors:

$$\boldsymbol{R}_{n_1 n_2 n_3} = n_1\boldsymbol{a} + n_2\boldsymbol{b} + n_3\boldsymbol{c}, \tag{4.8}$$

where n_1, n_2, n_3 are integers and $\boldsymbol{a}$, $\boldsymbol{b}$, $\boldsymbol{c}$ are the unit vectors of a crystal lattice. Therefore, the integration over the whole crystal can be reduced to a summation over all lattice points:

$$\begin{aligned}
\boldsymbol{E}'(\boldsymbol{r}) &= \boldsymbol{A} \sum_{n_1,n_2,n_3} \exp i[\boldsymbol{k}\cdot\boldsymbol{r} + (\boldsymbol{q}\cdot\boldsymbol{R}_{n_1 n_2 n_3})] \\
&= \boldsymbol{A} \exp i(\boldsymbol{k}\cdot\boldsymbol{r}) \sum_{n_1,n_2,n_3} \exp i[\boldsymbol{q}\cdot(n_1\boldsymbol{a} + n_2\boldsymbol{b} + n_3\boldsymbol{c})] \qquad (4.9) \\
&= \boldsymbol{A} \exp i(\boldsymbol{k}\cdot\boldsymbol{r}) \sum_{n_1} \exp in_1(\boldsymbol{a}\cdot\boldsymbol{q}) \sum_{n_2} \exp in_2(\boldsymbol{b}\cdot\boldsymbol{q}) \sum_{n_3} \exp in_3(\boldsymbol{c}\cdot\boldsymbol{q}).
\end{aligned}$$

The condition for a maximum of $\boldsymbol{E}'(\boldsymbol{r})$, and thus of the scattered intensity, is well-defined: the dot products in the sums have to equal an integer multiple of 2π. These are the so-called *Laue conditions*:

$$\begin{aligned}
\boldsymbol{a}\cdot\boldsymbol{q} &= 2\pi\hat{h} \\
\boldsymbol{b}\cdot\boldsymbol{q} &= 2\pi\hat{k} \\
\boldsymbol{c}\cdot\boldsymbol{q} &= 2\pi\hat{l}.
\end{aligned} \tag{4.10}$$

Here, the symbols $\hat{h}, \hat{k}, \hat{l}$ (*Laue indices*) are integers and correspond to the *diffraction order.*

For the derivation of the scattered intensity in Eq. 4.13 0-dimensional scattering centres sited on lattice points are assumed. In general, that is not the case and the position of the *basis* has to be taken into an account:

$$\boldsymbol{R}_{j,n_1 n_2 n_3} = (n_1 + x_j)\boldsymbol{a} + (n_2 + y_j)\boldsymbol{b} + (n_3 + z_j)\boldsymbol{c}, \tag{4.11}$$

To perform the summation over the whole crystal according to the Eq. 4.13 one has to substitute Eq. 4.8 by Eq. 4.11. Additionally, now the scattering amplitude depends on the position $\boldsymbol{r}_j$ of the basis:

$$\begin{aligned}
\boldsymbol{E}'(\boldsymbol{r}) &= \sum_{n_1,n_2,n_3} \sum_j \boldsymbol{A}(\boldsymbol{r}_j) \exp i[\boldsymbol{k}\cdot\boldsymbol{r} + (\boldsymbol{q}\cdot\boldsymbol{R}_{n_1 n_2 n_3}) + (\boldsymbol{q}\cdot\boldsymbol{r}_j)] \qquad (4.12) \\
&= \exp i(\boldsymbol{k}\cdot\boldsymbol{r}) \sum_j \underbrace{\boldsymbol{A}(\boldsymbol{r}_j) \exp(\boldsymbol{q}\cdot\boldsymbol{r}_j)}_{\boldsymbol{F}(\boldsymbol{\Delta k})} \sum_{n_1,n_2,n_3} \exp i[\boldsymbol{q}\cdot(n_1\boldsymbol{a} + n_2\boldsymbol{b} + n_3\boldsymbol{c})] \\
&= \boldsymbol{F}(\boldsymbol{\Delta k}) \exp i(\boldsymbol{k}\cdot\boldsymbol{r}) \sum_{n_1} \exp in_1(\boldsymbol{a}\cdot\boldsymbol{q}) \sum_{n_2} \exp in_2(\boldsymbol{b}\cdot\boldsymbol{q}) \sum_{n_3} \exp in_3(\boldsymbol{c}\cdot\boldsymbol{q}).
\end{aligned}$$

The expression $\boldsymbol{F}(\boldsymbol{\Delta k})$ is called *structure factor* and determines the scattered intensity depending on the basis.

4.1.2 Reciprocal lattice

So far, the conditions have been derived which ensure that the collectively emitting dipoles sited on crystal lattice points lead to an interference maximum (see Eq. 4.10). To satisfy equation 4.10, a proper $\boldsymbol{q}$ has to be found, which multiplied by the unit vectors of a given crystal structure ($\boldsymbol{a}$, $\boldsymbol{b}$, $\boldsymbol{c}$) yields an integer manifold of 2π.

The concept of the *reciprocal lattice* was introduced to solve the Laue conditions. The basis vectors of a reciprocal lattice are constructed by the following rule:

$$\boldsymbol{a}^* = 2\pi\frac{\boldsymbol{b}\times\boldsymbol{c}}{\boldsymbol{a}(\boldsymbol{b}\times\boldsymbol{c})} \qquad \boldsymbol{b}^* = 2\pi\frac{\boldsymbol{c}\times\boldsymbol{a}}{\boldsymbol{a}(\boldsymbol{b}\times\boldsymbol{c})} \qquad \boldsymbol{c}^* = 2\pi\frac{\boldsymbol{a}\times\boldsymbol{b}}{\boldsymbol{a}(\boldsymbol{b}\times\boldsymbol{c})}, \tag{4.13}$$

where $\boldsymbol{a}$, $\boldsymbol{b}$, $\boldsymbol{c}$ are the lattice vectors of a given crystal structure. From the construction of the reciprocal unit vectors it is obvious that, e.g.,$\boldsymbol{a}^*$ is perpendicular to the unit vectors $\boldsymbol{b}$, $\boldsymbol{c}$. In analogy to the real space crystal lattice (cf. 4.14), the reciprocal lattice vectors are defined as follows:

$$\boldsymbol{R}^*(hkl) = \hat{h}\boldsymbol{a}^* + \hat{k}\boldsymbol{b}^* + \hat{l}\boldsymbol{c}^*. \tag{4.14}$$

Here, $(\hat{h}\hat{k}\hat{l})$ are *Laue indices* as used in Eq. 4.10. The integers (hkl) are called *Miller indices* and correspond to a family of lattice planes in the real space. They are given by the three points where a lattice plane intersects the unit vectors: $\frac{\boldsymbol{a}}{h}$, $\frac{\boldsymbol{b}}{k}$ and $\frac{\boldsymbol{c}}{l}$. This means, the (hkl) values are reciprocal to the intersection ratios of the unit vectors. The relation between Laue and Miller indices is given by:

$$(\hat{h}\hat{k}\hat{l}) = n(hkl), \tag{4.15}$$

where n is an integer.

The Laue conditions Eq. 4.10 are exactly satisfied by substituting $\boldsymbol{q}$ for $\boldsymbol{R}^*(hkl)$:

$$\begin{array}{lll} \boldsymbol{a}\cdot\boldsymbol{a}^* = 2\pi & \boldsymbol{a}\cdot\boldsymbol{b}^* = 0 & \boldsymbol{a}\cdot\boldsymbol{c}^* = 0 \\ \boldsymbol{b}\cdot\boldsymbol{a}^* = 0 & \boldsymbol{b}\cdot\boldsymbol{b}^* = 2\pi & \boldsymbol{b}\cdot\boldsymbol{c}^* = 0 \\ \boldsymbol{c}\cdot\boldsymbol{a}^* = 0 & \boldsymbol{c}\cdot\boldsymbol{b}^* = 0 & \boldsymbol{c}\cdot\boldsymbol{c}^* = 2\pi. \end{array} \tag{4.16}$$

The derived relationship means that constructive interference is observed when the scattering vector $\boldsymbol{q}$ equals a reciprocal lattice vector $\boldsymbol{R}^*$:

$$I \rightarrow max \Leftrightarrow \boldsymbol{q} = \boldsymbol{R}^*(hkl). \tag{4.17}$$

This is a vector equation; by varying the direction and the magnitude of the scattering vector $\boldsymbol{q}$ the reciprocal lattice can be mapped. The reciprocal lattice then in turn allows to deduce the crystal lattice in real space.

The reciprocal lattice vectors are reciprocally related to the interplanar lattice spacings of the real space lattice:

$$d(hkl) = \frac{2\pi}{|\boldsymbol{R}^{*}(hkl)|}, \tag{4.18}$$

which is of importance in the next subsection.

4.1.3 Bragg equation

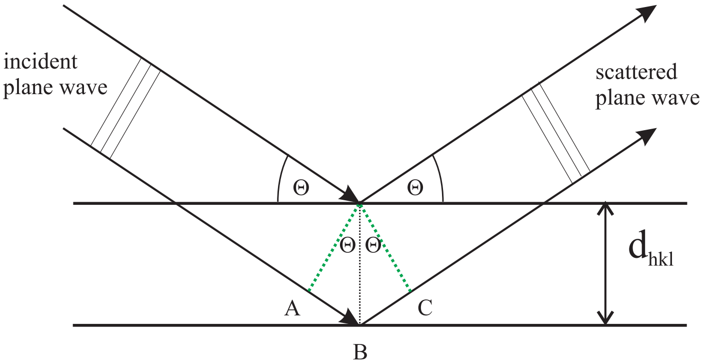

Figure 4.2: *Derivation of Bragg equation based on reflection geometry of a plane wave by lattice planes.*

An alternative description of Laue equations was given by W.H. Bragg (1913), which was derived from x-ray diffraction on crystal lattices. The arguing was, that the diffraction of order $(\hat{h}\hat{k}\hat{l}) = n\ (hkl)$ can be explained by a specular reflection of the incoming wave on lattice planes (hkl) having an interplanar spacing d_{hkl}. This situation is schematically shown in Fig. 4.2. The incoming x-ray is not only reflected by the surface; it penetrates the crystal and is diffracted on consecutive lattice planes as well. In specular geometry incident and reflected waves enclose an equal angle θ with the lattice planes. Constructive interference occurs when the path difference of waves reflected on consecutive lattice planes equals an integer multiple of the wavelength.

The path difference between the waves diffracted on the consecutive lattice planes is easily derived from the sketch shown in Fig. 4.2. It equals the sum of $\overline{AB}$ and $\overline{BC}$ distances, which both have a magnitude of $d_{hkl} sin\theta_B$. Therefore, the condition of constructive interference is given by the so-called *Bragg equation*:

$$n\lambda = 2d_{hkl}\sin\theta_B \tag{4.19}$$

$$\lambda = 2d_{\hat{h}\hat{k}\hat{l}}\sin\theta_B, \tag{4.20}$$

where n is the reflection order. This means, for a given wavelength λ the reflection on particular lattice planes with the interplanar distance d_{hkl} occurs at a specific angle, which is termed *Bragg angle* θ_B.

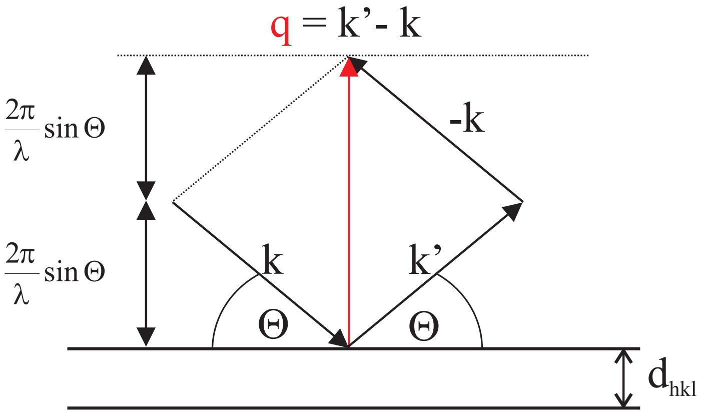

Figure 4.3: *Specular diffraction geometry.*

The Bragg equation can be derived directly from the solution of Laue conditions Eq. 4.10 as well. The illustration for this approach is shown in Fig. 4.3. The magnitude of the scattering vector (together with Eq. 4.2) is expressed by:

$$|\boldsymbol{q}| = \frac{4\pi \sin\theta}{\lambda}. \tag{4.21}$$

On the other side $|\boldsymbol{q}|$ has to satisfy the Eq. 4.18 as well:

$$|\boldsymbol{q}| = \frac{2\pi}{d_{hkl}}. \tag{4.22}$$

The combination of these two equation yields the Bragg equation.

4.2 X-Ray diffraction

In the following, two complementary x-ray diffraction techniques will be presented, which have been used in this work for the investigation of organic thin films. The combination of these techniques allows to unambiguously determine the epitaxial relationship between the organic thin film and the underlying substrate surface.

4.2.1 Specular scans

An x-ray diffractometer used for the measurement of specular scans is shown in Fig. 4.4. It is composed of an x-ray tube (the wavelength of the characteristic radiation is determined by the anode material), a goniometer to which the sample is mounted and an x-ray detector which measures the intensity diffracted by the sample.

Here, the scattering geometry is identical to that used to derive the Bragg equation (Fig. 4.2): the incoming wave vector encloses the same angle as the outgoing wave in respect to sample surface. By using a diffractometer as shown in Fig. 4.4 the incident angle is defined by the tilt of the sample holder in respect to an x-ray tube, and the angle of the measured diffracted wave by the position

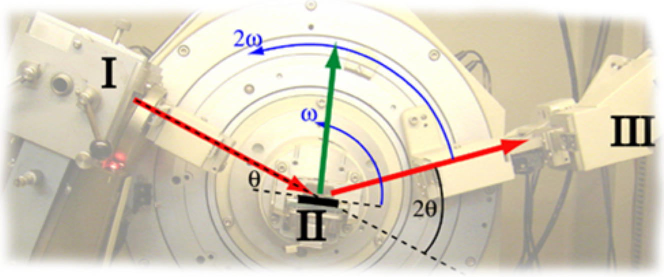

Figure 4.4: *An x-ray diffractometer in a specular diffraction geometry.*

of the detector. To realize a specular measurement geometry the detector is moved with the doubled angular velocity (2ω) of the sample holder (ω). The prolonged incident beam encloses an angle of 2θ with the detector; specular scans are therefore denoted as $\theta/2\theta$-scans as well.

Figure 4.5 illustrates the scattering geometry in respect to the sample surface. The incoming **k** and the scattered **k'** wave vectors span the so-called scattering plane. Scattering vector $\boldsymbol{q}$ is exactly the bisection between the incoming and outgoing wave vectors, and lies therefore within the scattering plane (*co-planar scattering*). A consequence of the specular measurement geometry is that the scattering vector is always *perpendicular* to the sample surface.

For a better understanding of scattering measurements the vector solution of Laue equations 4.18 can be divided into two scalar equations: (i) the direction as well as (ii) the magnitude of the scattering vector $\mathbf{q}$ has to equal to a reciprocal lattice vector $\boldsymbol{R}^*(hkl)$. As discussed in the subsection 4.1.2, reciprocal lattice vector $\boldsymbol{R}^*(hkl)$ is perpendicular to lattice planes hkl (i.e. parallel to the lattice plane normal vector). The specular measurement geometry therefore implies that only lattice planes which are parallel to the sample surface satisfy part (i) of the Laue equations. The (ii)-part of the Laue equations is described by the Bragg equation. As the experiment is operated with monochromatic radiation, the magnitude of the scattering vector is solely determined by the angle θ. That means, by symmetrically varying θ and 2θ, the magnitude of the scattering vector is varied. Every time $\boldsymbol{q}$ corresponds to a reciprocal lattice point, a maximum in intensity is measured. Given a known wavelength λ, interplanar distances d_{hkl} can be determined via Bragg equation by measuring the θ angle where an intensity peak is observed.

4.2.2 Pole figure measurement

Above discussed *specular scans* provide the interplanar distances d_{hkl} of lattice planes which are oriented parallel to the substrate surface. Thus, a specular scan reveals a preferential orientation of organic crystallites in respect to the substrate surface (*out-of-plane order*). However, specular measurements do not allow to deduce a preferential azimuthal orientation on the substrate (*in-plane order*); this complementary information on the epitaxial relationship between the thin film and the underlying substrate is provided by pole figure measurements.

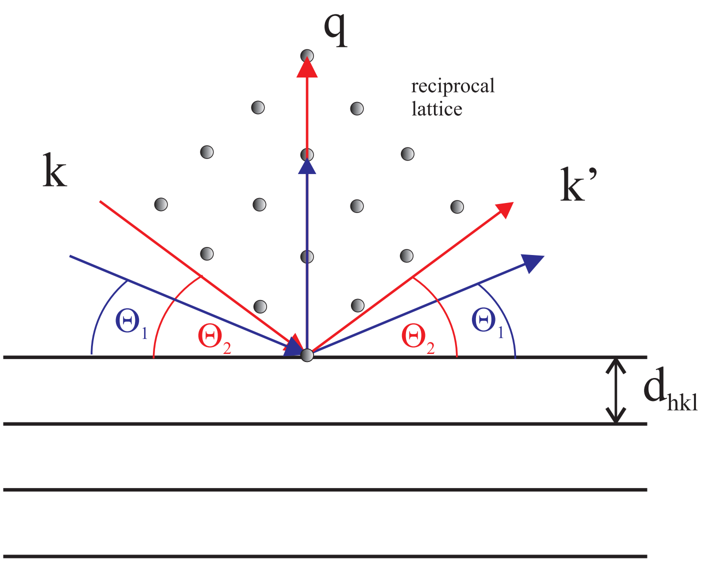

Figure 4.5: *Sketch illustrating the relation between the Bragg angle θ and the scattering vector $\boldsymbol{q}$.*

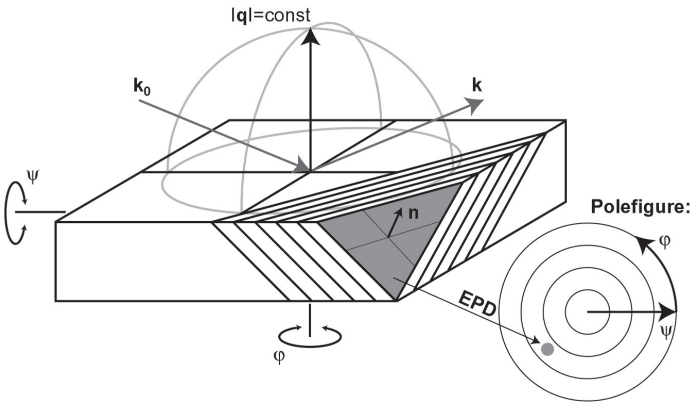

Figure 4.6: *Schematic of a pole figure measurement.*

The idea of pole figure measurements is to systematically tilt and rotate the sample and thereby ensure that the (i)-part of the Laue equation satisfied for any possible direction of the lattice plane normal. The principle of pole figure measurements is sketched in Fig. 4.6. If one wants to detect lattice planes which are not parallel to the sample surface (see Fig. 4.6), the sample has to be tilted by an angle ψ and rotated by an angle ϕ; in this orientation the condition (i) is satisfied. To fulfil the (ii)-part of Laue conditions, the pole figure has to be measured for the Bragg angle θ_B which corresponds via Bragg equation 4.20 to the interplanar distance d_{hkl}.

These measurements are performed on a diffractometer equipped with an Eulerian cradle, having four angular degrees of freedom (ω, 2θ, ψ, ϕ). A pole figure is measured at a constant Bragg angle $\theta_B/2\theta_B$ which is for a known d_{hkl}

calculated by the Bragg equation. During the measurement the sample is tilted in $\Delta\psi$-steps about the ψ-axis in the range $\psi = 0° \ldots 90°$. For every tilt in ψ a ϕ-scan is performed, where the sample is rotated by 360° in ϕ, i.e. about its own axis. By this systematic tilting and rotating it is ensured that for some combination of ψ and ϕ, the normal vector of the probed lattice plane will become parallel to the scattering vector and Laue equations will be satisfied. The intensities measured for (ψ, ϕ)-pairs are plotted in a polar plot (see Fig. 4.6); occurring diffraction spots are denoted *enhanced pole densities* (EPDs). The reciprocal space can be efficiently probed by measuring pole figures for different d_{hkl}.

For the evaluation of the measured pole figures, a stereographic projection for the lattice planes satisfying the Bragg equation is calculated and the calculated (ψ,ϕ)-positions are compared to the measured EPD. For the calculation of a stereographic projection one has to assume a center of projection which corresponds to the lattice plane parallel to the substrate surface. This information is usually obtained by specular scans. For an unambiguous determination of the in-plane alignment, about three pole figures have to be evaluated consistently.

If the crystal structure is unknown, the angle couple $\theta/2\theta$ is varied systematically as well. If the $\Delta\theta$-step is chosen smaller than the divergence of the x-ray beam, the whole relevant reciprocal space can be mapped.

Combining XRD specular scans with pole figure measurements allows for an efficient determination of the epitaxial relationship between the thin film and the underlying substrate. The epitaxial relation is unambiguously determined by (i) the lattice plane of the film being parallel to the substrate surface (out-of-plane orientation) and (ii) the orientation of the thin film crystal within plane parallel to the substrate surface (in-plane orientation). Specular scans provide information concerning the out-of-plane orientation. The relative in-plane orientation is determined by measuring pole figures of the thin film as well as of the substrate. This allows to determine lattice directions of the thin film crystal which are oriented parallel to lattice directions within the substrate surface.

4.3 Transmission electron microscopy

The following section is based on [84, 85] and references therein.

Due to the wave-particle duality, interaction of accelerated electrons with matter leads to diffraction phenomena. In a transmission electron microscope an electrically heated cathode emits electrons which are accelerated to an anode. The acceleration voltage usually lies between 80-200 kV and determines the wavelength of the electrons. It reads (in the non-relativistic approximation):

$$\lambda = \frac{h}{\sqrt{2m_0 eU}} = \frac{38.78}{\sqrt{U[kV]}}[\mathrm{pm}]. \tag{4.23}$$

Electrons have the advantage to be easily focusable via magnetic fields. In

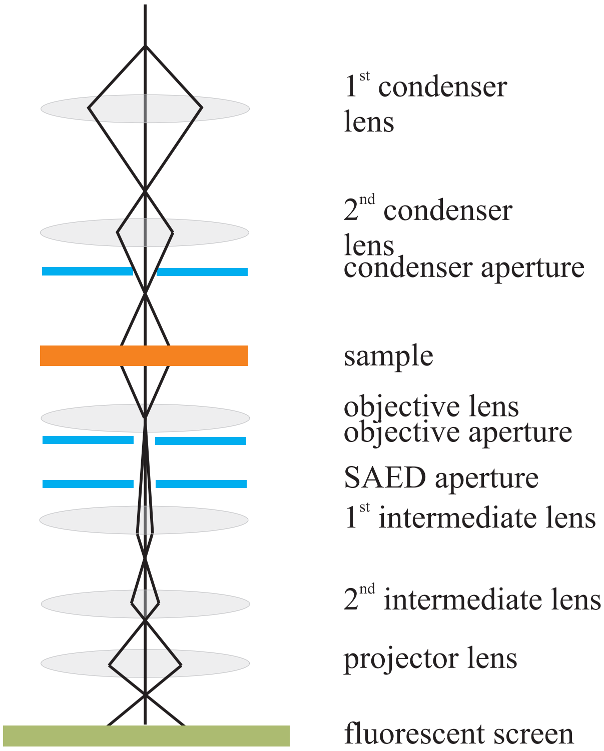

Figure 4.7: *Path of the electron beam in a TEM set-up.*

addition to diffraction measurements, electrons also enable imaging the real space and allows displaying the morphology of the sample. A transmission electron microscope (TEM) can be operated in a diffraction or image mode. Switching between the two modes enables establishing a correlation between the real- and reciprocal space.

4.3.1 Imaging modes

The centrepiece of a transmission electron microscope are magnetic lenses used for focussing the electrons. Figure 4.7 schematically shows optical components incorporated in a TEM. The electron beam is first modelled by a condenser system, consisting of an aperture and two condenser lenses. The beam cross-over is demagnified by the first condenser lens, while the second condenser lens models its convergence and the effective size on the sample. After passing the condenser system electrons impinge onto the sample; they interact with the sample atoms and are transmitted again. Directly below the sample the objective lens is placed, which forms the image of the sample. Figure 4.8 shows in more detail the ray path formed by the objective lens. On the one hand, it creates a real-space image of the sample in the image plane, which can be magnified by the subsequent lenses. On the other hand, it provides a diffraction pattern stemming from the sample. Electrons diffracted by the same Bragg angle θ_B form parallel rays which are focused into one point in the back focal plane thus giving the diffraction pattern (i.e. Fourier transform) of the sam-

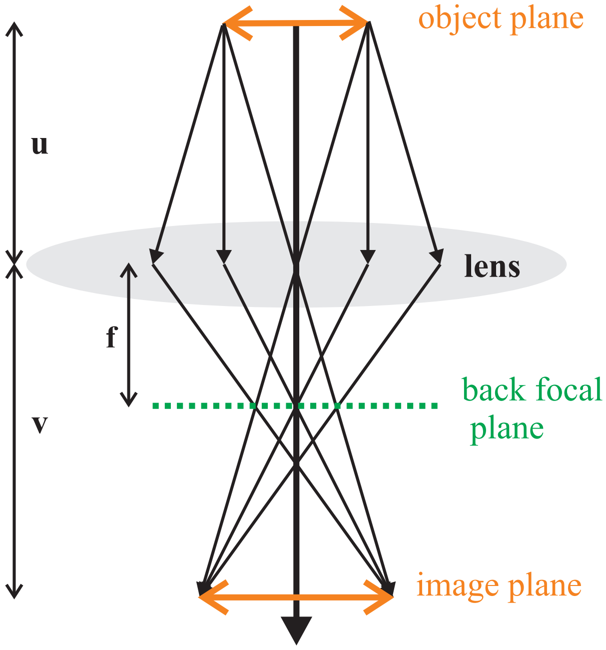

Figure 4.8: *The ray path of electrons through an objective lens.*

ple. The objective lens aperture is placed in this plane and depending on the imaging mode, it selects which part of the beam contributes to the final image. The intermediate lens can be focussed either on the image or on the back focal plane, thus yielding either a real space or a reciprocal space image. Finally, the projector lens generates the image onto a fluorescent screen. The following paragraphs describe different operating modes of a transmission electron microscope used in this work.

Bright field imaging

In the bright field (BF) mode the objective aperture allows the direct beam to pass and blocks the diffracted beams out. Additionally, the intermediate lens is focussed onto the image plane, where the real space image of the sample is formed. The contrast in TEM bright field images can be divided into two contributions: mass-thickness (i) and diffraction contrast (ii). Contribution (i) is caused by Rutherford scattering, which scales with the squared atomic number Z^2. Scattering on atoms with a large Z leads to stronger deflection of impinging electrons; thus these regions appear darker in the image. The same effect is present if the sample is not homogeneous: thicker parts cause stronger scattering of electrons and appear darker in the image. Contribution (ii) (diffraction contrast) depends on the size of the objective aperture. In the bright field mode only the direct beam passes through; all diffracted beams are suppressed. Therefore, crystalline regions deflecting electrons by diffraction appear dark in the BF image.

Electron diffraction

In the diffraction mode, the objective aperture allows also the diffracted beams to pass. The intermediate lens is focussed on the back focal plane; hence, the diffraction pattern is projected onto the fluorescence screen.

An aperture placed in the image plane of the objective lens allows to perform the diffraction experiment only on a particular part of the sample. This is the so-called selected area electron diffraction (SAED) which allows to correlate crystallographic properties to specific morphologies.

Dark field imaging

In the dark field image mode the objective aperture suppresses the direct beam and selects an electron beam diffracted by a specific θ_B (corresponds to a specific lattice plane distance d_{hkl}). In the formed real space image only regions of the sample where electrons are diffracted by θ_B appear bright and thus the homogeneity of the crystalline areas can be observed.

High resolution imaging

High resolution images allow depicting details in real space on the scale of atomic periodicities; these correspond to large values in the reciprocal space. However, in the bright field as well as in the dark field the objective aperture is placed in the back focal plane where the diffraction pattern is formed. Thus, due to the use of a objective aperture, the reciprocal range is truncated and details on small periodicities in the real space are lost. The relationship between the resolution in the real space Δx and in the reciprocal space δ is simply given by:

$$\Delta x = \frac{2\pi}{\delta k}. \tag{4.24}$$

This means, to gain atomic resolution d the corresponding range in the reciprocal space is needed: $\delta k = \frac{2\pi}{d}$. A k-range which is large enough to gain atomic resolution in general is achieved when the objective aperture is large enough to pass the direct beam as well as at least one diffracted beam. The diffracted beams containing information on atomic periodicities modulates the direct beam; this gives rise to high resolution images. The high resolution images rely on the phase relationships of the diffracted beams. However, up to now, phase distortion caused by the objective lens limits the spatial resolution to 1.7 Å.[85]

Part II

Results

Chapter 5

Substrate selected polymorphism of epitaxially aligned tetraphenyl-porphyrin thin films

The work presented in this chapter was published in the journal *Physical Chemistry Chemical Physics* and is essentially identical to the article. Figure 5.1 shows the title of the article and all contributing authors including their affiliations. *Phys. Chem. Chem. Phys., 2012, 14, 262-272 - Reproduced by permission of the PCCP Owner Societies. The original article is available online at the following link:* http://pubs.rsc.org/en/content/articlepdf/2012/cp/c1cp22299f

Abstract. Porphyrin molecules, of interest as versatile materials for organic electronics, are highly prone to formation of significantly different polymorphic phases. To elucidate the determinants for the specific polymorphic phase formed in thin films as well as for the arrangement of the molecules on a given substrate two different anisotropic substrate surfaces have been selected: KCl(100) and the oxygen reconstructed Cu(110) surface. We observe that the crystal structure of the thin films depends on the substrate, whereas the relative molecular orientations in both cases are similar. X-Ray and transmission electron diffraction of 30 nm thick tetraphenyl-porphyrin (H_2TPP) and platinum tetraphenyl-porphyrin (PtTPP) thin films deposited on KCl(100) surfaces reveals that both kinds of molecules crystallize in a tetragonal polymorph with the (001) lattice planes, i.e. with their macrocycles, parallel to the substrate. Films deposited on the oxygen reconstructed Cu(110)-(2x1)O surface exhibit in contrast the triclinic polymorph even though molecules again align nearly parallel to the substrate surface as observed by LEED and X-ray diffraction. On both substrates we identify two driving forces for the epitaxial alignment of porphyrins: (i) molecules aligning with their macrocycles (nearly) parallel to the substrate surface and (ii) the porphyrin molecules forming a commensurate unit cell with the respective substrate. The polymorphic phase meeting both requirements is the most favorable to be formed on a given substrate and due to this structural

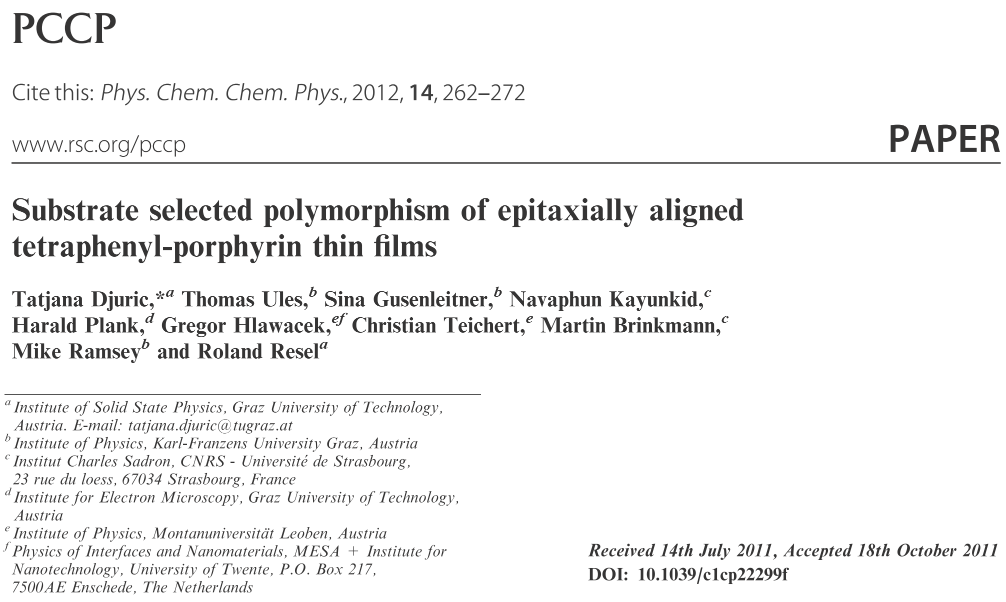

PCCP

Cite this: *Phys. Chem. Chem. Phys.*, 2012, **14**, 262–272

www.rsc.org/pccp

PAPER

Substrate selected polymorphism of epitaxially aligned tetraphenyl-porphyrin thin films

**Tatjana Djuric,*[a] Thomas Ules,[b] Sina Gusenleitner,[b] Navaphun Kayunkid,[c]
Harald Plank,[d] Gregor Hlawacek,[ef] Christian Teichert,[e] Martin Brinkmann,[c]
Mike Ramsey[b] and Roland Resel[a]**

[a] *Institute of Solid State Physics, Graz University of Technology, Austria. E-mail: tatjana.djuric@tugraz.at*
[b] *Institute of Physics, Karl-Franzens University Graz, Austria*
[c] *Institut Charles Sadron, CNRS - Université de Strasbourg, 23 rue du loess, 67034 Strasbourg, France*
[d] *Institute for Electron Microscopy, Graz University of Technology, Austria*
[e] *Institute of Physics, Montanuniversität Leoben, Austria*
[f] *Physics of Interfaces and Nanomaterials, MESA + Institute for Nanotechnology, University of Twente, P.O. Box 217, 7500AE Enschede, The Netherlands*

Received 14th July 2011, Accepted 18th October 2011
DOI: 10.1039/c1cp22299f

Figure 5.1: *Header of the article published in the journal Physical Chemistry Chemical Physics. It shows all contributing authors and the corresponding affiliations.*

flexibility in both cases well-ordered, epitaxially aligned porphyrin thin films are achieved.

5.1 Introduction

Predicting and controlling the crystal structure as well as the molecular alignment of organic thin films is of crucial importance for the performance of organic thin film devices.[86] Although often observed for crystals of organic molecules the phenomenon of polymorphism is still barely understood. Due to their weak and non-directional Van-der-Waals interactions, structures with significantly different molecular packings and thus different electronic properties can have similar lattice energies, i.e. in the thermodynamical sense have a similar likelihood of occurrence.[33,35,87]

In this study we focus on characterizing thin films of porphyrin molecules, a group of organic compounds often used in organic opto-electronics and showing a pronounced tendency to polymorphism.[54,57,58,88,89] Here, the crystal packing, molecular arrangement and morphological properties of epitaxially aligned thin films of tetraphenyl-porphyrin $C_{44}H_{30}N_4$ (H_2TPP) and its Pt-analogue $C_{44}H_{28}N_4Pt$ (PtTPP) are studied. H_2TPP molecules consist of four phenyl groups which are attached to a highly conjugated porphine skeleton (macrocycle); two out of four nitrogen atoms located in the center of the macrocycle are bound to hydrogen atoms (Fig. 5.2 a). The two hydrogen atoms are substituted by a platinum atom in the case of its metal complex PtTPP (Fig. 5.2 b). Two competing forces are determining the final molecular configuration of porphyrins in crystals. On the one hand a planar macrocycle is advantageous. It ensures the most effective π-π -orbital overlapping as the molecules prefer-

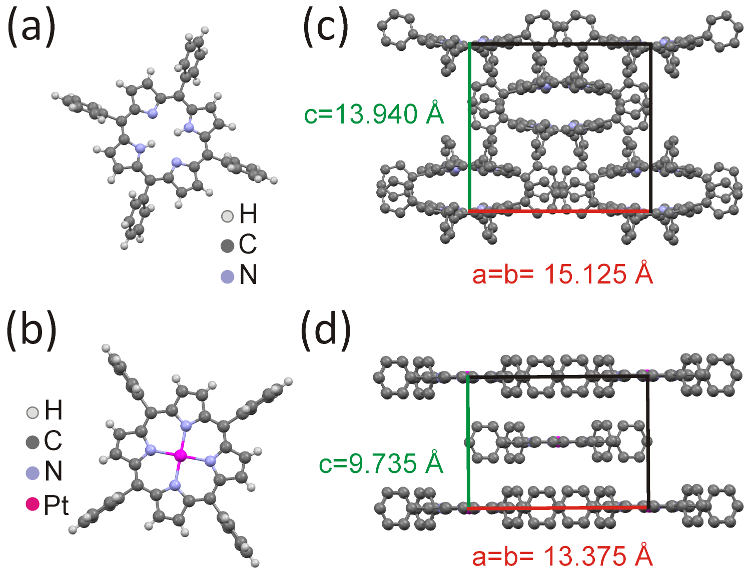

Figure 5.2: *(a) Molecular structure of H_2TPP* ($C_{44}H_{30}N_4$) *and (b) its Pt-analogue PtTPP* ($C_{44}H_{28}N_4Pt$). *Unit cells of the tetragonal polymorph I (c) and tetragonal polymorph II (d), respectively.*

entially stack parallel to each other. On the other hand, the molecules try to pack as close as possible. Since the porphyrin molecules are easily deformed, several crystal structures are reported where the close packing is realized inducing a bending of the macrocycle. In these crystal structures, the so called "ruffled" or "saddled" conformation is observed giving rise to the phenomenon of conformational polymorphism (i.e. molecules adopt varying conformations in different crystal lattices).[57,88,89] Though the bending and twisting of phenyl side groups in respect to the porphine skeleton is usually such that they are nearly perpendicular to the porphine skeleton, for specific polymorphic phases it also might significantly differ.

Due to the highly conjugated macrocycle and the tendency to crystallize with the macrocycles parallel to each other, porphyrins have been recognized as promising materials for organic electronic devices, such as light-emitting diodes[90,91] photovoltaic cells[92,93] or thin film transistors.[94,95] Additionally, the easy substitution of the two central hydrogen atoms by a metal atom allows tuning the specific electronic and optical properties.[96–98] Studies on thin films further show that those molecules form highly ordered arrays on various substrate surfaces. This is due to the high conformational flexibility of porphyrin molecules, which enables to adopt a conformation favorable for a specific substrate surface.[99,100]

Numerous recent studies have focused on the growth of porphyrins in ultra thin films solely using surface sensitive investigation techniques like LEED (low energy electron diffraction) and STM (scanning tunneling microscope). Such studies barely go beyond the first monolayer and have not investigated crystallographic properties of porphyrin multilayer films.[96,100–104] In the present study we go further: besides determining the impact of the substrate on the molecular arrangement we will explore which polymorphic phase most likely forms on a specific substrate.

Two different well-defined, anisotropic substrates were selected for this purpose. The KCl(100) surface exhibiting a square 2d unit cell, is a favored model surface reliably yielding epitaxial aligned films of organic molecules.[105,106] The second substrate, oxygen reconstructed copper (110) (Cu(110)-(2x1)O), provides a corrugated surface due to adsorbed oxygen atom rows oriented along the Cu[001] direction. For rodlike molecules it has been shown that the surface corrugation aligns the molecules and induces epitaxial order of the deposited molecules[80] and in the present work this will be demonstrated also for the plate-like porphyrin molecules. The crystallographic and morphological properties of the porphyrin thin films are determined using LEED, X-ray diffraction techniques (XRD), transmission electron microscopy/diffraction (TEM/TED) as well as atomic force microscopy (AFM).

5.2 Experimental section

5.2.1 Sample preparation

The oxygen reconstructed Cu(110) substrate surface was prepared by cleaning the copper crystal by repeated cycles of Ar^+-ion bombardment and annealing it to 800 K. Dosing 10 L [1 Langmuir (L) = 1 Torr ms] of oxygen on the clean Cu(110) crystal at 500 K forms a p(2x1) added-row reconstruction which chemically polishes the surface.[107] The resulting terraces are up to hundreds of nanometers wide and separated by monoatomic steps. In addition, oxygen exposure not only flattens out the substrate but also passivates it with respect to aromatic adsorption. The KCl(100) substrates were produced by cleaving a KCl single crystal under UHV with a homemade cleaver along the (100) plane. The H_2TPP as well as PtTPP was deposited in situ from a thoroughly degassed evaporator with a pressure of 10^{-10} mbar. Nominal growth rates of 1.5 Åmin^{-1}, as monitored by a quartz microbalance, assuming a density of 1.273 and 1.688 gcm^{-3}, respectively, were used.

5.2.2 Low energy electron diffraction measurements

Low energy electron diffraction (LEED) experiments were performed in situ under ultra high vacuum on an Omicron MCP-LEED. Here, a micro channel plate is used to amplify electrons being backscattered by the sample. Due to this amplification only a low emission current in nA range is needed. The low primary beam current of the MCP-LEED allows sensitive samples, such as the studied porphyrin thin films, to be investigated without causing damage induced by higher beam current. In order to preserve the momentum of electrons parallel to the sample $k_{||}$, in the LEED pattern display a fringe field correction plate is used. However, close to the edge of the LEED screen little distortion is seen.

With this setup a transfer width greater than 25 nm at 100 eV beam energy is reached.

5.2.3 X-ray diffraction measurements

The in situ prepared and characterized porphyrin multilayer films were removed from an UHV chamber for subsequent X-ray diffraction (XRD) measurements. Using a Philips X'pert X-ray diffractometer with CrK$_\alpha$ radiation specular scans and pole figure measurements were performed. The measurement geometry of specular scans ensures that the scattering vector is always parallel to the surface normal of the substrate. By continuously varying its magnitude, lattice periodicities perpendicular to the substrate surface are probed determining the lattice planes of the thin film oriented parallel to the substrate surface.

In contrast, pole figures are measured by keeping the magnitude of the scattering vector constant (e.g. choosing a specific lattice plane distance to be measured) while systematically changing its direction. Thereby, the distribution of lattice plane orientations of the substrate as well as of the organic thin film is obtained. From these measurements the azimuthal orientation of the thin film crystallites in respect to the substrate surface can be deduced. The simulation of pole figures was performed using STEREOPOLE[108] and for the assignment of the peak positions measured in the specular scans POWDER CELL[109] was used. The diffraction patterns of the H_2TPP and PtTPP powders were measured with a Siemens D501 diffractometer in the focusing Bragg-Brentano geometry using CuK$_\alpha$ radiation with a secondary graphite monochromator. The powder diffraction patterns were refined using the software MAUD.[110]

5.2.4 Transmission electron diffraction measurements

TEM was used as a complementary technique to determine the spatially resolved structure of the porphyrin films grown on KCl. The carbon coated H_2TPP and PtTPP films were removed from the KCl substrate by floating onto water and were subsequently recovered onto TEM copper grids. TEM investigations were performed in bright field (BF) and selected area electron diffraction (SAED) modes using a Philips CM electron microscope (120 keV) equipped with a MVIII CCD camera. Calculation of the electron diffraction (ED) patterns was performed using WebEMAPS.[111]

5.2.5 Atomic Force Microscopy Measurements

Atomic ForceMicroscopy (AFM) measurements were performed ex situ using a Digital Instruments MultiMode AFM operated with a Nanoscope IIIa controller and a Digital Instruments Dimension 3100 AFM operated with a Nanoscope IVa controller. Regular silicon cantilevers with a typical resonance frequency of 300 kHz were used in tapping mode. The use of tapping mode ensures minimal lateral forces between the tip and the sample to preserve the original surface morphology of these sensitive films. Gwyddion[112] and NanoScope [Version 1.2 by VEECO, 2010] software packages have been used for image analysis

5.3 Results

5.3.1 Powder diffraction

To specify to which extent the crystal structures formed in thin films depend on the nature of the substrate, the crystal structure of the "as-delivered" porphyrin powders used for the preparation of the thin films was investigated by X-ray diffraction. The diffraction pattern obtained for the H_2TPP powder (Fig. 5.3 a) is in a good agreement with the simulated pattern of a body centered tetragonal structure reported by Hamor et al. (a=b=15.125 Å , c=13.940 Å; see Fig. 5.2 c)[88] though the unit cell parameters are slightly shifted to larger values: a=b=15.2215 Å , c=13.97 Å. Within small variations in the unit cell parameters identical crystal structure is also reported for many metal-substituted porphyrins such as CuTPP,[89] PdTPP, NiTPP[89] as well as for PtTPP.[57] The macrocycle lying in the (a,b) plane is ruffled and the porphyrin molecules are stacking along the c-direction. This structure exhibits the I$\bar{4}$2d space group, while the molecular symmetry is assigned to the D2d ($\bar{4}$2m) point group,[18] which accounts for the bended structure of the macrocycle. The two opposed phenyl rings do not lie in the same plane. They are twisted by an angle of 23° in respect to each other and enclose angles of 78.51° with the mean plane of the macrocycle.

Though, only this crystal phase is explicitly reported for PtTPP,[57] the diffraction pattern observed for the PtTPP powder (Fig. 5.3 b) reveals a different body centered tetragonal unit cell, which is isomorphic (i.e. unit cell parameters are closely similar) with the structure previously reported for CuTPP:[58] a=b=13.3747 Å, c=9.7348 Å (Fig. 5.3 d). Taking the reported CuTPP structure as a starting-point, the copper atoms were replaced by platinum atoms and the lattice parameters were slightly refined with a least-squares approach using the software MAUD (a = b= 13.345 Å, c = 9.719 Å). The lattice spacings calculated by using this adapted structure (black line) are in perfect accordance with the measured diffraction pattern (red line). There is a slight discrepancy in the intensity ratio probably induced by a preferential orientation of the crystallites due to the preparation of the powder for the measurement. Like in the tetragonal structure observed for H_2TPP, the porphyrin molecules are stacked along the c-axis, but here the macrocycles are perfectly flat lying in the (a,b)-plane with phenyl groups perpendicular to it. The planar skeleton is described by the C4h (4/m) symmetry and this structure belongs to the I4/m space group.

It is worth emphasizing that in the observed crystal structures the Pt-analogue PtTPP adopts a planar structure in contrast to the metal-free H_2TPP molecules. This peculiarity of porphyrin systems was already observed in the 1960s[88,89] and points out that it is not the substitution with a metal atom which induces a conformational change leading to ruffled or saddle-like geometries but rather the specific forces of a given crystal structure. As the porphyrin molecules are easily deformable, crystal packing forces affect the final conformation of the molecules and therefore conformational polymorphism in porphyrin

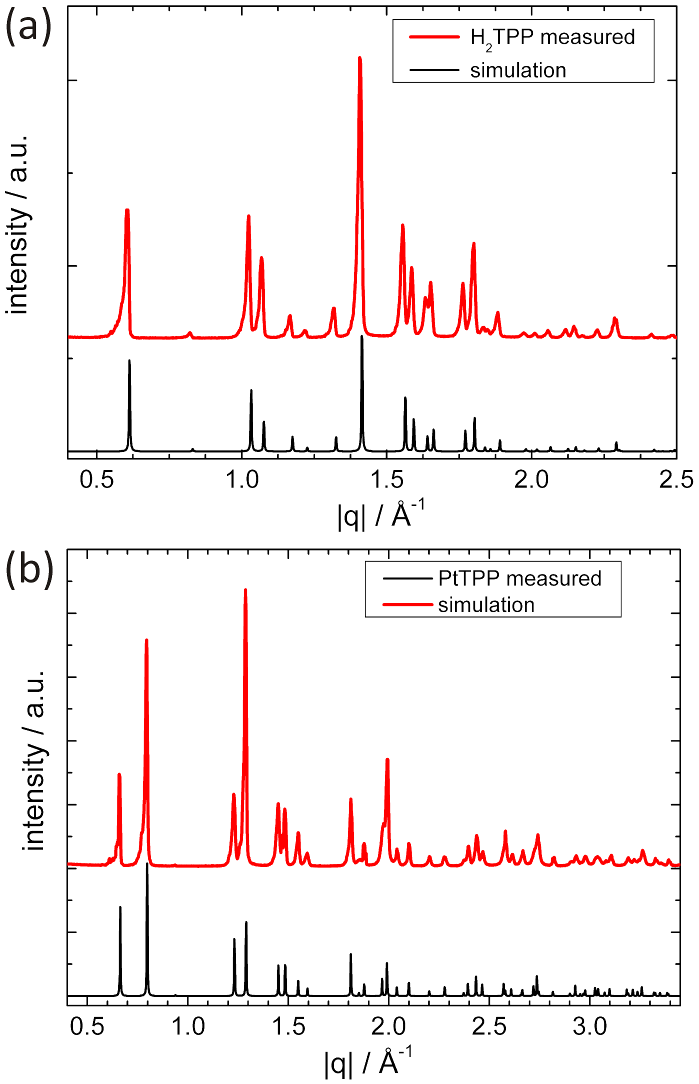

Figure 5.3: *(a) Diffraction pattern of the* H_2TPP *powder can be assigned to the tetragonal unit cell with the lattice parameters: a=b=15.125 Å, c = 13.940 Å tetragonal polymorph I). (b) The diffraction pattern for the PtTPP powder reveals a different tetragonal unit cell described by the following unit cell parameters: a = b = 13.3747 Å, c = 9.7348 Å (tetragonal polymorph II). The black lines in both cases show the simulated peak positions and intensities based on the assigned crystal structures.*

crystals is often observed. For the purpose of readability the tetragonal phase observed for the H_2TPP powder will be defined as “tetragonal polymorph I”, the phase observed for the PtTPP powder as “tetragonal polymorph II”.

5.3.2 Structure and alignment of tetraphenyl-porphyrins on KCl(100)

Thin films (30 nm) of H_2TPP and PtTPP on UHV cleaved KCl(100) substrates were prepared as described in the experimental section 5.2.1. Due to the strong charging of the KCl substrate under the electron beam, in-situ LEED measurements could not be performed. However, the KCl substrates are easily dissolved in water thus making the sample preparation for the TEM measurement unchallenging. To determine the epitaxial alignment of porphyrin molecules in respect to the substrate surface, XRD measurements were performed. To relate the morphology of the thin films to the principle symmetry axes of the substrate AFM measurements were performed.

Transmission electron microscopy

The bright field images of the PtTPP (Fig. 5.4 a) and H_2TPP (Fig. 5.4 d) films reveal similar morphologies: uniform coverage with hemispherical shaped crystallites aggregated to islands. Although the domains are not facetted and show rather smooth contours, they tend to align along preferential in-plane directions, suggesting epitaxial alignment by the KCl(100) substrate. The size of the aggregates in the case of the PtTPP film is in the range of 200 nm, while the H_2TPP film is composed of larger crystallites reaching dimensions even up to 500 nm. Very similar morphologies for porphyrin films grown on KCl(100) at room temperature were already reported.[113–115]

The electron diffraction (ED) pattern of PtTPP grown on KCl(100) shows remarkably sharp diffraction spots indicative of a strong epitaxial alignment by the KCl substrate (Fig. 5.4 b). A closer analysis reveals a superposition of two identical single crystal patterns which are rotated by 36° in respect to each other. The measured lattice spacings d_{hkl} can be assigned to the tetragonal polymorph II which was observed for the PtTPP powder ($a = 13.345$ Å, $c = 9.719$ Å, space group: I4/m).[58] The measured single crystal pattern is consistent with the calculated one of this structure assuming the [001] zone axis (Fig. 5.4 c). This zone axis corresponds to the (001) contact plane and implies that molecules orient with their flat macrocycles parallel to the substrate surface.

Figure 5.4 e shows the electron diffraction pattern observed for H_2TPP on KCl(100). Also here, we have two sets of identical single crystal patterns rotated by 36° in respect to each other. The measured lattice spacings e.g. $d_{110} = 0.94$ nm and $d_{020} = 0.67$ nm are the same as for the tetragonal polymorph II measured in the PtTPP film but interestingly the extinction rules imposed by the space group 87 are not fulfilled. Here, the reflection condition for the space group 87 (I4/m)regarding the (hk0) reflexes is not obeyed:

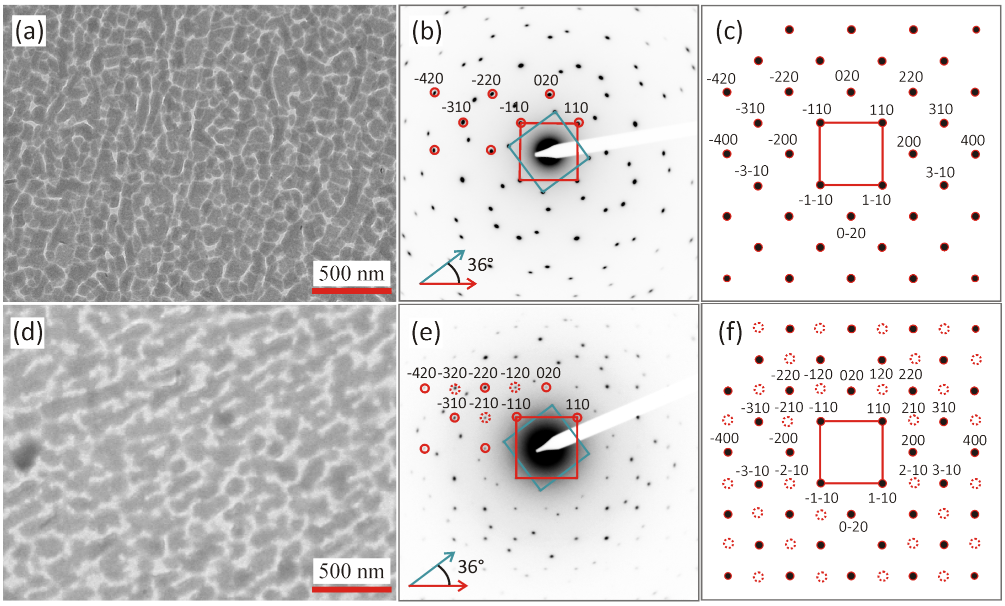

Figure 5.4: *(a) Bright field image of a PtTPP thin film (30 nm) grown on the KCl(100) substrate at room temperature. (b) Typical electron diffraction pattern of the PtTPP film reveals two single crystal diffraction patterns rotated by 361 in respect to each other. Panel (c) shows the calculated single crystal diffraction pattern assuming the [001] zone axis of the tetragonal polymorph II. (d) The bright field image of a H2TPP thin film (30 nm) grown on KCl(100) substrate at room temperature. (e) The diffraction pattern of the* H_2TPP *thin film is basically the same as in the case of PtTPP, but here additional reflexes are visible (denoted by dashed circles). (f) Thus, it can be also explained by the tetragonal polymorph II assuming the same zone axis [001] but taking also the systematical forbidden reflexes* $h + k \neq 2n$ *into account.*

$$h + k = 2n, \tag{5.1}$$

where n is an integer. We are additionally measuring following reflexes:

$$h + k \neq 2n. \tag{5.2}$$

The appearance of additional diffraction spots is indicated in Fig. 5.4 f) by dashed-line circles. However, the conditions:

$$(00l) : l = 2n \quad \text{and} \quad (0k0) : k = 2n \tag{5.3}$$

are still fulfilled and possible space groups are identified to be 94 ($P4_22_12$) and 114 ($P\bar{4}2_1c$). The difference in the space group has implications for the symmetry of the molecules. While the molecular symmetry of the structure measured for the PtTPP (space group 87) is described by a D4h point group and implies a planar geometry of the porphyrin macrocycle, both space groups coming in question for the H_2TPP crystals have different point groups (D_4 and D_{2d} respectively). These point groups have a reduced symmetry and may indicate ruffling of the molecules. Molecular ruffling described by the D_{2d} point group was also observed for the H_2TPP powder, where the molecules have crystallized in the tetragonal polymorph II[88](Fig. 5.2 c and Fig. 5.3 a).

In the crystallographic phases mentioned above the H_2TPP molecules obviously exhibit a four-fold inversion symmetry axis[88] (this is also valid for porphines in general[116]). At first sight this might be surprising, as only two out of four nitrogen atoms located diagonally opposite in the center of the porphine ring are bound to hydrogen atoms. These pyrrole rings are distinguishable from the other two and therefore the porphine core is determined by a two-fold rotational axis. The fact, that nevertheless a 4-fold molecular symmetry is experimentally observed, has been explained by a statistical distribution of the inner hydrogen atoms.[88] The reason for the statistical distribution was proposed to be either a static molecular disorder[116] or a dynamical effect caused by rapid intercoversion of N-H tautomers. Indication for the latter was given by NMR (Nuclear Magnetic Resonance) studies.[117]

High resolution TEM. The molecular orientation deduced from ED patterns is further corroborated by the HR-TEM image of the PtTPP thin film, corresponding to a two dimensional projection of the crystallites (Fig. 5.5). The contrast in the HR-TEM image showing a periodic modulation (Fig. 5.5 a) arises from the Z-contrast between the Pt cores and the organic macrocycle. The Fast Fourier Transform (FFT) in the inset shows two pairs of perpendicular directions (indicated by red and blue circles, respectively) along which a periodicity of 9.0 ± 0.5 Å is observed. Hence, the analysis of the HR-TEM image and the corresponding Fast Fourier Transform (FFT) in the inset yields two square lattices which are rotated by 36.71° in respect to each other. In the HR-TEM image these two differently oriented domains containing squared periodicities are labeled (I) and (II) and marked with blue and red dashed lines, respectively. The occurrence of two square lattices with a 9.0 ± 0.5 Å period and two different in-plane orientations at a relative angle of 36.71° is in accordance with the angle of 36° observed in the ED pattern of PtTPP (Fig. 5.4 b). The period of the lattice observed by HRTEM is in good accordance with the calculated lattice spacing of $d_{110} = 9.46$ Å for the tetragonal polymorph II. As PtTPP crystallizes in a body centered structure, the projection along the **c** axis, corresponding to a (001) contact plane as observed in ED pattern, yields an apparent square lattice with a period equal to d_{110}. The insets in Fig. 5.5 b and c depict the corresponding molecular packing of the Pt-TPP molecules in the tetragonal polymorph II along the **c**-axis projection. The dashed lines correspond to the (110) and (110) lattice planes, defining a grating with a periodicity of $d_{110} = 9.46$ Å as observed in the HR-TEM image. This result supports the body-centered structure of the Pt-TPP in epitaxied layers on KCl i.e. a structure isomorphous to the polymorph II evidenced in powders. This implies that epitaxy of Pt-TPP on KCl does not induce a specific thin film phase.

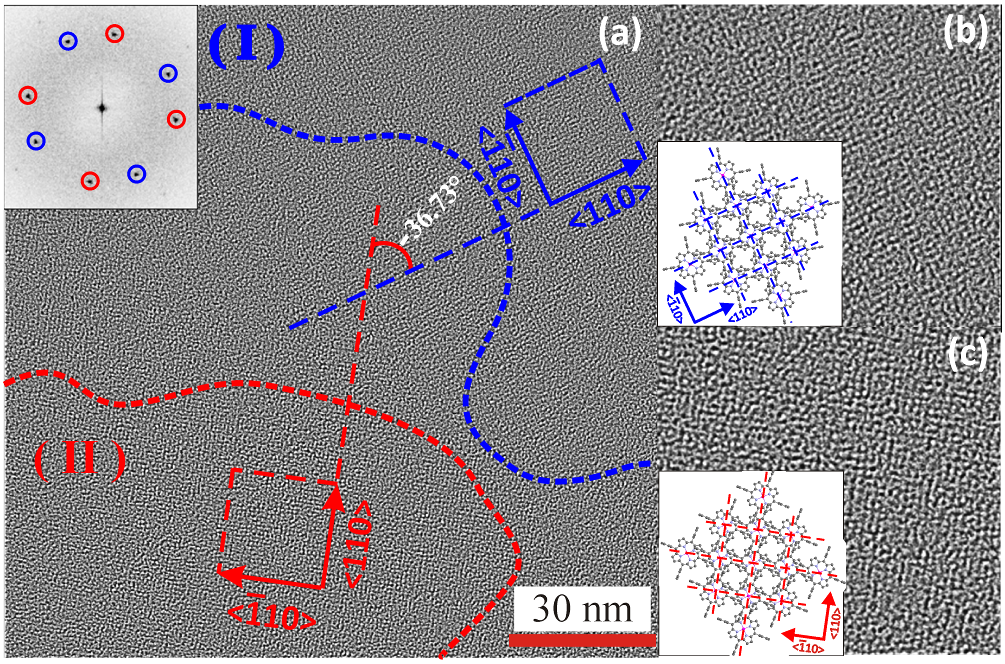

Figure 5.5: *(a) The high-resolution TEM image of PtTPP grown on KCl(100) substrate. The corresponding FFT image is shown in the inset. The blue and red colors indicate the different oriented domains: (I) and (II). The dotted lines represent the boundaries of oriented crystalline domains and the arrows indicate the crystallographic directions in the domains. The figure (b) and (c) are the enlarged HR-TEM images (38 nm x 38 nm) of the domains (I) and (II), respectively. The enlarged figures apparently display similar net-like morphology in both domains but in different orientations. The angle between 2 orientations is 36.7° as shown in (a) similar to XRD. The insets of (b) and (c) are models showing the molecular orientation of PtTPP networks in each domain.*

X-ray Diffraction

To determine the epitaxial alignment of the porphyrin molecules in respect to the KCl(100) substrate surface, XRD measurements were performed. The Bragg peak measured in the specular scan of the PtTPP thin film corresponds to a lattice spacing d = 0.484 nm and can be assigned to the (002) net plane of the tetragonal polymorph II (see Fig. 5.6 a). The orientation of the porphyrin crystallites with the (001) lattice plane parallel to the substrate as deduced from TEM measurement is confirmed. The rocking curve measured for this peak is rather narrow with a full width at half maximum of 0.641° indicating a small mosaicity of the crystallites composing the thin film. The pole figures measured for the lattice planes {101} with d = 0.787 nm (Fig. 5.6 b), {112} with d = 0.433 nm (Fig. 5.6 c) and {211} with d = 0.510 nm (Fig. 5.6 d) further reveal that the crystallites are also azimuthally well-ordered and are arranged in two domains. The mirror symmetry of the two domains along the high symmetry axes [010] and [001] of the KCl substrate indicates that the orientation of the crystallites is induced by molecule–substrate interactions.

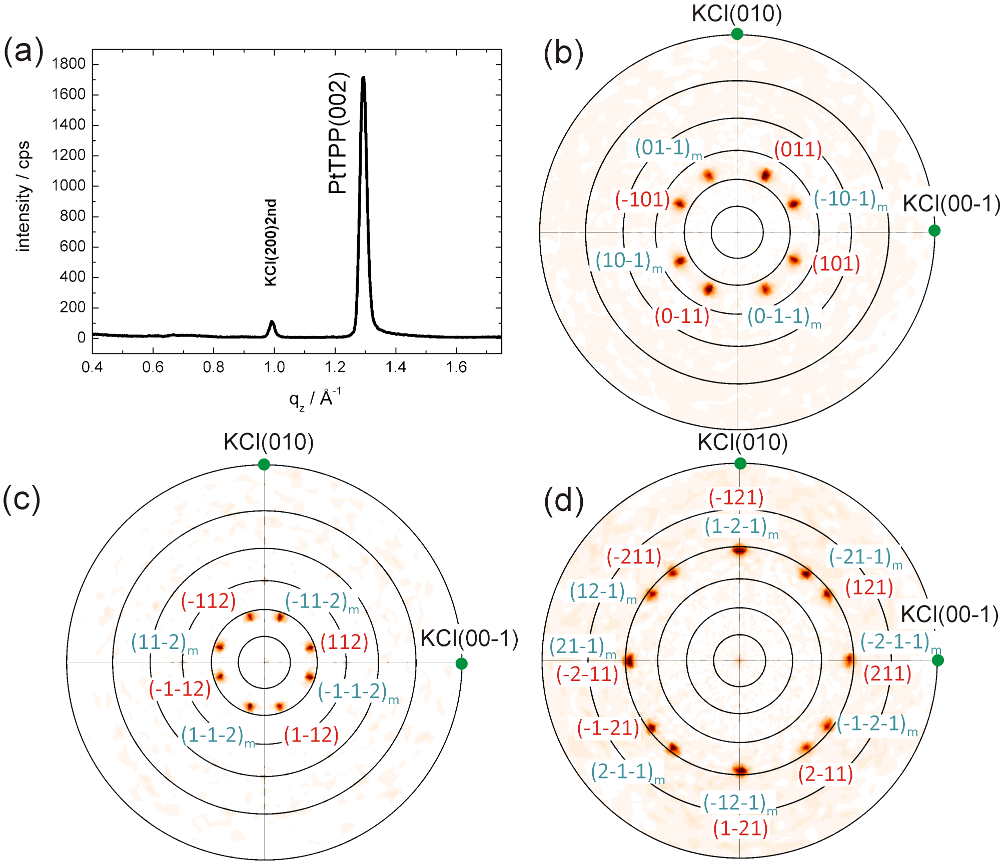

Figure 5.6: *(a) Specular scan of a 30 nm thick PtTPP film grown on KCl(100). Pole figures measured for net planes (b)* {101} *with d=0.787 nm, (c)* {112} *with d=0.433 nm and (d)* {211} *with d=0.510 nm reveal two epitaxially well-aligned domains, which are mirrored in respect to the substrate azimuths (denoted with indices in red and blue). The relative azimuthal orientation of the KCl(100) substrate is denoted by green circles.*

The epitaxial alignment of the molecules deduced from the pole figure measurements is depicted in Fig. 5.7 in the top view. The two molecular arrangements shown in (a) and (b), respectively, are indistinguishable as they would yield the same diffraction pattern in the pole figures. Thus, the pole figure diffraction patterns can be explained by either the configuration (a) (used for the indexation in Fig. 5.6 b-d) or (b) or a mixture of both. When the relative orientation of the molecules is neglected, both configurations exhibit an identical alignment of the unit cell in respect to the substrate surface. Interestingly, in the literature both molecular arrangements were reported for metalloporphyrins on KCl(100) substrates independently from each other.[118,119] However, in both cases the two unit cells of the mirrored domains yield diffraction patterns rotated by 36° to each other as also was observed in the TED patterns (Fig. 5.4) and HR-TEM image (Fig. 5.5 a).

Molecules lying in the (001) contact plane form a square unit cell with the cell parameter a = 1.345 nm. The dimensions of this unit cell are in accor-

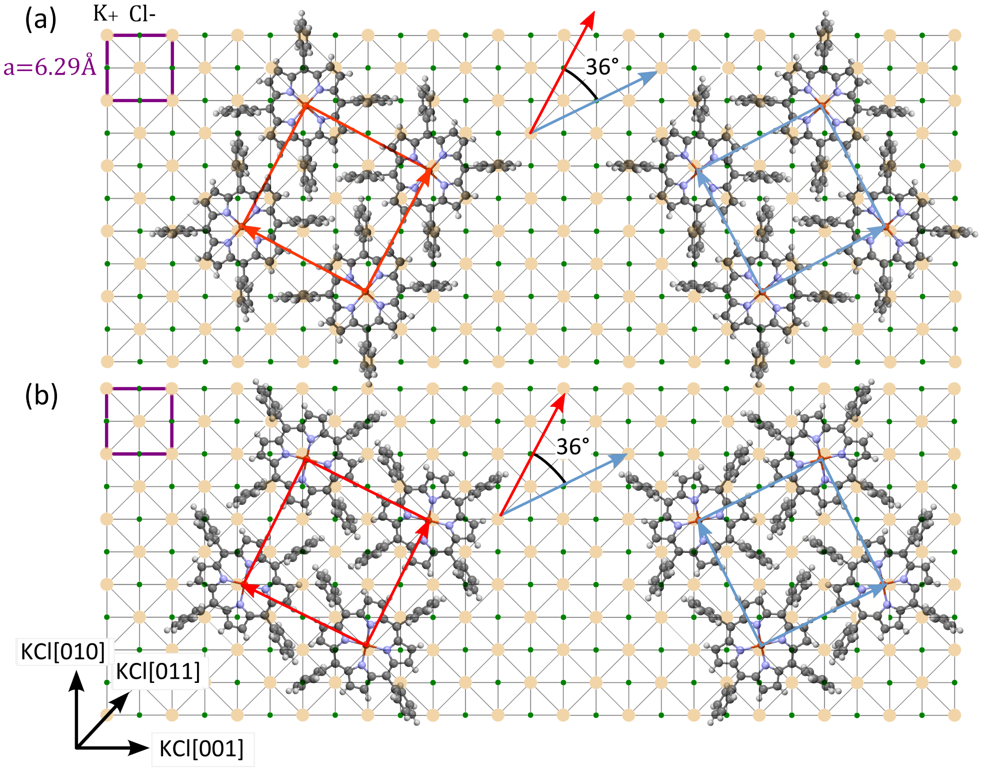

Figure 5.7: *Epitaxial alignment of PtTPP domains on the KCl(100) surface substrate in top-view. PtTPP crystallites are oriented with the (001) net plane parallel to the substrate surface and form a commensurate square unit cell with a = 13.375 Å. Lattices of the two molecular arrangements shown in (a) and (b) are indistinguishable as they yield the same diffraction pattern in the pole figures.*

dance with the usually reported monolayer structure for systems of porphyrin molecules[96,98,104] suggesting that the alignment of the monolayer molecules basically is preserved when films in multilayer range are grown. When a lattice mismatch of 5% is taken into account, the epitaxial relationship with the underlying KCl(100) substrate can be described by the following commensurable epitaxial matrix

$$M_1 = \begin{pmatrix} 2 & 1 \\ -1 & 2 \end{pmatrix} \tag{5.4}$$

where $\mathbf{a}_{KCl} = (0.629, 0)$ and $\mathbf{b}_{KCl} = (0, 0.629)$ are the vectors of the non-primitive KCl(100) unit cell. The KCl(100) 2d unit cell vectors are given in a basis spanned by unit vectors running along the [001] and [010] directions, respectively. This means, the observed relative orientation of the 2D square unit cell ensures that a commensurable structure with the underlying substrate is formed. The software Epicalc[120] based on geometric lattice misfit modeling calculates exactly the same azimuthal orientation as the most favorable for this 2D unit cell. This underlines that the minimization of the lattice mismatch is a driving force for the observed epitaxial alignment in this system.

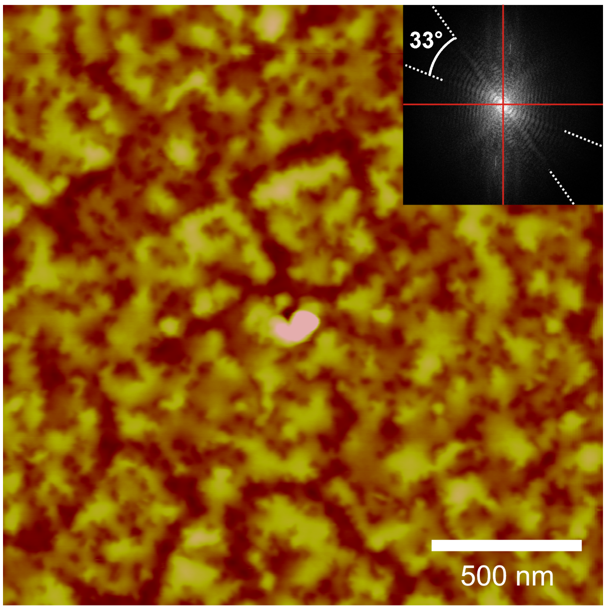

Figure 5.8: *AFM image of a 30 nm PtTPP film grown on KCl(100). The inset shows the Fourier transform of the image. The dashed white lines denote the preferential alignment of the PtTPP crystallites in respect to the substrate azimuths (solid red lines).*

An AFM image recorded on the 30 nm thick PtTPP film grown on KCl(100) is shown in Fig. 5.8. The morphology shows preferred alignment of the features, which is reflected in the Fourier transform in the inset. The relative azimuthal alignment of the crystallites (dashed white lines) in respect to the substrate (horizontal/vertical lines) enclosing an angle of $(33 \pm 4)^\circ$ is in good accordance with the alignment of the 2D unit cells deduced from XRD measurements.

5.3.3 Structure and Alignment of Tetraphenyl-Porphyrins on Cu(110)-(2x1)O

Low Energy Electron Diffraction

LEED measurements observed for H_2TPP and PtTPP monolayer films on Cu(110)-(2x1)O surfaces are shown in Fig. 5.9 a and b respectively. Both films exhibit the same diffraction pattern consisting of sharp diffraction spots which indicate a highly ordered structure consisting of two mirrored domains. In the corresponding simulation (Fig.5.9 c) the two domains are depicted as blue and red dots, whereas the black circles correspond to the measured diffraction spots. The evaluation of the diffraction pattern, however, reveals a peculiar 2D structure clearly different from that observed in the films deposited on KCl(100). On the oxygen reconstructed Cu(110) surface the molecules are arranged in a rather dilute unit cell with $a = (1.51 \pm 0.05)$ nm, $b = (2.57 \pm 0.05)$ nm and $\gamma = 78.61$. This structure can be described by the following epitaxial matrix where $\mathbf{a} = (0.3607,\ 0)$ and $\mathbf{b} = (0,\ 0.5102)$ are the vectors of the rectangular unit cell formed on Cu(110) by oxygen reconstruction defined in a basis spanned

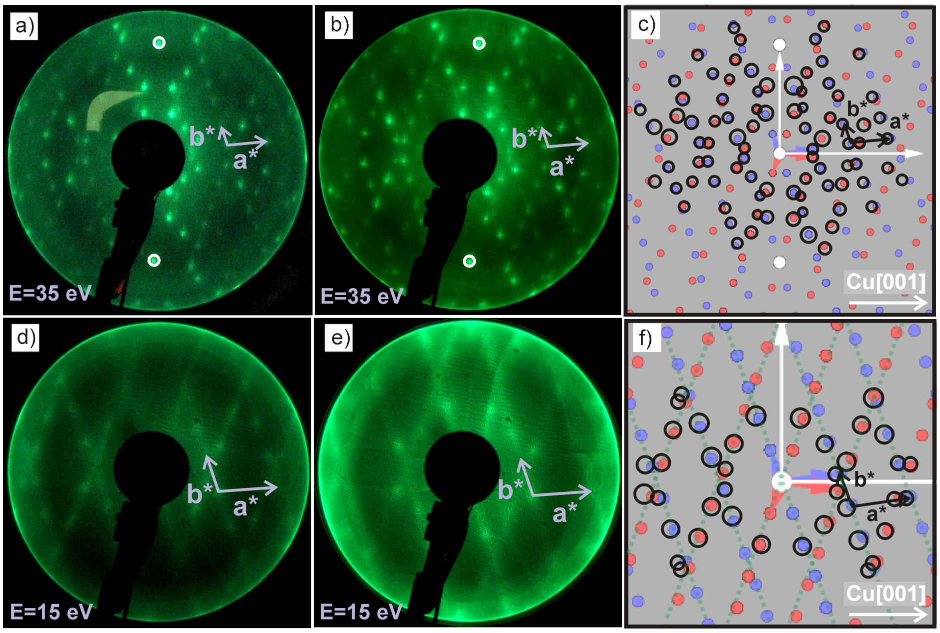

Figure 5.9: *LEED images of* H_2TPP *and PtTPP monolayers grown on Cu(110)-(2x1)O are shown in (a) and (b), respectively, and reveal the same diffraction pattern. (c) The measured diffraction patterns (black circles) can be explained by two mirrored domains (red and blue spots) forming a unit cell with dimensions:* $a = (1.53 \pm 0.05)$ *nm,* $b = (2.57 \pm 0.05)$ *nm and* $\gamma = 78.57°$*. The corresponding LEED measurements of the 3 nm multilayer films are shown in (d) for* H_2TPP *and (e) for PtTPP. The pattern shown in (f) is calculated using basically the same unit cell as observed for the monolayer.*

by unit vectors running along the [001] and [-110] directions, respectively:

$$M_1 = \begin{pmatrix} 4 & -1 \\ 1 & 5 \end{pmatrix} \tag{5.5}$$

As all elements of the matrix are integers the PtTPP monolayer structure is commensurate with the rectangular unit cell of the oxygen reconstructed copper surface. The LEED measurements performed on the 3 nm thick H_2TPP (Fig. 5.9 d) and PtTPP (Fig. 5.9 e) multilayer films indicate that the molecular arrangement observed in the monolayer regime is preserved. The simulated pattern (Fig. 5.9 f) showing a nice correspondence with the measured diffraction patterns (black circles) reveals basically the same unit cell parameters: $a = (1.46 \pm 0.05)$ nm, $b = (2.59 \pm 0.05)$ nm, $\gamma = 78.61°$.

X-ray Diffraction

In a next step, the crystallographic properties of a 37 nm thick multilayer film were investigated by XRD. Specular scan measured to determine the net planes oriented parallel to the substrate surface did not reveal any diffraction intensity stemming from the organic film and thus is not depicted here. Nevertheless, the pole figures summarized in Fig. 5.10 are measured for (a) d = 1.213 nm, (b)

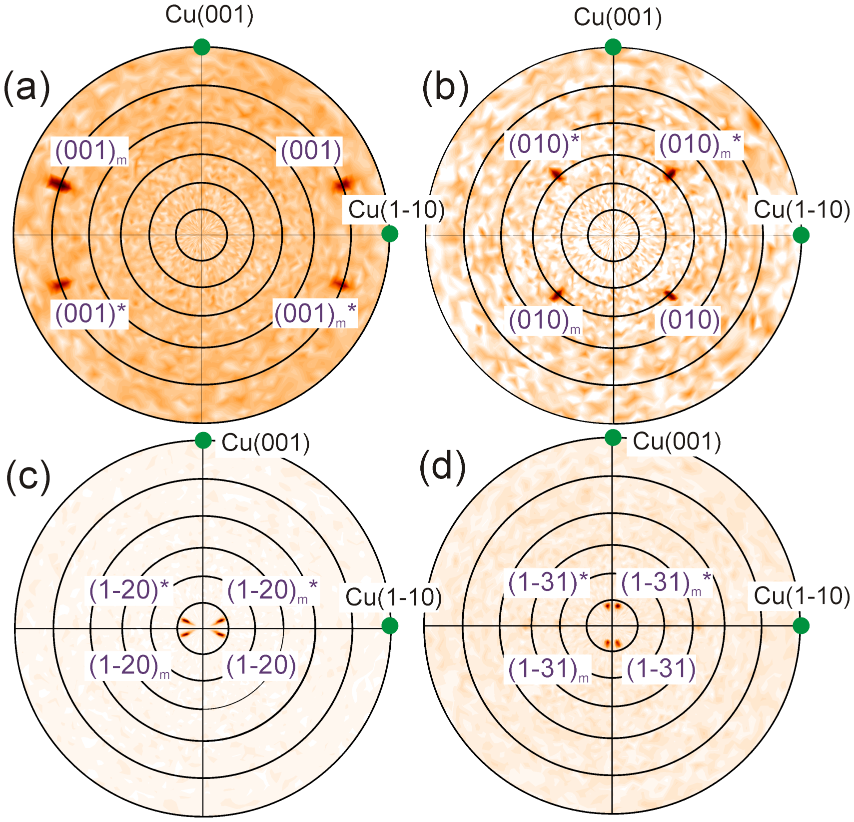

Figure 5.10: *Pole figures of the H2TPP multilayer film grown on the Cu(110)- p(2x1) substrate are measured at different* d_{hkl} *values: (a)* d_{001}*=12.13 Å , (b)* d_{010}*=10.12 Å , (c)* $d_{1\bar{2}0}$*=4.41 Å,(d)* $d_{1\bar{3}1}$*=3.19 Å. Pole figures reveal that crystallites arrange in epitaxially oriented domains with the* $(5\overline{10}3)$ *net plane parallel to the substrate surface. The relative azimuthal orientation of the KCl(100) substrate is denoted by green circles.*

d = 1.012 nm, (c) d = 0.441 nm, (d) d = 0.319 nm and indicate well-ordered domains. These domains are epitaxially aligned as they show mirrored symmetry along the substrate azimuths. However, when compared with the pole figures measured on the KCl(100) substrate (see Fig. 5.6 b-d), the distribution of the enhanced pole densities (EPD) indicates a lower symmetry of the crystal structure.

A detailed analysis reveals that the molecules have crystallized in a known triclinic phase with the following cell parameters: a = 6.44 Å, b =10.42 Å , c = 12.41 Å, a = 96.06°, b = 99.141°, γ = 101.121° For this polymorph the porphyrin molecules are stacked along the a-direction. The macrocycle is tilted by approximately 64° in respect to the (b,c)-plane and the neighboring porphyrin macrocycles do not lie in the same plane (see Fig. 5.11 a). In porphyrin thin films it is usually observed that molecules stack with their macrocycles parallel to the substrate surface forming columnar structures as was observed for porphyrins grown on KCl(100). Since this triclinic polymorph does not reveal a lattice plane of densely packed molecules it is considered unlikely to appear in thin films.[121]

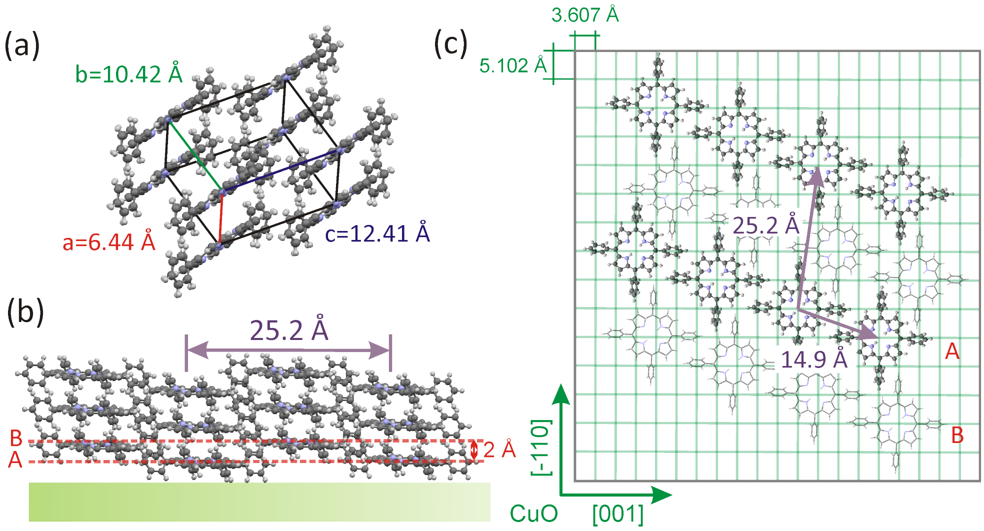

Figure 5.11: *(a) Unit cell of the triclinic polymorph observed in a 37 nm thick* H_2TPP *film grown on a Cu(110)-(2x1)O surface. (b) Side view of* H_2TPP *molecules orienting with the* $(5\bar{1}\bar{0}3)$ *net plane parallel to the Cu(110)-(2x1)O substrate. (c) Alignment of* H_2TPP *molecules on the oxygen reconstructed Cu(110) surface in top view.*

From the pole figure measurements, the orientation of the porphyrin crystallites can be described by the high indexed $(5\bar{1}\bar{0}3)$ lattice plane being parallel to the substrate. The structure factor for this lattice plane equals zero, explaining the absence of diffraction intensity stemming from the thin film in the specular scan. The side view of the molecules oriented with the $(5\bar{1}\bar{0}3)$ lattice plane parallel to the surface (Fig. 5.10 b) illustrates that also in this system H_2TPP molecules have adopted an orientation where the porphyrin rings are nearly parallel to the substrate with a tilt of only 91 in respect to it. Figure 5.11 c shows the arrangement of the molecules on the oxygen reconstructed Cu substrate in top view. The $[\bar{7}32]$ direction of the H_2TPP crystallites is determined to be parallel to the [001] direction of the oxygen reconstructed copper surface; this means that H_2TPP molecules align epitaxially with diametrically opposite phenyl rings along the oxygen rows of the CuO surface reconstruction (see Fig. 5.11 c). The commensurate unit cell deduced from the monolayer LEED measurements and described by the epitaxial matrix M_2 is very close to the 2D unit cell deduced from the molecules lying in the $(5\bar{1}\bar{0}3)$ net plane with only a 5 % mismatch. Further, in Fig. 5.11 c it is seen that the packing of the molecules is not as dilute as expected from the unit cell dimensions deduced from the LEED measurements. At a distance of only 0.2 nm there is a second plane B containing porphyrin molecules which have the same molecular orientation with respect to the substrate. The molecules in this plane form an identical commensurate unit cell but with an origin shifted by a vector of $\mathbf{s}$ = (3,2) (i.e. $3\mathbf{a}_{\mathrm{Cu}}$, $2\mathbf{b}_{\mathrm{Cu}}$) with respect to the unit cell lying in plane A. Taking this second plane into account, the coverage of the porphyrin molecules is rather dense. In the side-view (see Fig. 5.11 b) the position of these two planes is indicated.

The surface morphology of the same H_2TPP multilayer film (37 nm) was

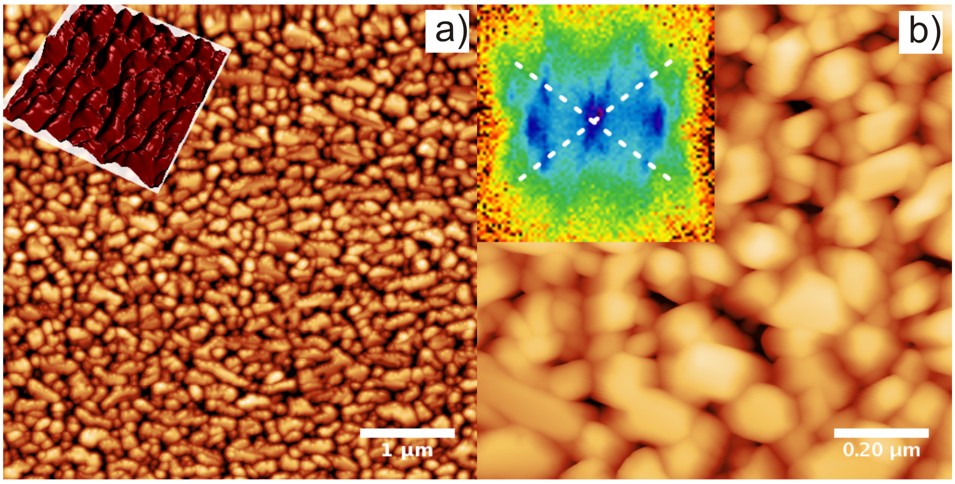

Figure 5.12: *AFM images of a 37 nm thick* H_2TPP *film grown on Cu(110)-(2x1)O. (a) Crystallites with a size of 0.013 mm*^{2} *and an average aspect ratio of 1:1.4 are observed (z-scale 50 nm). The inset is a 3D representation of 1 mm detail which clearly demonstrates that the crystals are aligned. (b) 1 mm detail of the* H_2TPP *film showing faceted crystallites. The inset displays the slope distribution (x,y range from -1 to 1 or -45° to 45°) found in the image. Facets with an inclination angle of 29°± 5° are most common (dashed lines). The two dominant azimuthal directions of the facet normals are separated by 76° ± 8°.*

characterized using AFM. The 5x5 mm^2 AFM image shown in Fig. 5.12 a reveals a rather uniform, granular morphology which is reminiscent of that observed for porphyrins on the KCl(100) surface (compare Fig. 5.4 a and d). The crystallites have an average aspect ratio of 1:1.4 and a projected area of 0.013 mm^2 (130 nm x 90 nm). On a smaller scale (inset in Fig. 5.12 a) it becomes evident that crystallites line up forming linear structures with a correlation length of up to 500 nm. Figure 5.12 b shows a 1x1 mm^2 detail of the surface. The crystals exhibit a limited number of well oriented facets. Since the AFM topography image represents the three-dimensional morphology z(x,y), it can be analyzed in terms of the orientation of the local surface normals finally yielding integral information on the facet orientations.[122,123] The corresponding slope distribution, obtained by fitting a local plane through the neighborhood of each point and using its gradient, is given in the inset of Fig. 5.12 b. The distance of a point to the center corresponds to the inclination of the local plane while the polar position represents the in-plane orientation of the local surface normal. It shows that the most frequent facets normals found have an inclination angle of 29° ±5° (measured from the substrate surface normal) and are separated azimuthally 76° ± 8° (dashed lines). These inclination angles fit with the angles enclosed by the low-indexed planes like $(1\bar{1}0)$ (24.2°) and $(1\bar{1}1)$ (27.9°) with the $(5\bar{10}3)$ lattice plane, which is parallel to the substrate surface. The azimuthal orientation of the crystallites corresponds well to the two mirrored domains which are rotated by 40° to each other as determined by XRD.

5.4 Discussion

The crystal structures measured in porphyrin powders are used as a starting point to discuss the impact of the substrate surface on the polymorphic phase appearing in porphyrin thin films. In powder, H_2TPP and PtTPP crystallize in two different tetragonal polymorphs. The tetragonal polymorph I (a=b= 15.2215 Å, c = 13.97 Å) with a ruffled macrocycle was found for the H_2TPP powder, while in the PtTPP powder the tetragonal polymorph II (a = b = 13.345 Å, c = 9.719 Å) with a flat macrocycle was observed.
We have found that in thin films, molecules of tetraphenylporphyrins adopt different polymorphic structures depending on the nature of the substrate surfaces (schematically summarized in Fig. 5.13). When deposited on KCl(100) substrates both porphyrin molecules (H_2TPPand PtTPP) crystallize in the tetragonal polymorph II with their macrocycles oriented parallel to the substrate surface. The relative azimuthal orientation of the formed 2D unit cell is commensurable with the 2D unit cell of the KCl(100) substrate. The software Epicalc43 based on geometric lattice misfit modeling calculates exactly the same azimuthal orientation as the most favorable for this 2D unit cell. This underlines that the minimization of the lattice mismatch is a driving force for the observed epitaxial alignment in this system. By contrast, for molecules lying in the (001) lattice plane of the tetragonal polymorph I (corresponding to macrocycles oriented parallel to the substrate) no commensurable arrangement is possible, making this polymorphic phase less favorable to be formed on the KCl(100) substrate.

On the Cu(110)-(2x1)O surface the porphyrin macrocycles are oriented nearly parallel to the substrate surface and crystallize in a triclinic polymorphic phase, a polymorph not observed in the powders. Using the geometric lattice matching routine Epicalc the azimuthal orientation of the 2D unit cell forming a commensurable structure as observed by LEED and pole figure measurements is predicted to be the most favorable. If we take the 2D unit cell of the tetragonal polymorph II observed on the KCl(100) substrate into account and calculate the most favorable epitaxial alignment on the Cu(110)-(2x1)O surface, no commensurate structure is found. This gives a possible explanation why on the oxygen reconstructed Cu(110) surface the triclinic phase is more favorable than the tetragonal polymorph II.

The open question that remains is why on the Cu(110)- (2x1)O surface the porphyrin molecules do not crystallize in the tetragonal polymorphic phase I. The (001) net plane of this structure contains the macrocycles and for the square unit cell formed by the molecules lying in this plane (a=b=1.5125 nm) azimuthal orientation yielding a commensurate unit cell would be possible. We suggest that it is the conformation of porphyrin molecules in the tetragonal phase I which makes this polymorph less favorable for the accommodation on the strongly corrugated Cu(110)-(2x1)O surface. In the triclinic structure the phenyl rings are not perpendicular to the macrocycle, as also was evidenced by NEXAFS studies of these films,[82] but enclose an angle of approx. 62° with it.

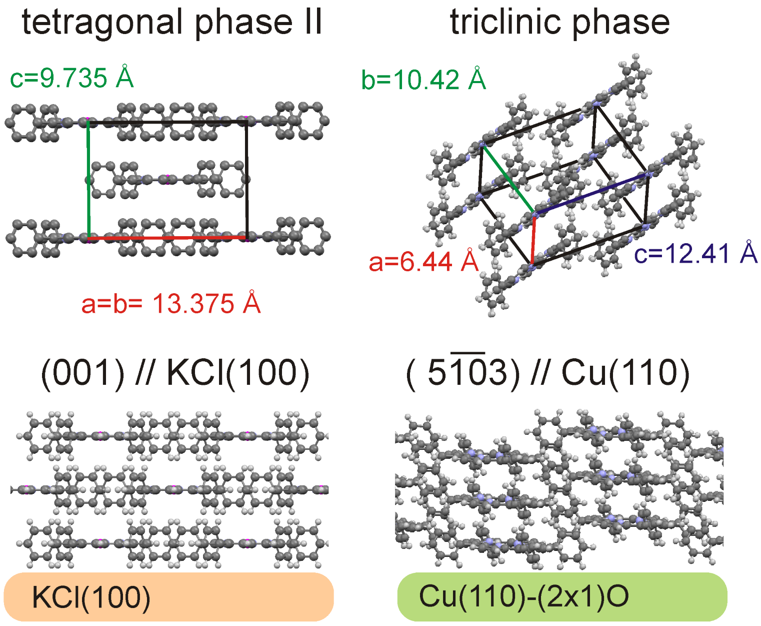

Figure 5.13: *Schematic diagram summarizing the polymorphic phases and preferential orientations of tetraphenyl-porphyrin thin films deposited on KCl(100) and Cu(110)-(2x1)O substrates, respectively. The relative orientation of the molecules in respect to the selected substrate surface is depicted in the bottom row. The top row shows the polymorphic phases appearing on respective substrate surfaces.*

This finding is in accordance with studies reporting a bending of phenyl rings when porphyrins are deposited on metallic surfaces.[100] However, in the triclinic structure the opposed phenyl rings lie in the same plane, whereas in the case of the tetragonal phase I their planes are twisted by an angle of approximately 23°. As the corrugation of the Cu(110)-(2x1)O surface induces an epitaxial alignment of molecules parallel to the oxygen rows (e.g. along the corrugation trenches) the triclinic phase with the untwisted opposed phenyls might be more favorable to arrange itself to the surface corrugation than the tetragonal phase. Taking this finding into account, we suggest that also in the case of porphyrin molecules deposited on the KCl(100) substrate, the phenyl rings will preferentially align along the principle symmetry axes of the substrate making the alignment depicted in Fig. 5.7(a) more reasonable than that in 5.7(b).

5.5 Conclusions

This work shows the high structural adaptability of porphyrin molecules leading to an extraordinarily pronounced polymorphism with the substrate determining not only the crystallite orientation but also the polymorph that grows on it. In particular, we have investigated the structural and morphological properties of well-ordered and epitaxially aligned porphyrin thin films deposited on two different substrates. On the Cu(110)-(2x1)O surface the porphyrins crystallize in a rather unusual triclinic phase for thin films with macrocycles nearly parallel to the substrate. In contrast, on the KCl(100) substrate we observe the tetragonal polymorph II exhibiting the (001) contact plane containing the flat lying macrocycles. In all cases, the porphyrin molecules form a commensurate unit cell with the respective substrate ensuring the most effective geometric lattice matching. Based on these results two main driving forces for the epitaxial growth of porphyrins on the observed anisotropic surfaces are identified: (i) alignment of macrocycles parallel to the substrate surface forming molecular columns in a subsequent step of crystallization and (ii) minimization of the lattice mismatch between the adsorbate and the substrate unit cell. These two requirements determine which polymorphic phase is most likely realized on a given substrate surface.

Chapter 6

Epitaxially grown films of standing and lying pentacene molecules on Cu(110) surfaces

The work presented in this chapter was published in the journal *Crystal Growth & Design* and is essentially identical to the article. Figure 6.1 shows the title of the article and contributing authors with their affiliations. *Reproduced with permission from Crystal Growth&Design. Copyright 2011 American Chemical Society. The original article is available online at the following link:* http://pubs.acs.org/doi/pdf/10.1021/cg101230j.

Abstract. Here, it is shown that pentacene thin films (30 nm) with distinctively different crystallographic structures and molecular orientations can be grown under essentially identical growth conditions in UHV on clean Cu(110) surfaces. By X-ray diffraction, we show that the epitaxially oriented pentacene films crystallize either in the "thin film" phase with standing molecules or in the "single crystal" structure with molecules lying with their long axes parallel to the substrate. The morphology of the samples observed by atomic force microscopy shows an epitaxial alignment of pentacene crystallites, which corroborates the molecular orientation observed by X-ray diffraction pole figures. Low energy electron diffraction measurements reveal that these dissimilar growth behaviors are induced by subtle differences in the monolayer structures formed by slightly different preparation procedures.

6.1 Introduction

Because of its high charge carrier mobility[124,125] and its ability to form well-ordered films,[126,127] pentacene ($C_{22}H_{14}$), a highly conjugated oligoacene consisting of five benzene rings, has become the material of choice for the active layer in organic thin film transistors. Although pentacene (5A) is already used in commercially available semiconductors, many aspects of its thin film growth are still unclear. Especially, it is remarkable that when deposited in thin films,pentacene crystallizes in various polymorphic phases and molecular orientations. As the

CRYSTAL GROWTH & DESIGN

dx.doi.org/10.1021/cg101230j | *Cryst. Growth Des.* 2011, 11, 1015–1020 ARTICLE

pubs.acs.org/crystal

Epitaxially Grown Films of Standing and Lying Pentacene Molecules on Cu(110) Surfaces

Tatjana Djuric,[*,†] Thomas Ules,[‡] Heinz-Georg Flesch,[†] Harald Plank,[§] Quan Shen,[∥] Christian Teichert,[∥] Roland Resel,[†] and Michael G. Ramsey[‡]

[†]Institute of Solid States Physics, Graz University of Technology, 8010 Graz, Austria
[‡]Institute of Physics, Karl-Franzens University, 8010 Graz, Austria
[§]Institute for Electron Microscopy, Graz University of Technology, 8010 Graz, Austria
[∥]Institute of Physics, Montanuniversität Leoben, 8700 Leoben, Austria

Figure 6.1: *Header of the article published in the journal Crystal Growth & Design. It shows all contributing authors and the corresponding affiliations.*

crystalline phase and the molecular orientation of the pentacene thin films have a great impact on their electronic properties, understanding the parameters controlling the film structure is important for the development of reliable and reproducible film growth procedures.

To gain a systematical overview of the numerous pentacene (5A) polymorphs reported,[37–44] preferentially, the interplanar spacing of the (001) planes $d_{(001)}$ is used for distinction. The reported bulk phase structures basically can be classified in two different polymorphs: the “bulk” phase with $d_{(001)} \sim 1.45$ nm[37,40] and the “single crystal” phase with $d_{(001)} \sim 1.41$ nm.[38,40,44] Additionally, thermally evaporated pentacene thin films often exhibit a so-called “thin film” phase with $d_{(001)} \sim 1.54$ nm.[41–43]

Many reasons have been proposed as to why and under which circumstances a specific polymorphic phase and molecular orientation are formed. So far, the substrate material and temperature, the deposition rate, and the final thickness were reported to have a great influence on the crystallographic structure of the pentacene films.[128–132] Especially for the growth of the first monolayer, pentacene molecules tend to grow in an upright orientation when deposited on flat, inert substrates like on SiO_2 or on polymeric dielectrics.[127–129,133–136] On reactive surfaces like on clean Si or clean metals, pentacene thin films exhibit an arrangement of flat-lying molecules.[129,137,138] It has been reported that on SiO_2 the substrate temperature and the deposition rate are the parameters determining which polymorphic phase will appear. The “single crystal” phase is favored for high substrate temperatures and low deposition rates. The thin film phase, on the other hand, preferentially grows at low substrate temperatures and high deposition rates.[128] The final thickness of the film was also observed to have an influence on the polymorphic phase: The “thin film” phase dominates at average film thicknesses smaller 50 nm, and above 150 nm, the “single crystal” phase is prevalent.[131] In contrast here with experiments on an atomically clean and controlled Cu(110) substrate surface, we will show that leaving all of the growth parameters constant (substrate, substrate temperature, deposition rate, and film thickness), the different crystallographic structure and the orientation of the films are determined solely by the structure of the first monolayer.

A variety of lying 5A monolayer structures on Cu(110) can be found in the literature;[94,132,139–142] however, beyond the monolayer, only multilayers with uprightmolecular orientations have, until now, been reported.[132,139] From surface energy considerations alone, this might be expected as the (001) lattice plane (corresponding to upright standing molecules) has a significantly lower energy.[143] However, our previous ultraviolet photoelectron spectroscopy (UPS) studies of 5A film growth on clean Cu(110) have shown that in fact two distinctly different multilayer films with different valence band photoemission signatures and distinct angle-resolved photoemission behavior suggesting films of either upright or lying molecular orientation could be formed.[144,145]

In this work, we investigate the structure of pentacene thin films grown under identical conditions on subtly different monolayers on clean Cu(110) surfaces. The resulting multilayer films are shown to exhibit either the "thin film" phase with standing molecules or the "single crystal" phase with molecules lying with their long molecular axes parallel to the substrate. By studying the evolution of the film structure from the mono- to the multilayer regime, we illuminate the underlying mechanism determining the crystallographic phase and the molecular orientation of the prepared thin films.

6.2 Experimental Section

6.2.1 Sample preparation

The Cu(110) substrate surface was prepared by cleaning the copper crystal by repeated cycles of Ar^+-ion bombardment and annealing to 800 K in a UHV system with a base pressure of 10^{-10} mbar. The pentacene (purchased from Fluka) was deposited in situ from a thoroughly degassed evaporator with a pressure $< 10^{-9}$ mbar during the evaporation. The film growth in different stages was monitored in situ by low energy electron diffraction (LEED) and ARUPS measurements. LEED experiments were performed with an Omicron MCP-LEED. Here, a microchannel plate is used to amplify electrons being backscattered by the sample. Because of this amplification, only a low incident beam current in the nA range is needed. Thus, no beam damage or charging problems were encountered even for the relatively thick molecular films.

Generally, when pentacene films are grown directly on the Cu(110) substrate, valence band photoemission and LEED imply that multilayers of upright standing molecules are formed, while, if such multilayers are thermally adsorbed and then a fresh multilayer is grown, it consists of lying molecules. To identify the reason for this different growth behavior, two routes using identical substrate temperatures and deposition rates but resulting in films of either standing or lying molecules were developed. The specific preparation for the upright film (see Fig. 6.2 a) characterized here was evaporation of an initial

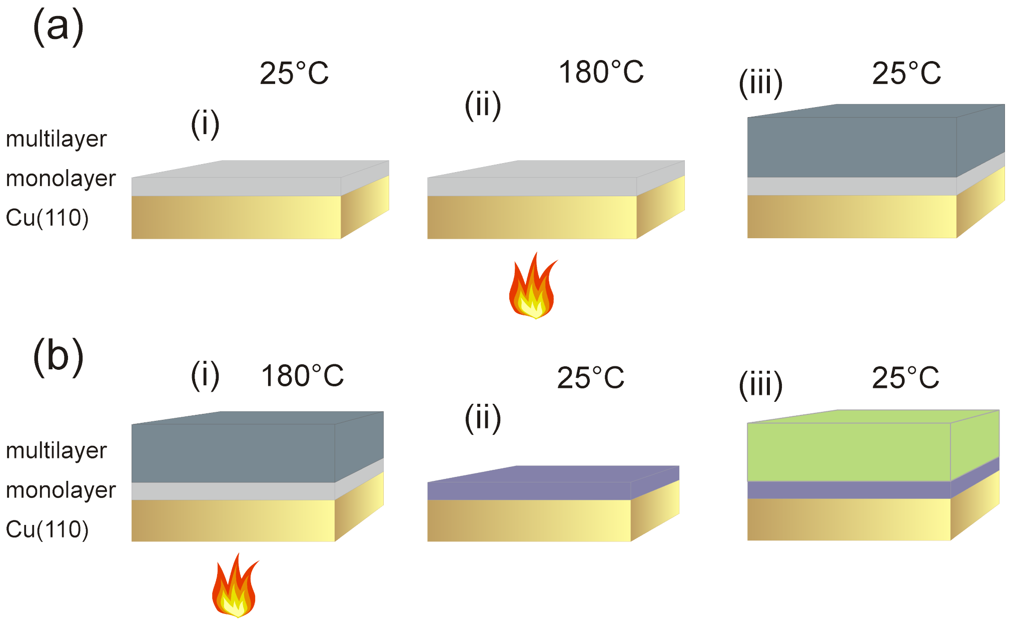

Figure 6.2: *a) Preparation steps of a pentacene thin film grown on monolayer 1. b) Preparation steps for the film grown on monolayer 2.*

monolayer (4 Å, as monitored by a quartz microbalance assuming a 5A density of 1.33 g cm^{-3}) at room temperature followed by annealing to 180 °C. After cooling down to room temperature on this monolayer (henceforth denoted as monolayer 1), a multilayer was grown at a deposition rate of 5 Å/min to a final thickness of 300 Å. The preparation of a lying film is shown in Fig. 6.2. First, an upright multilayer film (prepared as above) is desorbed by annealing it to 180 °C. This leaves a monolayer (denoted as monolayer 2) on which again 300 Å of 5A, at a rate of 5 Å/min, was deposited at room temperature. Note that in both cases the monolayers have been annealed to the same temperature.

6.2.2 X-ray diffraction measurements

The in situ prepared and characterized films were removed from the UHV chamber for the X-ray diffraction (XRD) measurements including specular scans and pole figure measurements. Specular scans determine lattice planes of the thin film oriented parallel to the substrate by varying the magnitude of the scattering vector in z-direction (perpendicular to the substrate surface). The pole figures are measured by keeping the magnitude of the scattering vector constant while systematically changing its direction. Thereby, the distribution of lattice plane orientations is obtained, which yields the azimuthal orientation of the pentacene crystallites with respect to the Cu(110) substrate. Specular scans and pole figures were measured with a Philips X'pert X-ray diffractometer using Cr Kα radiation and a secondary side graphite monochromator. The simulation of pole figures was performed with Stereopole,[108] and for the evaluation of the specular scans, Powder Cell[109] was used.

6.2.3 Atomic force measurements

Atomic force microscopy (AFM) measurements of the multilayer film grown on the "as-prepared" monolayer 1 were performed with a Dimension3100 microscope equipped with a Hybrid closed loop scan head and a Nanoscope IVa controller (Digital Instruments, VEECO). All measurements were done in TappingMode^{TM} with different Olympus cantilever (2-40 N/m) depending on the sample requirements.

The AFM measurements of the multilayer film prepared on the monolayer 2 were performed by Asylum Research MFP-3D^{TM} AFM in tapping mode, which can eliminate lateral forces between tip and surface to avoid damage to the sample. For this intermittent contact mode, conventional Si-probes (Pointprobe®plus PPP-NCHR probe) were used with a resonance frequency of 300 kHz and a force constant of $40 Nm^{-1}$. The tip is typically 10-15 μm high and the tip radius is smaller than 10 nm.

6.3 Results

6.3.1 Upright Pentacene Films

XRD measurements of a pentacene thin film on Cu(110), where the multilayer was prepared on the monolayer 1, are shown in Fig. 6.3. The specular scan (Fig. 6.3 a) reveals that the pentacene film crystallizes in a so-called "thin film" phase ($5A_t$) with the crystallites oriented with the $5A_t(001)$ lattice plane parallel to the Cu(110) substrate surface. The unit cell parameters as reported by Nabok et al.,[43] a = 0.592 nm, b = 0.754 nm, c = 1.563 nm, α= 81.5°, β= 87.2°, and γ= 89.9°, imply that the long molecular axes of the molecules are tilted 3° from the surface normal.

Pole figure measurements at q= 1.337 $Å^{-1}$ (Fig. 6.3 b), q= 1.664 $Å^{-1}$ (Fig. 6.3 c), and q= 1.989 $Å^{-1}$ (Fig. 6.3 d) corroborate this orientation and furthermore indicate epitaxially well-ordered domains. In the pole figure measured at q = 1.989 $Å^{-1}$ (Fig. 6.3 d), poles of four different net planes are detected as their q values lie close to each other: (121) q = 1.976 $Å^{-1}$, $(1\bar{2}0)$ q=1.9861 $Å^{-1}$, $(\bar{1}21)$ q = 1.987 $Å^{-1}$, and (120) q = 1.996 $Å^{-1}$. The pole figure seen in Fig. 6.3 b (q = 1.337 $Å^{-1}$) shows poles of two different net planes having similar q values: $(1\bar{1}0)$ q = 1.351 $Å^{-1}$ and (110) q = 1.359 $Å^{-1}$. This measurement allows the conclusion that the 5A crystallites are arranged in two domains, which are rotated by 180° to each other, as the two enhanced pole densities (EPDs) belonging to the $(1\bar{1}0)$ are higher than those of the (110) plane as theoretically expected. In the case of four equivalent domains, including the mirrored ones, the four EPDs would have a similar magnitude.

The azimuthal orientation deduced from the pole figures shows that the pentacene crystallites are aligned with the [031]* crystallographic direction parallel

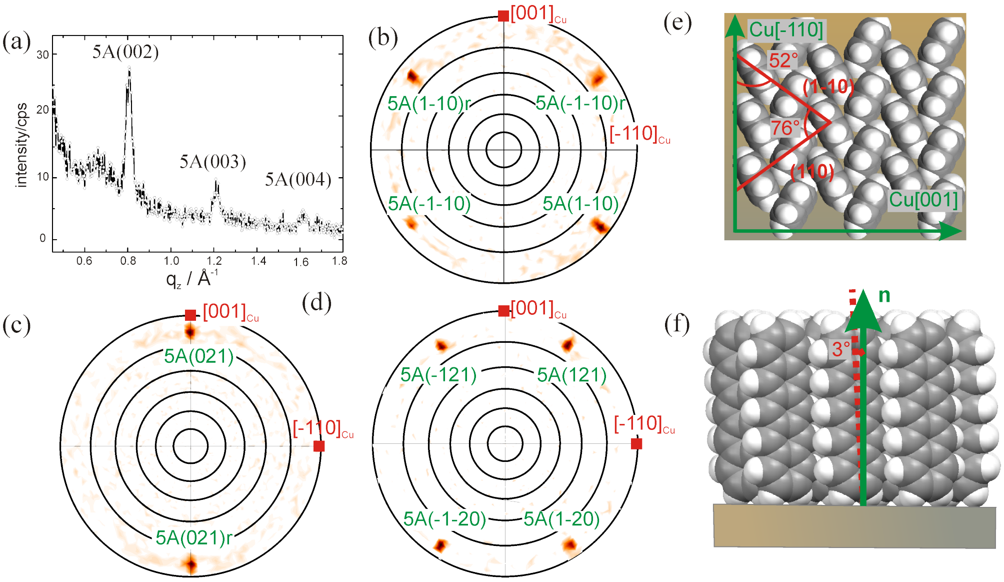

Figure 6.3: *XRD measurements of a pentacene thin film grown on Cu(110) surface. The multilayer film was deposited on the monolayer 2. (a)The specular scan shows that pentacene crystallizes in a "single crystal phase" with the (022) net plane parallel to the Cu(110) substrate surface. Pole figures measured at (b)* $q_z = 0.89$ *Å*$^{-1}$*, (c)* $q_z = 1.36$ *Å*$^{-1}$*, and (d)* $q_z = 1.99$ *Å*$^{-1}$ *reveal well-ordered, epitaxially aligned domains. The top view of this molecular orientation is shown in panel e, and the side view is shown in panel f.*

to the [001] azimuth of the copper substrate. The epitaxial alignment deduced from the XRD measurement is illustrated in Fig. 6.3 e,f. The top view (Fig. 6.3 e) of the (001) lattice plane shows the characteristic herringbone arrangement. In the side view (Fig. 6.3f), it becomes apparent that the orientation of pentacene molecules is nearly perpendicular to the substrate surface. This molecular orientation is highly advantageous for the charge carrier transport abilities in common transistor geometries, where charge transport parallel to the substrate surface is important. A tilt angle of only ∼ 3° from the substrate surface normal ensures a significant overlap between adjacent π-orbitals.[43,133] Considering the strong tendency of pentacene to form different polymorphic phases when crystallizing in thin films,[80,128,131,146]it is notable that the chosen growth parameters clearly determine one distinct polymorphic phase as the most favorable. For instance, on SiO_2, usually a thin film phase coexists with a single crystal phase, unavoidably leading to grain boundaries, which strongly lower the charge carrier mobility.[129]

The LEED of the multilayer prepared on the monolayer 1 also shows an epitaxially oriented structure but with some rotational disorder. The dimensions of the deduced rectangular unit cell with a = 0.78 nm and b = 0.61 nm and the unit cell vectors being parallel to the copper azimuths are in perfect

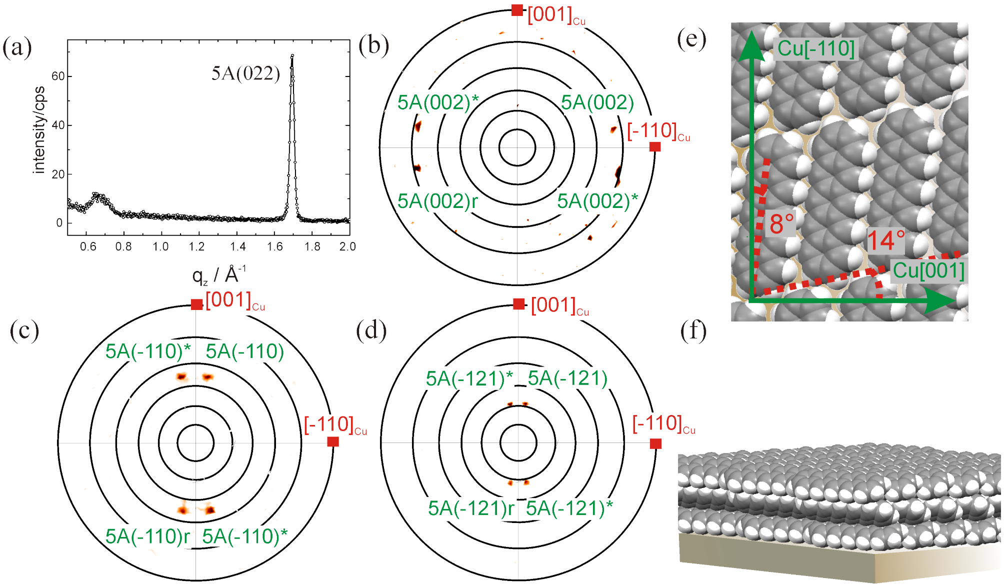

Figure 6.4: *XRD measurements of a pentacene thin film grown on Cu(110) surface. The multilayer film was deposited on the monolayer 2. (a) The specular scan shows that pentacene crystallizes in a "single crystal phase" with the (022) lattice plane parallel to the Cu(110) substrate surface. Pole figures measured at (b) q_z = 0.89 Å^{-1}, (c) q_z = 1.36 Å^{-1}, and (d) q_z = 1.99 Å^{-1} reveal well-ordered, epitaxially aligned domains. The top view of this molecular orientation is shown in panel e, and the side view is shown in panel f.*

accordance with the two-dimensional unit cell of the 5A$_t$(001) net plane found by XRD and thus corroborate standing molecules in the multilayer.

6.3.2 Lying Pentacene Films

In Fig. 6.4, XRD measurements of the film prepared on the monolayer 2 formed by thermal desorption are summarized. Also here, the specular scan (Fig. 6.4 a) exhibits only one Bragg peak and thus indicates a single polymorphic phase with one crystal orientation parallel to the substrate surface. The Bragg peak measured at $|q| = 1.69$ Å^{-1} can be assigned to the (022) net plane of a "single crystal" phase [5As(022)] reported by Mattheus et al.[39] with the following unit cell parameters: a = 0.6266 nm, b = 0.7775 nm, c = 1.4530 nm, $\alpha = 76.475°$, $\beta = 87.682°$, and $\gamma = 84.684°$. This orientation implies that the molecules are lying with their long axes parallel to the surface, while the molecular plane is tilted by ± 26° to it.

The pole figures measured at q= 0.89 Å^{-1} (Fig. 6.4 b), q =1.36 Å^{-1} (Fig. 6.4 c), and q = 1.99 Å^{-1} (Fig. 6.4 d) confirm the 5A$_s$(022) lattice plane as the orientation parallel to the substrate. The EPDs in these pole figures reveal four domains of well-ordered crystallites: domains of crystallites that are rotated by 180° and their mirrored domains. Azimuthally, the crystallites align with the 5A[1$\bar{2}$.10]* [This notation indicates the crystallographic direction, which is parallel to the normal vector of the lattice plane $(1\bar{2}.10)$] direction parallel to the Cu[110] azimuth. For this orientation, the molecules adopt a lying arrangement (see Fig. 6.4 e,f) where the long molecular axis encloses an angle of approximately 8±2° with the Cu[110] direction.

The LEED measurements of this multilayer film reveal an ordered epitaxially oriented structure. The structure of the multilayer is described by a unit cell with the dimensions a = 6.2 Å, b = 30.3 Å, and ϕ=79°. This is not the primitive unit cell one would expect from the 2D unit cell of the $5A_s(022)$ lattice plane measured by XRD (a = 6.27 Å, and b = 14.79 Å), but it can be explained by a (1x2) reconstruction of the surface of the organic crystallites where, for instance, every second pentacene molecule is either missing or has a different orientation.

6.3.3 Monolayer Base for Upright Molecules

For a better understanding of the mechanisms determining the crystallographic structure and the specific epitaxial orientation of the multilayer films, LEED measurements of the first monolayer provide great assistance. The LEED pattern of the monolayer 1 shown in Fig. 6.5 a reveals a well-ordered structure. The corresponding oblique unit cell exhibits the parameters a = 1.69 nm, b = 0.73 nm, and ϕ= 112.29° and is described by the following epitaxial matrix:

$$M_1 = \begin{pmatrix} 6.5 & -1 \\ -0.5 & 2 \end{pmatrix} \tag{6.1}$$

which is related to the Cu(110) substrate surface with the unit cell vectors: **a**= (2.55, 0) and **b** = (0, 3.6). The epitaxial matrix M_1 indicates a so-called point-on-line coincidence as both elements in the second column are integers. In this epitaxial alignment, every lattice point of the pentacene monolayer coincides with the [110] line of the Cu(110) substrate.

Point-on-line coincidence is often observed in the organic-inorganic heteroepitaxial growth,[79,80,147–149] and for these systems, Mannsfeld et al.[150] have demonstrated that such an alignment represents a minimum in the total interface potential. Furthermore, the dimensions of the observed oblique unit cell corroborate an arrangement of flat lying molecules. From UPS measurements, it is known that pentacene adsorbs with its long molecular axis parallel to the Cu(110) substrate and along the Cu[110] crystallographic direction in agreement with (sub)monolayer of the 5A on Cu(110) in the literature.[94,132,139–142]In the real space image of the monolayer 1, this molecular orientation is used (Fig. 6.5 b).

6.3.4 Monolayer Base for Lying Molecules

The LEED image of the monolayer 2 formed by thermal desorption shows a well ordered pattern, but only few reflexes are visible (Fig. 6.6 a). A detailed analysis reveals that this pattern is composed of two different structures. In addition to the already discussed oblique monolayer structure M_1, also a rectangular

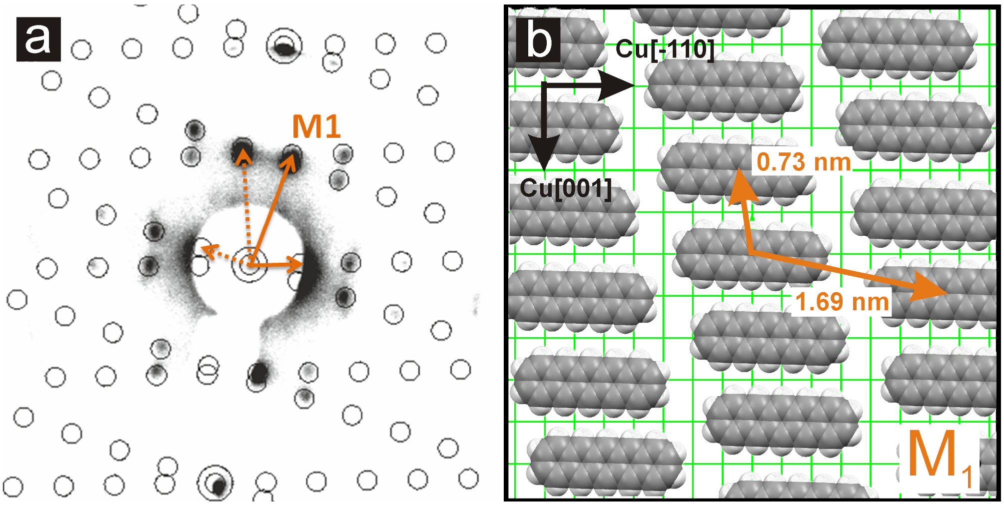

Figure 6.5: *(a) LEED image of the monolayer 1 exhibits one single structure. (b) It is described by an oblique unit cell with parameters: a = 1.69 nm, b = 0.73 nm, and* ϕ*= 112.9°.*

unit cell is found, which in the real space can be expressed by the following commensurable epitaxial matrix (see Fig. 6.6 b):

$$M_2 = \begin{pmatrix} 6 & 0 \\ 0 & 2 \end{pmatrix} \tag{6.2}$$

This matrix describes a commensurable, rectangular p(6x2) unit cell with the lattice parameters a = 1.53 nm and b = 0.72 nm. Exactly the same pentacene monolayer structure formed on Cu(110) surfaces was previously reported by Chen et al.[94] A similar p(6.5×2) unit cell was found by Söhnchen et al.[132]

In the LEED patterns of the multilayer, the oblique unit cell (M_1) of the monolayer is still visible, indicating an island-like growth of the multilayer. Of note is that the rectangular unit cell (M_2) of the monolayer is no longer visible, suggesting that the three-dimensional $5A_s(022)$ crystallites grow on these areas, although it cannot be ruled out that the M_2 rearranges. Although both discussed multilayers [$5A_t(001)$, $5A_s(022)$] grow with a defined epitaxial relationship with respect to the monolayers and substrates, their relationship is not simple, and the structures are incommensurable.

6.3.5 Film morphologies

The AFM images of the film with upright-standing molecules [$5A_t(001)$] reveal terraced islands, which are the typical morphology for the growth of upright standing molecules.[130,134,151] The terraces reveal an average step height of 1.4±0.1 nm as expected for upright standing molecules. The scale-up of these terraced islands shows that the terraces form rather distinct angles, suggesting facets of the azimuthally oriented thin film phase crystallites (Fig. 6.7 a). The facets as indicated in Fig. 6.7 a enclose an angle of approximately 78° around the Cu[001] direction, suggesting the (110) and $(1\bar{1}0)$ planes of the crystallites

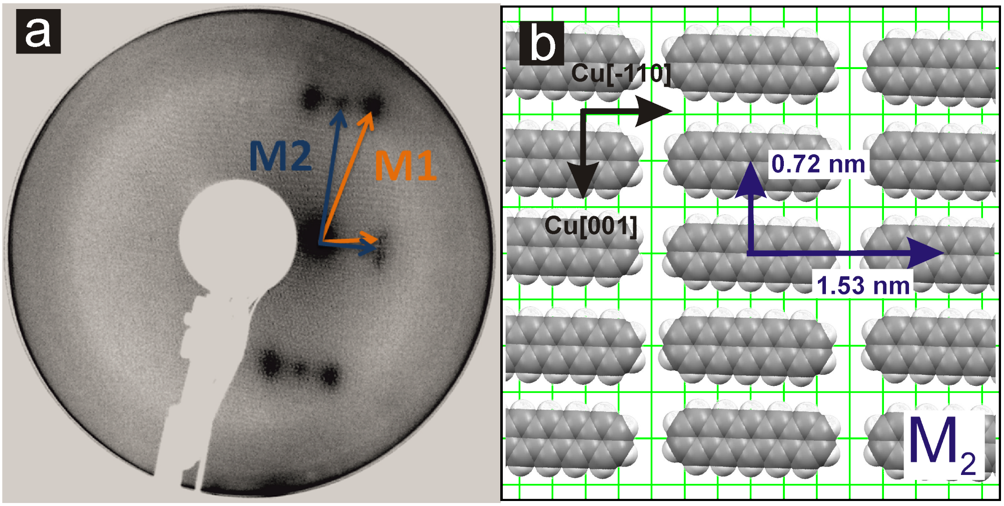

Figure 6.6: *(a) LEED pattern of the monolayer 2 formed by thermal desorption is composed of two different structures. (b) Additionally, to the oblique structure M_1 as observed in the monolayer 1, also a rectangular p(6×2) unit cell is found (M_2).*

(see Fig. 6.3 e). A difference to the standard 5A AFM morphologies reported is that the step edges are decorated with rounded structures of around 50 nm width and two molecule lengths height. We suggest that these might give rise to the partial rotational disorder observed in LEED. Note, unlike XRD, which showed no evidence for rotational disorder, LEED is surface area sensitive.

The film consisting of $5A_s(022)$ crystallites reveals a quite different morphology. Unlike the film of the upright standing molecules [$5A_t(001)$], which covers the entire substrate, here, severe islanding is present. Crystallites are covering $\sim 50\%$ of the surface with the wetting monolayer structure M_1 between them. The 3D structures consist of crystallites that have aggregated into islands as shown in Fig. 6.7 b. These islands are composed of individual grains (see Fig. 6.7 b inset) with a typical length of 800 nm, width of 300 nm, and height of 70 nm. Both the angles of the individual crystallites and the agglomerated island and their relation to the underlying Cu azimuth are in accordance to the angles deduced from the XRD measurements (see Fig. 6.4 e).

6.4 Discussion

Here, we have shown that under identical growth conditions (rate of deposition and substrate temperature), on the same single crystal substrate, two very different epitaxially oriented films of pentacene can be grown. The only identifiable reason for the difference lies in subtle differences in the first monolayers on which the films grow. In the case where the monolayer exhibits an oblique two-dimensional unit cell, the pentacene films grow in an upright fashion in the multilayer [$5A_t(001)$]. However, when the monolayer additionally consists of a rectangular unit cell, the long molecular axes in the multilayer remain parallel to the substrate, while the molecular planes roll by 26° around them, forming

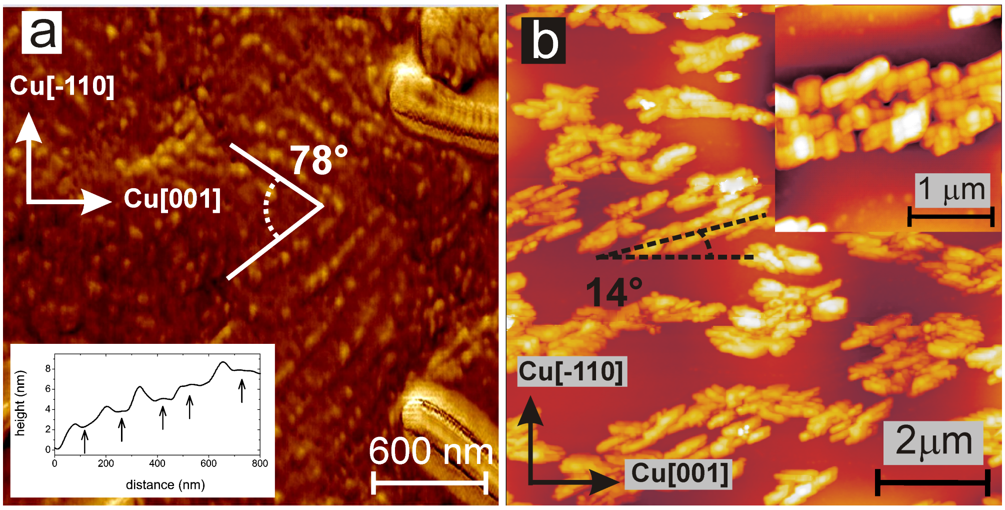

Figure 6.7: *(a) AFM phase scan of the film with standing molecules. The height profile in the inset is taken from a height scan not shown here. (b) 10 µm×10 µm topography image (color scale: 200 nm), inset: 2.5 µm×2.5 µm image (color scale: 100 nm). The film consisting of flat-lying molecules exhibits the morphology of elongated islands.*

the $5A_s(022)$ crystallites. As the monolayers are very similar, in both density and the orientation of the molecules within them, the interaction of adsorbing second layer molecules with the monolayers should be very similar.

We therefore speculate that the different crystalline films are a consequence of differences in the kinetics of molecules on the two different wetting monolayer structures. For anisotropic molecules on anisotropic substrates, we have previously shown the importance of one-dimensional diffusion on wetting monolayers for the growth of crystallites of lying molecules.[152] Although the interaction of arriving second layer molecules with the monolayers will be weak, they will orient parallel to the monolayer molecules (i.e., along [110]Cu) and will diffuse in this direction. In the case of the rectangular monolayer structure, the one-dimensional diffusion along the monolayer surface corrugation will be undisrupted. Molecules diffusing on neighboring channels can interact and, having their long molecular axes parallel, maximize their interactions, facilitating the formation of critical nuclei of $5A_s(022)$ crystallites, which then grow via sticking to island anisotropy. Such a mechanism has been invoked for the rodlike molecules sexiphenyl and sexithiophene on TiO2(110) and Cu(110)(2×1)O substrates, where crystallites of molecules aligned parallel to the substrate surface and surface corrugations are also found.[151,153–155]

In contrast, on the oblique monolayer structure (Fig. 6.5 b), there are no clear one-dimensional diffusion channels for molecules in the second layer, but rather, zigzag paths will be forced upon them. This will lead to diffusing second layer molecules meeting non-parallel and to become parallel and thus maximize π-π interactions they stand up, thus creating seeds for the (001) crystallite orientation. Naturally, this would imply that disordered substrate surfaces will ensure growth of films of upright molecules. Indeed, amorphous substrate surfaces such as Al-oxide, SiO_2, or Si where the first monolayer is strongly bound with a disordered lying monolayer[156] always lead to films of upright molecules. Note that the reactivity of the substrate per se is irrelevant; clean but disordered Cu(110) (sputtered but not annealed) yields a disordered monolayer of lying molecules on which films of upright pentacene grow.[145] However, unlike on the ordered oblique monolayer, the films are rotationally disordered with no relationship to the substrate azimuths.

6.5 Conclusion

Epitaxially aligned pentacene multilayer films with two very different types of molecular orientations and polymorphic structures were grown on Cu(110) surfaces. An explanation for the different growth behaviors of the films can be found in subtle differences within the monolayer structures. When the monolayer consists of an oblique unit cell, pentacene molecules grow in epitaxially ordered domains of upright-standing molecules crystallizing in the “thin film” phase with the (001) lattice plane parallel to the Cu(110) substrate.

However, when the monolayer additionally exhibits a rectangular unit cell, molecules arrange with their long molecular axes parallel to the surface and the “single crystal” phase with the (022) net plane parallel to Cu(110) is formed. To be able to fully explain the underlying kinetics driving the specific molecular orientations of these films, further theoretical development of growth dynamics is needed.

Chapter 7

Periodically deposited heterostructures of α-sexithiophene/para-hexaphenyl thin films on muscovite mica(001) surfaces: crystallographic structure and morphology

The work presented in this chapter is submitted to the journal *Journals of Materials Chemistry* and is essentially identical to the submitted article. Figure 7.1 shows the title of the article and all contributing authors.

Abstract. Multi-component systems of α-sexithiophene (α-6T) and para-hexaphenyl (p-6P) molecules show great promise for tuning the fluorescence colour of optically active films. As the opto-electronic properties of rod-like molecules in thin films strongly rely on their anisotropic orientation, a technique for preparation of well-defined, anisotropic multicomponent systems is required. We demonstrate that a p-6P film of less than two nanometers thickness grown on muscovite mica(001) substrates acts as efficient alignment layer for epitaxial growth of α-6T crystallites. On top of such p-6P alignment layer multilayer heterostructures of alternately deposited p-6P and α-6T molecules were grown. Combined x-ray diffraction and transmission electron microscopy studies show that molecules forming α-6T crystallites align parallel to those in the p-6P crystallites leading to a perfect adoption of their herring-bone structures. This alignment is desirable for optical applications and we show that it is preserved for heterostructures composed of up to 120 alternating p-6P (0.8 nm) and α-6T (3.4 nm) layers (120 cycles). Although for co-evaporated α-6T/ p-6P molecules formation of a mixed crystal polymorph is reported, we show that

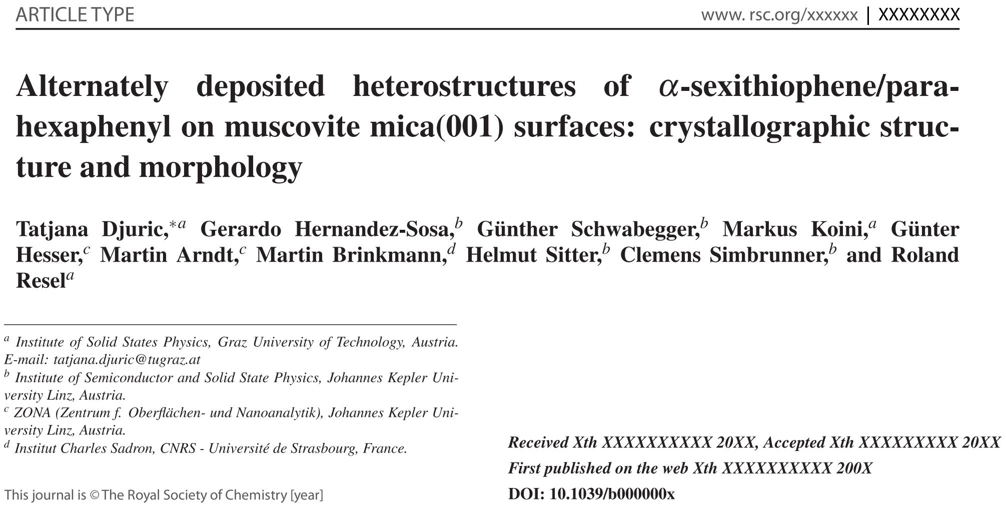

ARTICLE TYPE www. rsc.org/xxxxxx | XXXXXXXX

Alternately deposited heterostructures of α-sexithiophene/para-hexaphenyl on muscovite mica(001) surfaces: crystallographic structure and morphology

Tatjana Djuric,[*a] Gerardo Hernandez-Sosa,[b] Günther Schwabegger,[b] Markus Koini,[a] Günter Hesser,[c] Martin Arndt,[c] Martin Brinkmann,[d] Helmut Sitter,[b] Clemens Simbrunner,[b] and Roland Resel[a]

[a] *Institute of Solid States Physics, Graz University of Technology, Austria. E-mail: tatjana.djuric@tugraz.at*

[b] *Institute of Semiconductor and Solid State Physics, Johannes Kepler University Linz, Austria.*

[c] *ZONA (Zentrum f. Oberflächen- und Nanoanalytik), Johannes Kepler University Linz, Austria.*

[d] *Institut Charles Sadron, CNRS - Université de Strasbourg, France.*

This journal is © The Royal Society of Chemistry [year]

Received Xth XXXXXXXXXX 20XX, Accepted Xth XXXXXXXXX 20XX

First published on the web Xth XXXXXXXXXX 200X

DOI: 10.1039/b000000x

Figure 7.1: *Header of the draft submitted to the journal Journal of Materials Chemistry. It shows all contributing authors and the corresponding affiliations.*

in periodically deposited α-6T/p-6P heterostructures phase separation occurs and both molecules crystallize in their well-known equilibrium structures.

7.1 Introduction

Para-sexiphenyl (p-6P, $C_{36}H_{26}$) and α-sexithiophene (α-6T, $C_{24}H_{14}S_6$) surely are amongst the most important rod-like molecules intended for applications in organic semiconductor devices like organic light-emitting devices (OLEDs)[157–159] and organic field-effect transistors (OFETs).[49,51,160] To ensure efficient charge carrier transport, high structural anisotropy with well-defined orientation of the molecules within the organic layers is required.[13,14,160]

Highly ordered p-6P thin films can be obtained by epitaxial growth on muscovite mica(001) surfaces.[161–165]When deposited on a muscovite mica(001) surface p-6P molecules first form a closed monolayer of flat lying molecules.[166] Subsequently formed crystallites arrange epitaxially to long (μm range) and highly ordered self-assembled needles.[79,162–164,167] Para-sexiphenyl molecules forming highly anisotropic needles show a high quantum yield in the blue spectral regime[168] and more remarkably the elongated shape of the needles enables wave guiding and lasing.[169,170] Due to the structural similarity between p-6P and α-6T, muscovite mica(001) substrates were considered as favourable templates for the growth of α-sexithiophene thin films as well.[171–173] However, morphological and structural studies have shown that - although α-6T molecules tend to arrange in needle-like structures on muscovite(001) surfaces - their epitaxial alignment is much more complicated.[161,172,174] They show multi-directional azimuthal alignment which is strongly disadvantageous for the formation of long nano-fibres and thus suppresses waveguiding and lasing.

Classical inorganic/organic heteroepitaxy has extensively been utilized for the growth of anisotropic crystalline organic films. Only more recently also the potential of organic/organic heteroepitaxy was recognized.[17,78,175–177] Koller et al. (2006) have shown that the approach of organic-organic heteroepitaxial growth of p-6P and α-6T molecules enables to grow thin films with high crystallinity and well-defined interfaces thus meeting the requirements for applications as active materials in organic semiconductor devices.[17] In addition to that, organic/organic heteroepitaxy enables adjusting the physical properties of the organic multilayers as well. In particular, for p-6P/α-6T bilayers on muscovite mica(001) surfaces Simbrunner et al. (2010)[177] have shown that an α-6T layer deposited on top of a p-6P layer changes the emission color from blue to green. Furthermore, through the deposition on highly ordered p-6P template fibres the multiple azimuthal orientations of α-6T needles - as observed on bare mica(001) substrates - are suppressed. Due to the anisotropic molecular alignment of p-6P as well as of α-6T crystallites, highly polarised fluorescence in the green range is observed.

In order to obtain a more precise tuning of the emission chromaticity of p-6P/α-6T nanofibers the heteroepitaxy bilayer approach was extanded to a system of periodically, i.e. alternately, deposited α-6T and p-6P layers grown on top of a p-6P template layer.[178] In this work, we focus on the structure and morphology of such periodically grown p-6P/α-6T heterostructures grown by hot-wall epitaxy (HWE). Particularly, it is of interest to investigate how the periodical deposition influences the crystallization behaviour of the two molecular species. Beside the entropy term, also the particular intermolecular interactions determine whether a regular solution (random mixing), ordered mixed crystal (solid solution) or phase separation will occur.[179–183] Generally, unless the mixed molecules show a high degree of structural compatibility, phase separation is expected when two molecular compounds are mixed.[184,185]

In principle, α-6T and p-6P molecules comply with the requirements for building mixed crystals: they are of similar size (van der Waals length of 2.61 nm (α-6T) and 2.87nm (p-6P)) and in the equilibrium they form the same type of crystal structure (monoclinic, space group 14) with a herring-bone packing.[51,52] Moreover, for co-evaporated α-6T/p-6P heterostructures Vogel et.al (2010)[186] have demonstrated that they indeed form mixed crystals and that the length difference between the two molecules is crucial for their mixing behaviour. The smaller α-6T molecules are integrated into a crystal network of the larger p-6P molecules forming a mixed crystal with an intermediate interlayer spacing; the opposite scenario is not observed. In particular, it is of interest to observe how the structural properties of the films prepared by periodically deposition of p-6P and α-6T layers differ from the co-evaporated ones.

Using X-ray diffraction (XRD), transmission electron microscopy/diffraction (TEM/TED), Auger electron spectroscopy (AES) and atomic force microscopy (AFM) the crystallization behaviour of periodically deposited p-6P/α-6T organic-organic heterostructures is investigated. By combining these methods the evolving crystallographic phases, the arrangement of molecules relative to each other as well as the resulting morphology of the films are determined.

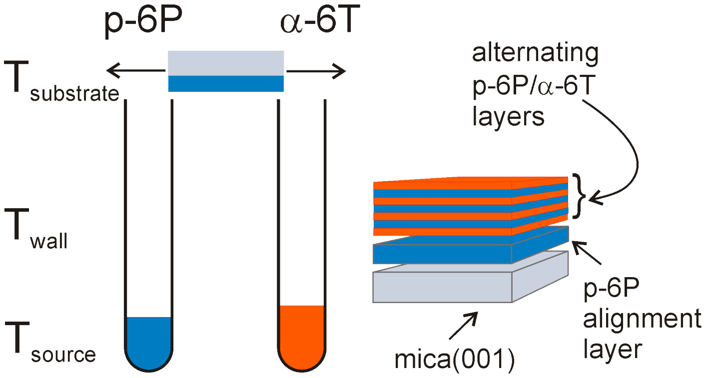

Figure 7.2: *Sketch illustrating the deposition of alternating p-6P/α-6T layers on a muscovite mica(001) substrate using the hot wall epitaxy system equipped with two separated growth reactors.*

7.2 Experimental Section

7.2.1 Sample preparation

Table 7.1: *Nominal thicknesses of p-6P (t6P) and α-6T (t_{6T}) layers deposited in a single cycle at T_{sub}= 120 °C on a 33 nm thick p-6P template layer. The total thickness of the formed multilayer heterostructures is kept constant: $t_{total,6P}$= 98.1 nm and $t_{total,6T}$= 405 nm.*

number of cycles	$t_{total,6P}$	$t_{total,6T}$
0	98.1	-
1	98.1	405
10	9.8	40.0
30	3.3	13.5
75	1.3	5.6
120	0.8	3.4

The samples were prepared by hot wall epitaxy (HWE) operated under high vacuum conditions with a nominal pressure of 9×10^{-6} mbar. Cleaved muscovite mica(001) (SPI, Structure Probe, Inc.) substrates were transferred via load lock to the growth chamber and have been preheated at the chosen substrate temperature T_{sub} (90°/120°C) for 30 min. This step cleans the surface and helps to avoid temperature gradients during the growth. The used compounds p-6P (TCl) and α-6T(Sigma-Aldrich) were placed in two separated reactors in the growth chamber (see Fig.7.2). The optimized evaporation temperature for the source materials p-6P (α-6T) is found at T_{source}= 240 °C (190 °C), respectively. The wall temperature is set to T_{wall}= 260 °C. The selected growth parameters lead to a nominal growth rate of 3.27 nm/min (4.5 nm/min). The nominal thickness used in this article is defined as the average fibre height. For the growth of α-6T molecules on p-6P template layers T_{sub} was set to 90 °C or 120 °C, respectively.

For the fabrication of periodically grown heterostructures T_{sub}= 120 °C was selected. The first step in the preparation of the periodically grown samples is the deposition of a p-6P template layer for 10 min (32.7nm). Subsequently, the periodical deposition of p-6P and α-6T molecules is initialized. The repetition unit of one p-6P and one α-6T layer in the subsequently initialized periodic deposition is denoted a *deposition cycle*. In this study, samples prepared with 0, 1, 10, 30, 75 and 120 cycles are discussed. The totalized thickness t_{total} of all periodically deposited samples is kept constant (p-6P: t_{total},6P= 98 nm, α-6T: t_{total},6T= 405 nm). Accordingly, the nominal thickness grown in a single cycle depends on the total number of deposition cycles (see Table 7.1).

7.2.2 X-ray diffraction measurements

X-ray diffraction specular scans and reciprocal space maps (RSMs) were measured on a Bruker D8 Discover diffractometer in the Bragg-Brentano configuration using CuKα radiation (λ=1.54 Å). RSMs provide an illustrative cross-section of the reciprocal space. The variation along the q_z-direction at q_x=0 corresponds to a specular scan, i.e. to Bragg peaks of lattice planes exactly parallel to the sample surface. The variation along q_x for a constant q_z value is equivalent to rocking curves indicating the mosaicity of the crystallites, i.e. for a given Bragg peak it is representative for the tilting of the corresponding lattice planes relative to the substrate. The diffractometer was equipped with conventional slit optics and a graphite monochromator on the secondary side. Pole figure measurements were performed on a Philips X?Pert X-ray diffractometer with CrKα radiation (λ=2.29 Å). For the assignment of Bragg peak position POWDER CELL[109] was used and the simulation of the pole figure measurements was done with STEREOPOLE.[108]

7.2.3 Transmission electron microscopy

For transmission electron microscopy/diffraction (TEM/TED) measurements carbon coated samples were removed from the muscovite substrate by floating on a dilute HCl (hydrofluoric acid) solution and were subsequently recovered on copper TEM grids. TEM investigations were performed in bright field (BF) and selected area electron diffraction (SAED) modes using a Philips CM12 microscope (120 kV) equipped with MVIII CCD camera. Calculation of the electron diffraction (ED) patterns was carried out using the program Cerius2 (Accelrys).

Cross sectional TEM measurements were carried out on a JEOL 2011 microscope (200 kV, LaB_6) attached with an OXFORD EDX-System for elemental analysis. Sample preparation with the focused ion beam technique was carried out using a ZEISS XB 1540 Crossbeam after depositing an aluminium layer by thermal deposition. The Auger images were taken at a tilt angle of 30° to the 30 kV primary electron beam and 30° to the concentric hemispherical analyzer (CHA) as a good compromise between distortion and count rate. Each Auger image consists of 128x128 pixels with a dwell time 50 ms per pixel. For the C

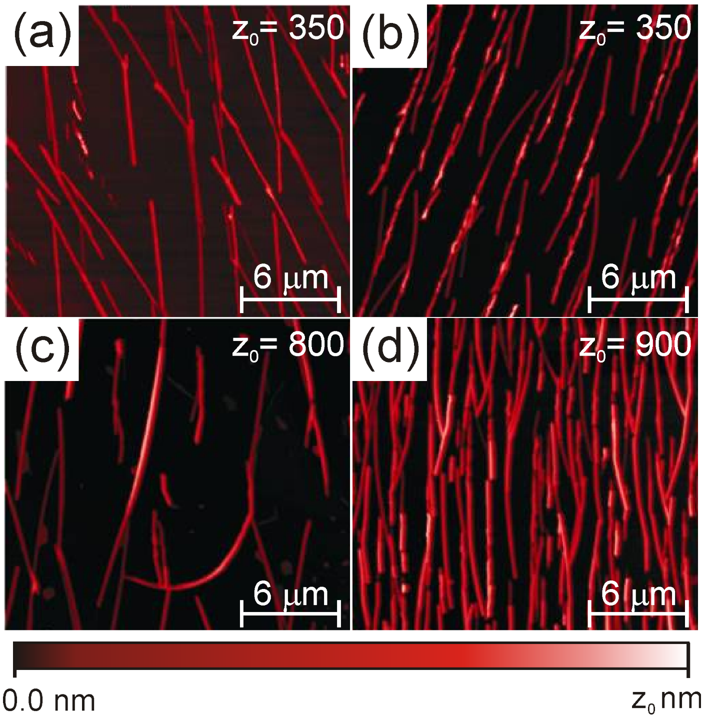

Figure 7.3: *AFM measurements of α-sexithiophene films (200 nm) grown on p-sexiphenyl templates. Templates were prepared at different substrate temperatures* T_{6T} *and template thicknesses* t_{6P}*: a)* T_{sub}*=90 °C,* t_{6P}*=0.3 nm b)* T_{sub}*=90 °C, d6P= 1.6 nm c)* T_{sub}*=120 °C, d6P=0.3 nm d)* T_{sub}*= 120 °C,* t_{6P}*= 1.6 nm.*

image the KLL Auger peak at 263 eV was used and for the S mapping the LVV Auger peak at 146 eV, respectively. For further analysis each image has been normalized to its maximum intensity and the translative offset of the different images has been corrected. By calculating iso-intensity lines of the normalized Auger image data [65% (S), 73%(C)] sulphur and carbon rich regions have been deduced. Finally the resulting data has been overlayed with the TEM image originating from the same organic nano-fibre.

7.2.4 Atomic force microscopy

Atomic force microscopy (AFM) studies of the deposited nano-fibres were performed using a Digital Instruments Dimension 3100 in the tapping mode. The AFM characterization was performed on an area of 30 mm^2 with a SiC tip. The pixel resolution was chosen with 512×512 pixels. The zero height has been corrected by levelling the data to the minimum height of the whole image.

7.3 Results

7.3.1 Growth of α-6T molecules on p-6P template layers

Before turning to central topic of this article (periodically deposited α-6T/p-6P heterostructures), we investigate the influence of the p-6P alignment layers on the subsequently deposited α-6T molecules in a simple bilayer system. The role of the template layer thickness on the alignment of the α-6T molecules is investigated, an issue not discussed in the recently published results on bilayer α-6T/p-6P nano-fibers.[177] Further on, TEM/TED measurements of a bilayer system are presented which are subsequently used as reference system for the periodically deposited α-6T/p-6P heterostructures.

AFM measurements summarized in Fig. 7.3 show that already very thin layers of p-6P act as efficient templates for the alignment of subsequently deposited α-6T molecules (t_{6T}=45 min, 200 nm). When deposited on an only 0.3 nm thick p-6P template layer (corresponds to one monolayer[166]) grown at T_{sub}=90 °C α-6T molecules arrange in needle-like aggregates but still show a strongly pronounced multidirectionality (Fig. 7.3 a). However, already a template thickness of 1.6 nm (Fig. 7.3 b) is sufficient to significantly reduce the branching of the α-6T needles. Also samples prepared at an elevated substrate temperature (T_{sub}=120 °C) were investigated and we observe that the directionality of the α-6T needles is further improved (Fig. 7.3 c). This is in line with the general observation that the morphology of (template) fibres improves with increasing substrate temperature.[187] Moreover, we find that an increased thickness of the p-6P template layer also remarkably increases the nucleation density of the α-6T needles (Fig. 7.3 d).

To demonstrate that a p-6P template layer with a thickness of 1.6 nm is sufficient to induce high azimuthal anisotropy of the subsequently deposited α-6T molecules, the morphology as well as the crystallographic properties of these films were investigated in detail by TEM and TED in high resolution. A representative α-6T thin film grown on a 1.6 nm thick p-6P template at T_{sub} = 90 °C (see Fig. 7.3 b) is discussed here. Besides the long branched α-6T needles (length: 10-30 μm, width: 0.1-0.3 μm) which were already observed in Fig. 7.3, TEM bright field images additionally reveal elongated islands (Fig. 7.4 a). Their dimensions are uniformly distributed with a typical length of approximately 50 nm and a width of 20 nm. Figure 7.4 b shows that α-6T needles align nearly parallel to these elongated islands. Pure p-6P films prepared with comparable growth time (t_{6P}= 26 s) at the same T_{sub} = 90 °C have shown an uniform coverage with elongated islands of similar dimensions.[164]

They were reported to crystallize in the β-structure of p-6P[52] with the $(11\bar{1})$ lattice planes aligned parallel to the muscovite mica(001) substrate surface (contact plane). This orientation corresponds to nearly flat lying molecules. Hence, the morphology observed in Fig. 7.4 is already a first hint that elongated islands are composed of p-6P crystallites exhibiting preferentially the $(11\bar{1})$ contact plane. For further examination, high-resolution images (HR-TEM) of such elongated islands were taken. The Fourier Transform (FT) of a single island (see inset of Fig. 7.4 b) reveals a periodicity of about 2.65 nm which is in good agreement to the (001) spacing of the p-6P crystal structure (d_{001}= 2.60 nm) and corroborates that the elongated islands are indeed composed of p-6P molecules with the $(11\bar{1})$ contact plane parallel to substrate.

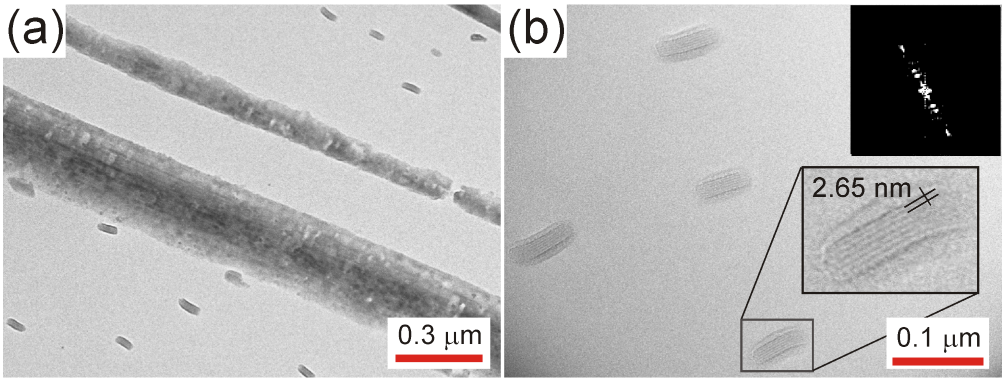

Figure 7.4: *a) TEM bright field image of a 200 nm thick α-6T film grown on a 1.6 nm thick p-6P template layer. b) High-Resolution TEM image of p-6P elongated islands. The inset in the right corner shows a Fast Fourier Transform of a single island.*

Figure 7.5 summarizes representative electron diffraction (ED) patterns observed for the discussed sample. Calculated patterns are shown in the left column; they are individually or collectively present in the measured diffraction patterns shown in the right column. Fig. 7.4 b shows an exemplary simple diffraction pattern originating from the edge of the large needle seen in the defocused SAED image in the inset. The diffraction pattern depicted in Fig. 7.4 a) was in a first step calculated using the low temperature crystal structure of α-6T[51] assuming the $[\bar{3}\ \bar{2}5\ 42]$ zone axis (alignment of the $(\bar{4}11)$ lattice plane parallel to the substrate surface). Depending on the tilt from this assumed zone axis, different reflexes appear (indicated by dashed lines in Fig. 7.5 a for the two strong series $(h\bar{1}\bar{1})$ and $(h\bar{2}\bar{1})$). Perfect agreement (Fig. 7.5 b) with the measured pattern was here obtained by tilting the assumed zone axis by 3.8° degrees, indicating that the orientation of the crystallite is slightly tilted in respect to the $(\bar{4}11)$ lattice plane. This orientation implies that the long molecular axis (LMA) of α-6T molecules is nearly parallel to the substrate surface. In addition to the edge of a thick needle also few elongated islands are present in the area shown in the inset. As their scattering volume is rather small the contribution to the diffraction pattern is rather weak.

Figure 7.5 d shows an ED pattern where domains with slightly varying tilts from the $(\bar{4}11)$ lattice plane are contributing (marked by rectangles); their positions lie along the dashed line shown in Fig. 7.5 a. The diffraction spots marked by circles are stemming from the p-6P$(11\bar{1})$ crystallites (compare with the calculated pattern in Fig. 7.5 c). Here, diffraction spots of both molecular species are present, enabling a determination of their relative azimuthal orientation. Generally in an ED pattern, lattice planes perpendicular to the contact plane are visible. Here, we observe that in-plane the $(3\bar{2}\bar{1})$ lattice plane of α-6T crystallites has arranged nearly parallel to the $(2\bar{1}\bar{3})$ lattice plane of p-6P crystallites. Both lattice planes are parallel to the edge-on molecules in the corresponding crystal structures and they have a similar lattice spacing: $d_{3\bar{2}\bar{1}}$= 3.217 Å for α-6T and $d_{2\bar{1}\bar{3}}$= 3.116 Å for p-6P. Their alignment parallel to

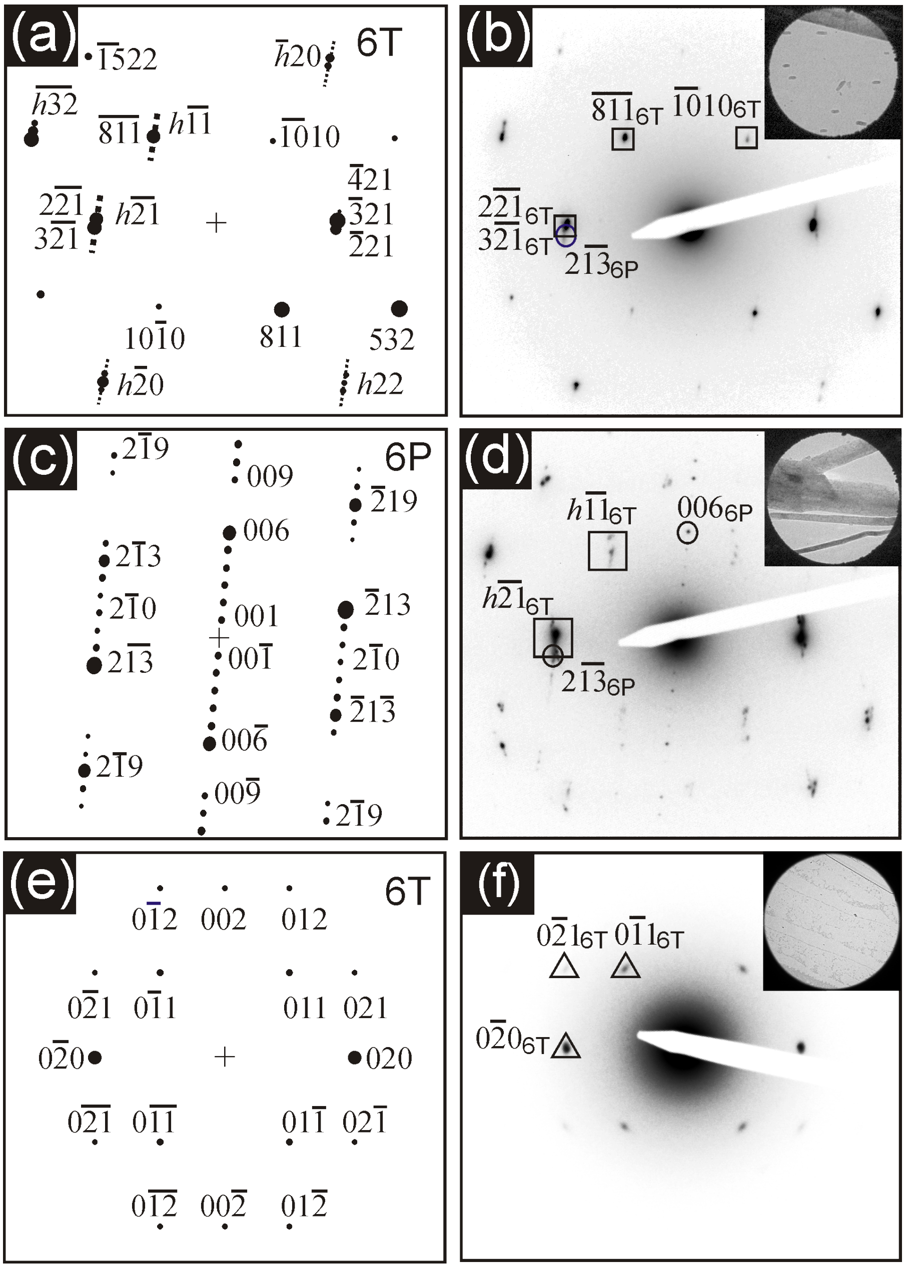

Figure 7.5: *Left column shows calculated electron diffraction (ED) patterns: a) for the low temperature phase of α-6T assuming a [-3 -25 42] zone axis (rectangles), c) for the α-phase of p-6P assuming the [1 2 0] zone axis (circles) and e) for the low temperature phase of α-6T assuming a [100] zone axis (triangles). Right column shows measured diffraction patterns for a 200 nm thick a-6T film grown on a 1.6 nm thick p-6P template layer with indexed reflexes. The insets show the corresponding defocused image of the diffracting area.*

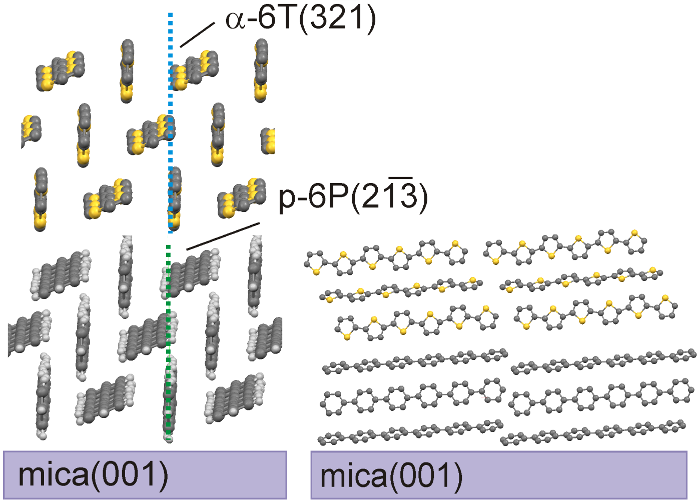

Figure 7.6: *Molecules as arranged in p-6P/ α-6T heterostructures on the muscovite(001) substrate. On top of the p-6P layer α-6T crystallites are formed. In the left panel the view along the long molecular axis, in the right panel perpendicular to it is shown.*

each other has the effect that α-6T crystallites perfectly adopt the herring-bone structure of the p-6P crystallites with both molecular species showing identical orientation (see Fig. 7.6).

Figure 7.5 f finally shows a diffraction pattern which is measured only in few regions on the sample. It shows a perfect agreement with the theoretical pattern (Fig. 7.5 e) calculated using the low temperature phase of α-6T and assuming the [100] zone axis (corresponds roughly to the (100) contact plane). α-6T crystallites exhibiting this contact plane are formed by molecules which are nearly perpendicular to the substrate surface. The corresponding morphology shown in the defocused SAED (inset) exhibits rather low contrast indicating small thicknesses in this area. Such islands of upright α-6T molecules are frequently observed on muscovite mica(001) substrates.[171,172,174,188] As the diffraction pattern as well as the defocused selected area image does not indicate underlying p-6P elongated islands, the upright α-6T molecules are most probably growing directly on the mica substrate surface.

To summarize the orientations of the crystallites found in α-6T thin films grown on p-6P template layers: elongated islands of p-6P(11$\bar{1}$) crystallites induce epitaxial growth of needle-like α-6T($\bar{4}$11) crystallites (Fig. 7.6). In between these needle-like structures also a population of α-6T(100) crystallites corresponding to standing molecules are observed which most probably grow directly on the substrate.

7.3.2 Periodic α-6T/p-6P multilayer heterostructures

For bilayer systems of p-6P and α-6T molecules showing high azimuthal anisotropy a shift in the spectral emission from blue to green was demonstrated.[177] More precise tuning of the emission chromaticity is possible using a modified heteroepitaxy approach where α-6T and p-6P molecules are deposited alternately on top of each other (on top of a p-6P template layer on mica).[178] To obtain well-defined and densely packed thin films a growth temperature of T_{sub}= 120 °C was chosen (see Fig. 7.3). As shown, the thickness of the p-6P alignment layer does not play a major role for the alignment of 6T($\bar{4}11$) crystallites; here, we are using a 33 nm thick p-6P template layer to avoid the formation of 6T(100) crystallites. The preparation of such heterostructures is schematically shown in Fig. 7.2 and explained in detail in the experimental section. Samples prepared by deposition cycles as listed in Table 7.1 were investigated.

For these systems to be useful for optical applications it is essential to preserve the epitaxial alignment observed in bilayer systems (Fig. 7.6). Therefore, it is of interest to investigate if the periodical deposition affects the crystallization behaviour of the two molecules. It is known that aromatic molecules often form solid solutions (mixed crystals).[185,189,190] Due to the high structural compatibility of the respective molecules (see Introduction), a formation of solid solutions is a plausible scenario as well. Most commonly, substitutional solid solutions are formed, where molecules of the one kind replace molecules of the other kind and occupy exactly the same crystal site.[189] The effect of such a substitution on the newly formed crystal structure can be phenomenologically described by Vegard's law: the new lattice constants are the weighted (by concentration) average of the lattice constants of its components.[185] Also so-called "structural mimicry"[191] is observed, where the lattice constants of the formed mixed crystal do not change as the minor component adopts the structure of the dominant one.[29,191,192] If no solid solution is formed at all, molecules either crystallize in separate phases or form an amorphous phase.

Therefore, when investigating the structural properties of periodically deposited p-6P/α-6T heterostructures, the following questions arise: a) Is the azimuthal alignment of the p-6P/α-6T crystallites preserved? b) Does the number of deposition cycles have an influence on the epitaxial alignment of the formed crystallites? and finally c) Do the two components mix on the molecular level and form solid solutions?

TEM/TED measurements

Figure 7.7 summarizes TEM and TED measurements performed on a 1-cycle sample (left column) and on a 120-cycles sample (right column). The diffraction pattern measured for the 1-cycle sample shown top left is basically identical to the one obtained for the α-6T film grown on a p-6P monolayer (Fig. 7.5 d). It yields the information, that both molecules have crystallized in their well-known equilibrium structures and the relative orientation of the formed crystallites is such that the LMAes of the molecules are arranged parallel. The defocused image in the inset shows the real image of the diffracting area (bright circle) revealing nearly parallel aligned needles. The bright field image depicted in the middle of the left column shows the morphology of the 1-cycle sample in higher magnification. When compared with the well-studied morphology of p-6P needles, here additionally needle-like structures are evident which exhibit strong contrast, appearing nearly black.[162] The strongly enhanced contrast points towards height differences in respect to the underlying needle-structures. To prove this assumption, rotational tilt was performed; figure at the bottom left corner shows the morphology of the sample tilted by 35°. It reveals that structures growing on top are significantly higher than the underlying needle-like structures. In this two-layer system (one cycle) α-6T molecules are deposited on top of a p-6P layer, hence these unusual wall-like morphologies correspond to α-6T crystallites. These wall-like structures appear to be flexibly bendable rather than rigid which could be also an explanation for the often found variations in the diffraction patterns assigned to α-6T crystallites of lying molecules.

The multilayer heterostructure shown in the right column of Fig. 7.7 is prepared by 120 deposition cycles, where the nominal thicknesses of the single p-6P and α-6T layers are 0.8 nm and 3.4 nm, respectively. The typical diffraction pattern shown at the top is a superposition of different diffraction patterns making the assignment to specific orientations of the involved crystallites increasingly difficult. Contributions from p-6P$(11\bar{1})$ and α-6T(100) crystallites are indicated by circles and triangles, respectively. Other diffraction spots, most probably due to α-6T$(\bar{4}11)$ crystallites, cannot be assigned unambiguously. However, the bright field image shown in the middle reveals that the deposited molecules still arrange in rather parallel and long needles. Also here, the morphology with enhanced contrast is present and indicates wall-like morphologies. In contrast to the previously discussed 1-cycle sample, for the 120-cycles sample α-6T(100) diffraction patterns corresponding to upright standing α-6T molecules are more often observed. Consistently, in the bright field images additional features beside the needle like-structures are present. Beside the small nuclei which are reminiscent to the elongated islands observed for p-6P in the monolayer regime (cf. Fig. 7.3), we observe flat islands with low contrast - a morphology typical for crystallites of upright standing α-6T molecule (see encircled area in the bottom right corner). This finding suggests that fast deposition cycles render the crystallization of α-6T in islands of upright-standing molecules more favourable. This orientation is preferentially found on substrates exhibiting weak interaction with the deposited molecules.

For a better discrimination of domains containing p-6P and α-6T molecules, respectively, a cross-sectional TEM measurement with a combined Auger electron spectroscopy of a 10-cycle sample was performed (Fig. 7.8). In the HR-TEM image shown in Fig. 7.8 a two different regions can be distinguished: in the lower part as well as on the left side regions with periodic modulation of intensity are visible; contrary, the triangular inclusion in the middle does not show any periodic structures. A FFT analysis of the region marked by a white circle yields a periodicity of 2.8 nm, which is in good agreement with the lattice

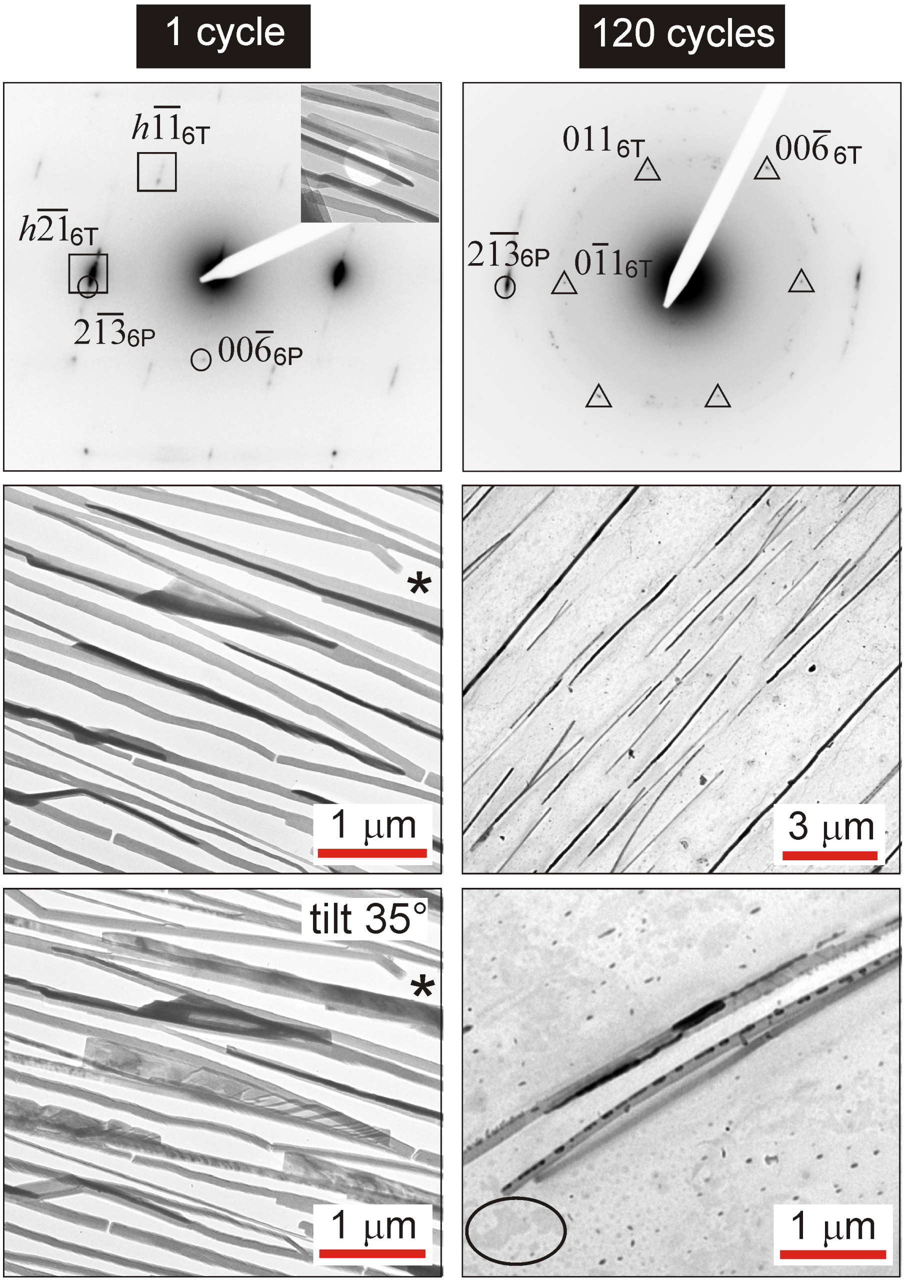

Figure 7.7: *The left column shows TEM results obtained for a 1-cycle sample. A typical electron diffraction pattern is depicted at the top. The bright field image in the middle shows the typical morphology. Below, the same area tilted along the long needle axis by 35° is shown. Asterisks denote the same area on the sample. The right column depicts TEM results measured for a 120-cycles sample. At the top a typical electron diffraction pattern is shown. In the middle the corresponding bright field image is depicted. On the bottom right higher magnification of the observed needle-like structures is shown. Reflexes are denoted according to Fig. 7.5.*

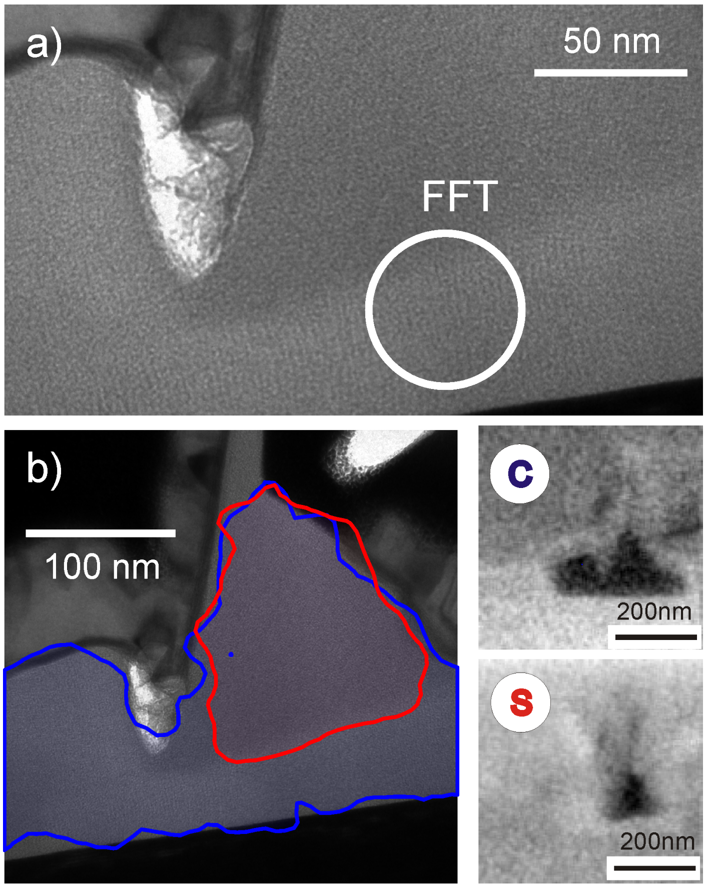

Figure 7.8: *a) Cross-sectional transmission electron microscopy (TEM) image of a p-6P/α-6T multilayer heterostructure prepared by 10 deposition cycles. b) TEM image with overlaid isointensities measured by Auger electron spectroscopy: carbon (blue) and sulfur (red). c) On the right side images for carbon and sulfur rich domains, respectively, are shown.*

spacing d_{001} of the p-6P crystal structure (compare Fig. 7.4 b). This suggests phase separation: regions showing periodicities correspond to p-6P$(11\bar{1})$ crystallites while most probably a region containing α-6T molecules is visible in the middle of the image. To substantiate this assumption Auger electron spectroscopy was measured (Fig. 7.8 b). Here, blue lines correspond to regions where signals from carbon are detected and red lines denote presence of sulfur atoms (and hence α-6T molecules). In regions showing periodicity in the HR-TEM image (Fig. 7.8 a) indeed only carbon atoms are measured, corroborating that pure p-6P(11-1) crystallites have formed. Contrary, the triangular structure in the middle additionally contains sulphur atoms, indicating the presence of α-6T molecules. However, the image in Fig. 7.8 a does not allow to deduce the crystal structure present in the triangular region. Therefore, we cannot conclude whether in this region solely α-6T molecules crystallize in their equilibrium structure as measured for the 1 cycle sample or if mixed crystals form.

In conclusion, for the 10 and 120-cycle samples in (cross sectional) TEM

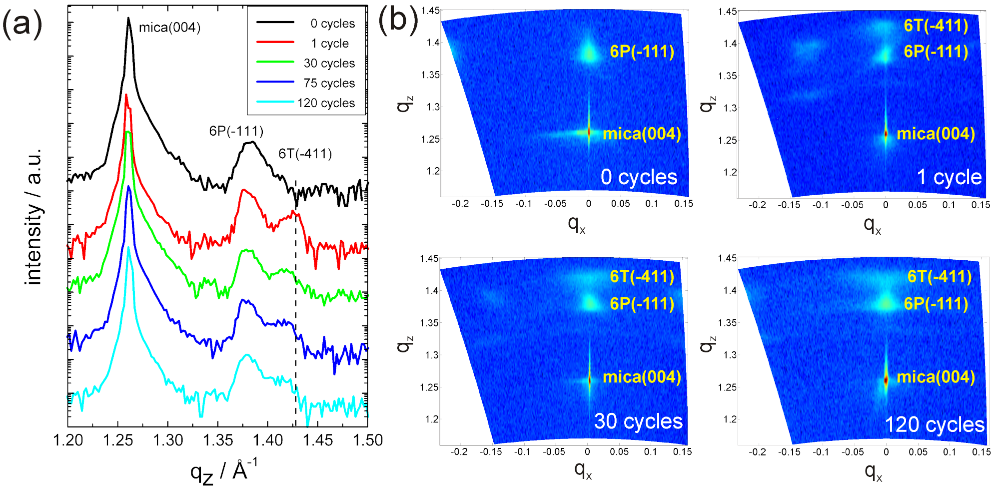

Figure 7.9: *Fig. 8: (a) X-ray diffraction specular scans of periodically grown 6P/6T layered heterostructures (0, 1, 30, 75 and 120 cycles). (b) Corresponding x-ray diffraction reciprocal space maps for samples grown with 0, 1, 30 and 120 cycles.*

we clearly observe p-6P crystallites oriented with the $(11\bar{1})$ lattice plane parallel to the substrate surface as well as α-6T molecules crystallizing in the low temperature phase with the (100) contact plane. However, to corroborate that the α-6T molecules still arrange in $(\bar{4}11)$ oriented crystallites with their LMAes parallel to those of p-6P molecules (as the bright field images in Fig. 7.7 e,f suggest), complementary XRD measurements are required.

XRD reciprocal space maps

Figure 7.9 a shows XRD specular scans for the periodically grown p-6P/α-6T heterostructures summarized in Table 7.1. Measured Bragg peaks indicate lattice planes parallel to the substrate surface. The 0-cycles sample is a pure p-6P thin film consisting of a 33 nm thick p-6P template layer and one p-6P layer (98.1 nm) on top of it. A peak at $\mathrm{q_z}= 1.383$ Å^{-1} is measured in addition to the (004) peak of the muscovite substrate ($\mathrm{q_z}= 1.26$ Å^{-1}). It can be assigned to the p-6P$(11\bar{1})$ lattice plane of the β-phase with the lattice spacing measured at $\mathrm{d}_{11\bar{1}}= 4.57\pm0.01$ Å. In the specular scan of a 1-cycle sample (additional deposition of a 405 nm thick α-6T layer) a new peak at $\mathrm{q_z}= 1.420$ Å^{-1} appears which is attributed to the $(\bar{4}11)$ lattice plane of α-6T low temperature phase measured at $\mathrm{d}_{\bar{4}11}= 4.42\pm0.01$ Å. These measurements confirm the orientations observed by TEM/TED measurements very well (cf. Fig. 7.7). More interestingly, specular scans reveal that the α-6T$(\bar{4}11)$ orientation is present for all observed films, even those prepared by 120 deposition cycles. However, the α-6T(100) orientation which was observed in TED (Fig. 7.7 d) is not present in the specular scan. The corresponding α-6T islands grow between the needle-like structures (Fig. 7.7 e, f) and their scattering volume is too small for detection with XRD as opposed to the locally more sensitive ED.

To examine how the mosaicity, i.e. degree of crystalline order parallel to the substrate surface, depends on the number of deposition cycles x-ray diffraction reciprocal space maps (RSM) were measured (for details, see experimental section) and are summarized in Fig. 7.9 b. The peaks measured in the RSM for the 0-cycle sample can be assigned to the (004) peak of the muscovite substrate and the (11$\bar{1}$) peak of p-6P (Fig. 7.9 b). The corresponding rocking curve of the p-6P(11$\bar{1}$) peak yields a rocking width of 0.5°, a rather small value for organic thin films which indicates highly oriented crystallites. For the 1-cycle sample the position and the rocking width of p-6P(11$\bar{1}$) remains constant and additional the α-6T($\bar{4}$11) peak appears. The latter exhibits a rocking width of 1.4° which is significantly larger than for p-6P crystallites but is still indicative for well-aligned crystallites. The α-6T($\bar{4}$11) peak shifts to smaller values with increasing number of deposition cycles , a trend also clearly visible in the specular scan (dashed line in Fig. 7.9 a). Figure 7.10 a, which illustrates the deviations of measured peak positions from their literature values, shows that the positions of the muscovite(004) and p-6P(-111) peaks basically remain constant when the number of deposition cycles is increased. In contrast, the position of maximum intensity assigned to the α-6T(-411) peak increasingly deviates from its literature value ($d_{\bar{4}11}$= 4.4213Å), with the largest difference amounting to $d_{\bar{4}}11$= 0.05 Å for 120 cycles. The same is true for the mosaicity: for the p-6P crystallites no significant changes are seen contrary to α-6T crystallites.

The change of the α-6T($\bar{4}$11) lattice spacing is rather continuous as is seen best in RSM of the 120-cycles sample (Fig. 7.9 b, bottom right panel), where the corresponding Bragg peak appears considerably broadened. Evaluating the mosaicity (Fig. 7.10 b shows the rocking widths with increasing number of deposition cycles) we distinguish between two different α-6T peak positions. On the one hand we consider the initial position of the α-6T($\bar{4}$11) peak which agrees with its literature value of q_z= 1.420 Å^{-1} (upside down triangles). On the other hand we analyze also the rocking curves for the actual q_z-value of maximum intensity for a given sample, i.e. shifted one (triangles). The mosaicity for the crystallites with the initial $d_{\bar{1}11}$ (literature) value strongly increases, while for the specific peak of maximum it nearly remains constant. In other words, as the number of cycles is increased also the ($\bar{4}$11) lattice spacing in the α-6T crystallites increases, and this leads to higher orientational order (smaller mosaicity than for the initial $d_{\bar{4}11}$). This result brings up the question if the change in the lattice spacing points towards a formation of a mixed phase.

Pole figure measurements

In contrast to specular scans, which probe lattice planes oriented parallel to the substrate surface, pole figure measurements give information on the orientational distribution of all lattice planes with a finite structure factor. This enables an efficient determination of the actual crystal structures as well as of the epitaxial relationship between involved crystallites. As the herring-bone arrangement of p-6P and α-6T molecules in the corresponding crystal structures is rather similar, most of the high intensity lattice planes are at the identical scattering angle and pole direction. Therefore, for measuring the pole figures

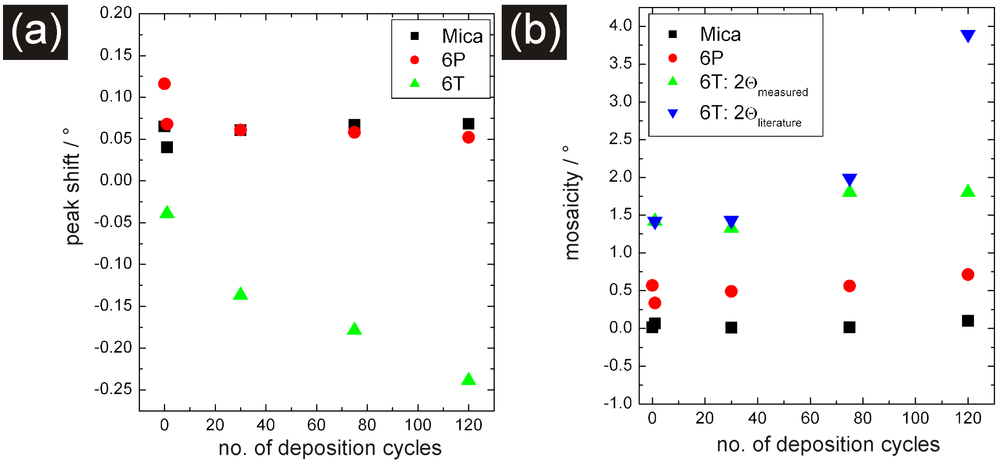

Figure 7.10: *(a) Shift of the measured Bragg peak positions from their literature values depending on the number of deposition cycles. (b) The mosaicity of the corresponding Bragg peaks as function of the number of the deposition cycles.*

lattice spacings were chosen in a way such that detectable diffraction intensity is present exclusively for one of the two crystal structures: d_{006}= 4.33 Å for p-6P crystallites (q= 1.424 $Å^{-1}$) and $d_{12.00}$= 3.73 Å for α-6T crystallites (q=1.687 $Å^{-1}$) enables distinguishing between contributions from the two molecular species.

Pole figures of a one-cycle sample measured for p-6P (d_{006}) and α-6T ($d_{12.00}$) are shown in Fig. 7.11 a and b, respectively. The measured enhanced pole densities (EPD) marked with red crosses stem from the muscovite mica(001) substrate. In Fig. 7.11 a EPDs that are not due to muscovite mica can be assigned to the β-phase of p-6P assuming the $(11\bar{1})$ lattice plane parallel to the substrate surface. The two indexed domains are mirrored in respect to each other. Corresponding domains rotated by 180° lie closely to the indexed ones and for the sake of clarity are not indexed here. Measured reflexion spots are rather narrow indicating that the in-plane order of p-6P crystallites is well defined. Furthermore, the epitaxial alignment of the p-6P molecules in respect to the muscovite substrate can be derived: we observe that the long molecular axis (LMA) of p-6P encloses an angle of 82°±2° with the [110] direction of the muscovite substrate. This finding is in line with the previously observed behaviour of p-6P molecules on muscovite substrates.[79] The pole figure measured for the (12.00) lattice plane of α-6T is shown in panel b and can be interpreted as the low temperature phase of α-6T with the $(\bar{4}11)$ lattice plane parallel to the substrate surface. The rather sharp EPDs are again indicative of well-aligned domains. Further, as the arrows in the corresponding pole figures indicate, the LMA of α-6T molecules is oriented exactly parallel to the LMA of p-6P. This means they have arranged parallel adopting the same orientation of their herring bone packing as it was also observed in the TEM/TED measurements (see Fig. 7.5).

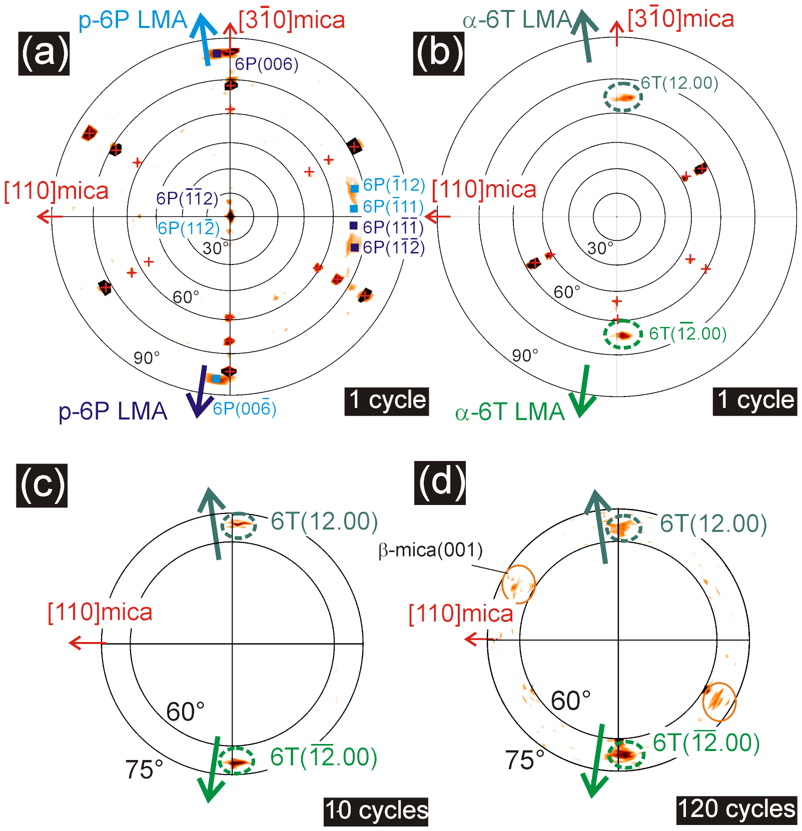

Figure 7.11: *(a) Shift of the measured Bragg peak positions from their literature values depending on the number of deposition cycles. (b) The mosaicity of the corresponding Bragg peaks as function of the number of the deposition cycles.*

This alignment, which is advantageous for optical applications, is preserved even for large numbers of deposition cycles as shown for 10 and 120 cycles in Fig. 7.11 c. For both pole figures only the relevant range $\psi = 60° - -75°$ of the 6T(12.00) pole figure is depicted, as the orientation of the muscovite substrate is the same as in the case of panel b) and that of p-6P crystallites the same as in panel a. The azimuthal alignment of the α-6T crystallites is identical to the one-cycle sample which can be explained by the low temperature phase. We mention for the sake of completeness that muscovite (001) exhibits two cleavage planes which are identical but azimuthally rotated by 120° in respect to each other: α-muscovite(001) and β-muscovite(001) surface.[79,163] Upon cleavage of the substrate surface terraces can form. In this case both muscovite surfaces are present simultaneously, explaining the additionally occurring EPDs encircled by orange circles in lower part of Fig. 7.11 c (the β-muscovite(001) surface); the EPDs discussed above correspond to crystallites formed on the α-muscovite(001) surface.

Summarizing, pole figure measurements (Fig. 7.11) reveal that even for large numbers of deposition cycles p-6P and α-6T molecules phase separate, each forming their equilibrium crystal structure. Hence, the slight change of α-6T

$d_{\bar{4}11}$ lattice spacing observed in the specular scan (Fig. 7.9) does not correspond to a formation of a mixed phase. Most probably this change originates from the strain formed upon the adaptation of α-6T crystallites to the herring-bone structure of p-6P: an inplane lattice spacing contraction (of 6T $d_{32\bar{1}}$= 3.217 Å to fit p-6P $d_{21\bar{3}}$= 3.116 Å) leads to an expansion perpendicular to the substrate surface (i.e. α-6T $d_{\bar{4}11}$).

7.4 Conclusions

We have shown that p-6P alignment layers of less than 2 nm thickness induce epitaxial alignment of subsequently deposited α-6T molecules. The α-6T crystallites grow preferentially with the ($\bar{4}$11) lattice plane of the low temperature phase parallel to the substrate surface. The molecules of α-6T crystallites align with their LMAs parallel to those of p-6P crystallites and the relative in-plane orientation leads to a perfect adoption of their herring-bone structures. For periodically deposited p-6P/α-6T heterostructures it is important to clarify a) whether the formed crystal structures correspond to the equilibrium structures of p-6P and α-6T molecules found in bi-layer systems and b) whether the alternating deposition affects the azimuthal alignment of the evolved crystallites. TEM and TED measurements with combined Auger electron spectroscopy show that in addition to domains containing α-6T molecules, pure p-6P(11$\bar{1}$) crystallites form. Using XRD specular scan and pole figure measurements we could clarify that for all periodically deposited heterostructures phase separated crystallization occurs. In addition to p-6P(11$\bar{1}$) crystallites also α-6T($\bar{4}$11) crystallites form and the relative azimuthal alignment found in the bilayer system is preserved. The only structural change we are observing is a slight adaptation of lattice spacings of the α-6T crystallites to those of p-6P. The consequence is a coexistence of strained and strain free α-6T crystallites, where the latter show a significantly larger mosaicity.

In contrast to the system of co-evaporated p-6P/α-6T molecules,[186] for periodically deposited p-6P/α-6T heterostructures no indication for phase mixing is found. This can be rationalized by the difference in the preparation technique of the periodically-deposited p-6P/α-6T compared to the co-evaporated systems. First, the molecules are deposited alternately not contemporaneously as in the case of co-evaporation. Second, the evaporation technique of hot wall epitaxy used here operates close to the thermodynamic equilibrium. Both aspects facilitate a crystallization of the molecules in their equilibrium structures. Contrary, the co-evaporated systems may be kinetically trapped, leading to metastable mixed phases.

Chapter 8

Impact of zinc phthalocyanine polymorphism on the interface structure of C_{60}/ZnPc heterojunctions

The work presented in this last chapter has been done during my stay in Strasbourg in the group of Martin Brinkmann and is still in progress. This is a summary of results obtained so far; to complete the picture of this system further work is planned.

Abstract. Photophysical properties and charge transport in donor-acceptor (D/A) systems depend crucially on the structure of the D/A interface and the morphology of the D and A layers. In this study, bilayer films combining the organic p-type semiconductor zinc-phthalocyanine (ZnPc) with the electron acceptor fullerene (C_{60}) have been prepared. We have focused on the impact of the structure of the ZnPc layer on the interface formed with C_{60}. To this aim, highly oriented ZnPc films of the α- and the β- forms have been grown on polycarbonate (PC) alignment layers. The detailed morphological and structural study of the bilayered films was performed using UV/VIS absorption spectroscopy, atomic force microscopy, transmission electron microscopy and X-ray diffraction. When grown at T_{sub}= 115 °C, the ZnPc films consist of uniaxially oriented nanocrystals of the α-phase with a preferential (001) surface. Electron diffraction indicates that the C_{60} crystallites grow with a rather "unusual" $(21\bar{1})$ contact plane. For T_{sub}= 200 °C, oriented β-ZnPc crystals are formed with a preferential (001) contact plane and the C_{60} nanocrystals grow with a preferential (111) contact plane. Molecular modelling is used to propose structural models of the D/A interfaces. In the case of α-ZnPc films, C_{60} molecules form rows that are oriented parallel to the columnar stacks of the ZnPc nanocrystals as observed experimentally by High-Resolution Transmission Electron Microscopy.

8.1 Introduction

Already before semiconducting properties of organic molecules came into the focus of device research, metallo-phthalocyanines (MPc) were valuated for their outstanding optical properties. Due to their strong absorption in the red and blue regime, they are used as synthetic pigments. In particular, the blue coloured CuPc ($C_{32}H_{16}N_8Cu$) is often used in inks or for colouring clothing.
More recently, MPcs are also recognized as p-type semiconductor material (electron donors). A great advantage of MPcs is their ability to crystallize easily from vapour phase which makes them ideal materials for the preparation of well-ordered thin films. In addition, they show very good thermal and chemical stability.[59] They have been therefore utilized in many different applications like in organic transistors,[193] photovoltaic devices[10,11,194] or light emitting diodes.[195,196]

In organic photovoltaic devices based on donor-acceptor heterojunctions PcM layers are shown to act as efficient p-semiconductors (see Section 1.2). As most organic molecules behave as electron-donors, the challenging task is finding an efficient electron-acceptor material. The very first two-layer organic solar cells based on CuPc molecules have used a perylene tetracarboxylic derivative (PV) as n-type semiconductor.[194] A remarkable increase in efficiency was achieved by using fullerene C_{60} molecules as electron acceptors.[9–11] The efficiency improvement is mainly due to the extraordinarily long exciton diffusion length of C_{60} of (77±10) Å.[197]

The donor-acceptor interface is of particular importance as it is responsible for the charge separation of photo-generated excitons (cf. Section 1.2). Once the exciton is separated into electron and hole, it is essential to prevent recombination until the charge carriers can reach the electrodes. For these processes to work well, the donor and acceptor layers have to be well-ordered, homogeneous, and the interface well-defined.[198,199]

8.2 Experimental

8.2.1 Preparation of bisphenol A polycarbonate alignment layers

The preparation of PC alignment layers has first been reported by Brinkmann et al. (2007)[200] and further explored by Vergnat et al. (2011).[63,201] The following description as well as Fig. 8.1 are based on these references.
The first step in the preparation of PC alignment layers is properly cleaning the supporting glass slides. This is done by sonication in aceton and ethanol for 15 min each, rubbed with a toothbrush in a Hellemanex solution with subsequent sonication by further 15min in that solution. Finally they are sonicated 3 more times in deionized water and dried in a flow of nitrogene.

The preparation process of oriented PC layers is divided into three steps (see Fig. 8.1):

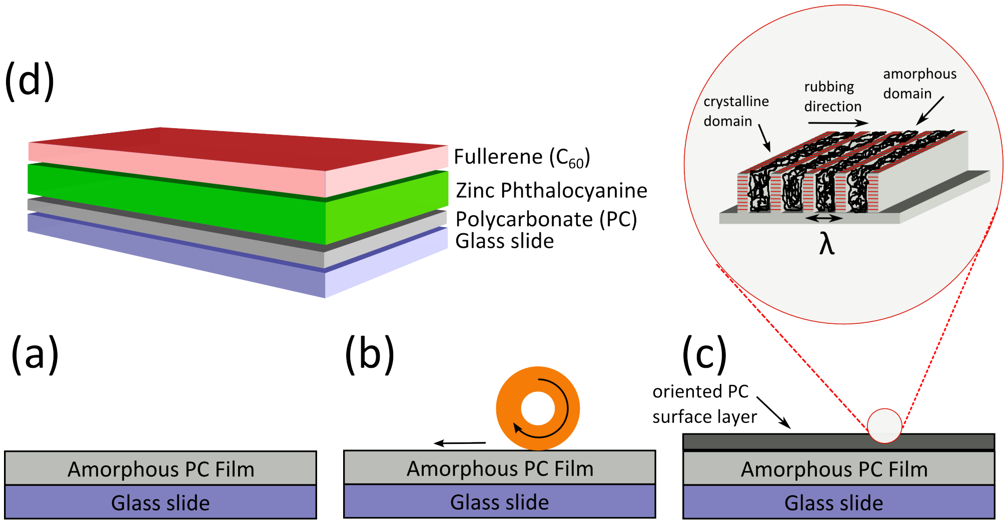

Figure 8.1: *The preparation of the polycarbonate (PC) alignment layer is divided into three steps: a) preparation of an amorphous film by spin coating, b) alignment of the polymer chains near the surface by rubbing and c) solvent vapour smoothing and induced crystallization. Illustration is based on Ref. [200]. d) Schematic representation of samples prepared on near-surface aligned PC layers.*

(a) By spin coating a thin film is prepared (thickness of 200-500 nm); here, the polymer is in its glassy state.

(b) Near the film surface, a uniform orientation is induced by one-directional rubbing, which is performed by a homemade rubbing machine.

(c) Finally, the film is exposed to acetone vapour which reduces the polymer surface roughness formed by rubbing. It further promotes solvent-induced crystallization of PC.

The freshly rubbed PC films exhibit a root-mean-square roughness (rms) of 5 nm ($2\times2\ \mu m^2$); rms is reduced to 0.5 nm after exposure to acetone. Thus, the resulting surface of the PC films is smooth and nano-structured. It consists of a periodic alternation of crystalline lamellae and amorphous interlamellar zones with a periodicity of 20 nm. The crystalline lamellae of PC are oriented preferentially with the (010)–lattice plane parallel to the glass slide and with the $\mathbf{c}_{\mathrm{PC}}$-axis parallel to the rubbing direction.
During the exposure to acetone vapour, the induced crystallization steadily continues from the surface to the bulk. In this work, rather short exposure times were chosen (2-10 min) as already a thin oriented surface layer is sufficient to induce epitaxial growth of molecules deposited on top of it. This is also advantageous, as the PC layer is thin enough to transmit electrons and does not contribute in diffraction experiments.

8.2.2 Deposition of ZnPc/C_{60}-bilayers

After exposing the PC films to aceton vapour, nano-structured semi-crystalline films are obtained which are used as templates for the deposition of the ZnPc

Table 8.1: *Preparation parameters for zinc-phthalocyanine (ZnPc) and fullerene (C_{60}) bilayers deposited on polycarbonate (PC) alignment layers.*
t_{aceton} *. . . exposure time to aceton vapour,* t_{ZnPc} *(*$t_{C_{60}}$*) . . . thickness of the ZnPc (*C_{60}*) layer,* DR_{ZnPc} *(*$DR_{C_{60}}$*) . . . deposition rate of the ZnPc (*C_{60}*) layer,* T_{sub} *. . . substrate temperature*

sample	t_{aceton} [min]	t_{ZnPc} [nm]	$t_{C_{60}}$ [nm]	DR_{ZnPc} [$\mathrm{nm \cdot min^{-1}}$]	$DR_{C_{60}}$ [$\mathrm{nm \cdot min^{-1}}$]	T_{sub} [°C]
B	3	40	20	1.3	0.7	115
C	2	40	20	1.3	0.7	115
D	2	40	10	1.3	0.7	115
E	3	40	10	1.3	0.7	115
G	2	40	2	1.0	0.7	115
H	3	40	2	1.0	0.7	115
Hβ	2	40	20	1.0	0.5	170
I	2	–	20	–	0.4	115
B_1	3	40	20	1.1	0.5	200 / 115
B_{2c}	3	40	–	1.1	–	200
B_{3c}	10	40	20	0.8	–	200
B_4	10	40	20	0.8	0.6	200
XRD_1	3	40	40	1.1	0.4	115
XRD_2	3	40	–	1.1	–	115
XRD_2	2	40	40	1.1	0.4	115

and C_{60} thin films (see Fig. 8.1 d). ZnPc and C_{60} thin films were deposited in high vacuum (10^{-6} mbar) using an Edwards Auto336 evaporator system. The growth mechanisms of ZnPc thin films on oriented PC substrates are well studied.[63,201] Based on this knowledge, a thickness t_{ZnPc} of 40 nm is chosen as here the majority of the ZnPc crystallites are oriented parallel to the PC lamellae. To trace the evolution of the C_{60} thin films on ZnPc surface, the thickness $t_{C_{60}}$ is varied between 2 and 40 nm. The deposition rates DR were monitored using a quartz microbalance and were for all samples constant ($DR_{\mathrm{ZnPc}} = 1.2 \pm 0.2$ [$\mathrm{nm \cdot min^{-1}}$], $DR_{C_{60}} = 0.6 \pm 0.2$ [$\mathrm{nm \cdot min^{-1}}$]). The substrate temperature T_{sub} was varied between 115 and 200 °C. All samples prepared with different growth parameters are listed in Table 8.1.

8.2.3 Investigation techniques

UV/VIS absorption

Before preparing the samples for TEM investigations, optical absorption measurements were performed. These measurement were done by UV-vis-near-IR absorption (300-900 nm) spectroscopy using a Shimadzu UV-2101PC spectrometer with polarized incident light and a spectral resolution of 1 nm. Using a goniometer, the optical absorbance was measured for the direction parallel ($\|$) and perpendicular ($\perp$) to the PC rubbing direction.

Transmission Electron Microscopy

The morphology and the crystallographic properties of the bilayer-films were investigated by Transmission Electron Microscopy in the bright field mode (BF) and by electron diffraction (ED) with a 120 kV Philips CM12 electron microscope equipped with a MVIII CCD camera (Soft Imaging Systems). Samples were coated with an amorphous carbon film and pre-cut into circles to exactly fit on TEM grids. Subsequently, they were floated off on a diluted aqueous HF solution (5%) and recovered onto TEM grids.

8.3 Results

Vergnat et al. (2011) have determined how the polymorphic phase occurring in ZnPc thin films grown on PC alignment layers depends on of the substrate temperature T_{sub}.[63] In the temperature range between 33 °C $\leq T_{\text{sub}} \leq$ 115 °C exclusively ZnPc α_{II}-phase crystallites are formed. For T_{sub} greater than 115 °C β-phase crystallites occur as well; their proportion to the α_{II}-crystallites increases with the increasing T_{sub}. Unit cell parameters of different polymorphic phases are summarized in Section 2.4.4.
ZnPc and C_{60} layers were deposited at different substrate temperatures with the aim of obtaining different polymorphic phases. The structural properties of these bilayer-systems, and how they depend on each other, is described in the following.

8.3.1 Case 1 – ZnPc: T_{sub}= 115 °C, C_{60}: T_{sub}= 115 °C

In this first case, the substrate temperature for the deposition of both molecules was set to 115 °C. Figure 8.2 a shows the UV/VIS absorption spectrum measured for a ZnPc/C_{60}-bilayer with t_{ZnPc}= 40 nm and $t_{C_{60}}$= 20 nm. UV/VIS absorption spectra are characteristic for crystallographic structures and thus enable distinguishing between different polymorphic phases. Both, the α- as well as the β-phase exhibit a Soret band at λ_0 in the range of 335-350 nm, which therefore will is not discussed here. Characteristic contributions λ_1, λ_2 can be seen in the Q-band region ($\pi \to \pi^*$). As known from the literature, for the α-phase the two contributions are located at λ_1= 630 nm and λ_2= 715 nm, while for the β-phase they are shifted to longer wavelengths: λ_1= 640 nm and λ_2= 750 nm.[63] Therefore, the peak positions measured in the UV/VIS spectrum (Fig. 8.2 a) at 634 nm and 724 nm are assigned to the α-phase of ZnPc. A pronounced anisotropy in parallel ($\|$) and perpendicular($\perp$) direction indicates a preferential azimuthal alignment of the ZnPc crystallites parallel to the PC rubbing direction. Contrary, the C_{60} peak is weakly pronounced exhibiting the same intensity for the direction parallel and perpendicular to the rubbing direction (approx. 470 nm). This finding does not necessarily mean that the C_{60} crystallites are randomly distributed. C_{60} usually crystallizes in highly symmetric structures (fcc or hcp, see section 2.4.5) and therefore exhibits an isotropic optical absorption behaviour.

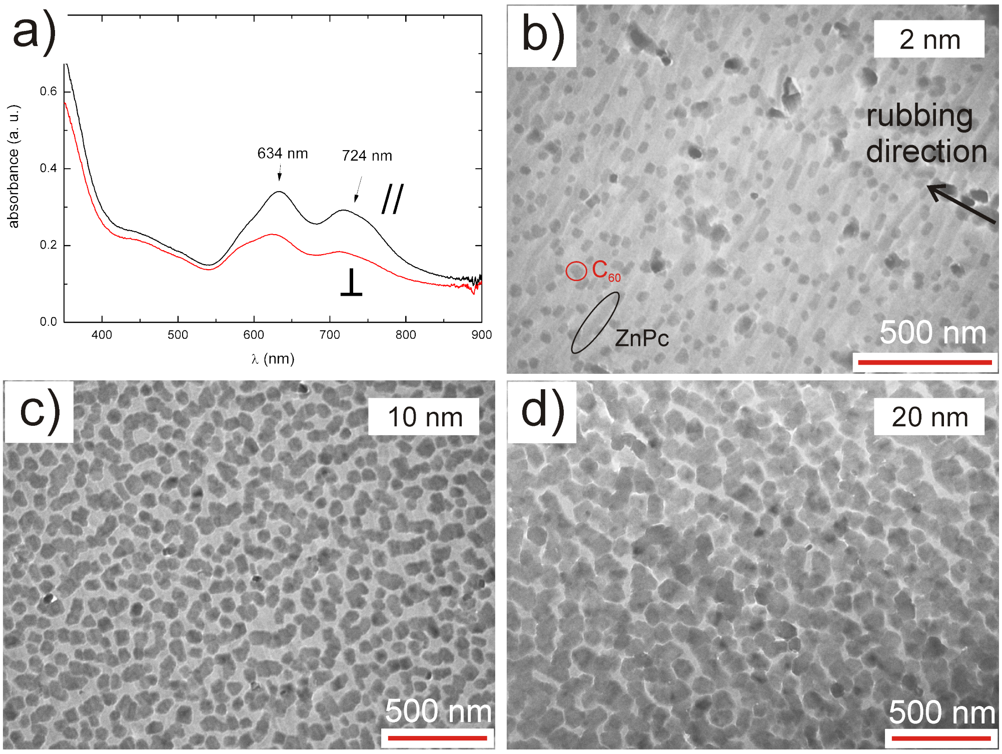

Figure 8.2: *a) UV/VIS absorption spectra measured for a ZnPc/C_{60}-bilayer grown at T_{sub}= 115 °C(t_{ZnPc}= 40 nm, $t_{\mathrm{C}_{60}}$= 20 nm). The black curve corresponds to the absorption measured parallel to rubbing direction of the PC alignment layer (‖), the red curve perpendicular to it (⊥). b)-d) TEM bright field images of ZnPc/C_{60}-bilayers. The thickness of the ZnPc layer is 40 nm, while the thickness of the C_{60} layers varies: b) 2nm, c) 10 nm and d) 20 nm.*

To trace the development of the C_{60} thin film layers, their thickness was varied between 2 nm, 10 nm and 20 nm. TEM images reflecting the morphology of these films are shown in Fig. 8.2 b-d. The image of the 2 nm thick C_{60} film (Fig. 8.2 b) in addition to the hemispherically shaped C_{60} crystallites (30-50 nm) on the top, also shows the underlying elongated ZnPc crystallites; the black arrow indicates the rubbing direction. It is evident that the ZnPc crystalites grow perpendicular to it. In other words, the elongated ZnPc crystallites align parallel to the crystalline lamellae of PC (see Fig. 8.1 c). The C_{60} crystallites deposited on top of them adopt the same orientation. With increasing coverage, the C_{60} crystallites grow further until they start to coalesce to elongated domains of lengths up to 200 nm (Fig. 8.2 c: $t_{\mathrm{C}_{60}}$= 10 nm, 8.2 d: $t_{\mathrm{C}_{60}}$= 20 nm). While the geometrical shape of the crystallites looks rather oblique and hemispherical in the TEM bright field images, AFM measurements show that this is not the case (Fig. 8.3). Already for $t_{\mathrm{C}_{60}}$= 2 nm (Fig. 8.3 a) rectangular shaped crystallites are observed, and for $t_{\mathrm{C}_{60}}$= 20 nm (Fig. 8.3 b) the facets of crystallites are strongly pronounced.

The crystallographic properties of these films were observed by electron

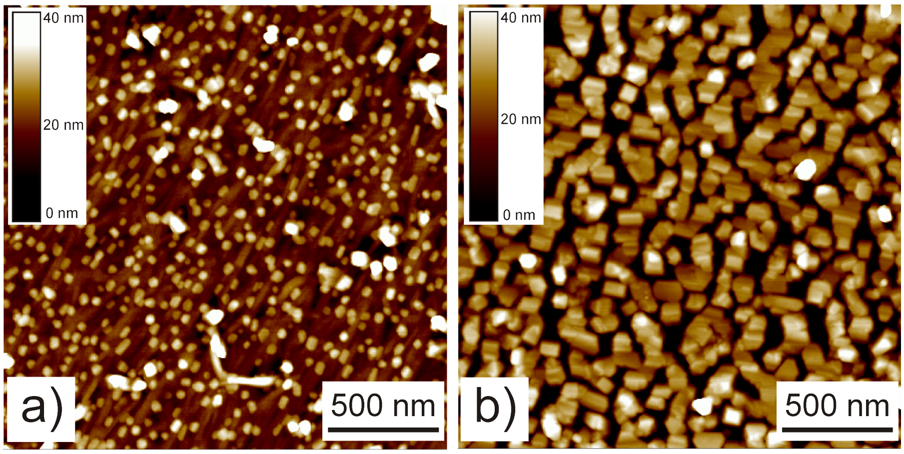

Figure 8.3: *AFM images of ZnPc/C_{60}-bilayers deposited at 115 °C for two different C_{60} coverages: a) $t_{C_{60}}$ = 2 nm and b) $t_{C_{60}}$ = 20 nm.*

Table 8.2: *Interplanar spacings d_{hkl} [Å] of strong reflexes assuming the given zone axis (ZA)*

C_{60} ZA:[$21\bar{1}$]	C_{60} ZA:[111]	α-ZnPc ZA:[001]	β-ZnPc ZA:[102]	β-ZnPc ZA:[112]
d_{111}= 8.12	d_{022}= 4.97	$d_{\bar{1}00}$= 12.25	$d_{20\bar{1}}$= 9.56	$d_{1\bar{1}0}$= 4.60
d_{022}= 4.97		$d_{\bar{2}00}$= 6.13	$d_{40\bar{1}}$= 4.78	$d_{3\bar{1}\bar{1}}$= 3.84
d_{113}= 4.24		$d_{\bar{1}10}$= 3.53	$d_{21\bar{1}}$= 4.28	$d_{31\bar{2}}$= 3.73
		$d_{\bar{2}10}$= 3.10	$d_{41\bar{2}}$= 3.38	

diffraction. Figure 8.4 a shows a representative diffraction pattern measured on a ZnPc/C_{60} film with a 10 nm thick C_{60} layer. The chosen substrate temperature of 115 °C is the upper limit of the regime (33 °C $\leq T_{sub} \leq$ 115 °C), which is reported to mainly yield the α_{II}-ZnPc form.[63] Indeed, the diffraction spots denoted with Laue indices in blue are assigned to the α_{II}-polymorph of ZnPc, assuming the (001) contact plane (corresponds to [100] zone axis; see also Table 8.2). The relatively sharp diffraction spots indicate uniaxial orientation of the crystallites. The relative orientation of the ZnPc molecules having the (001) lattice plane parallel to the substrate surface is shown in Fig. 8.4 b; the molecules adopt an edge-on orientation. By comparison of the real space and reciprocal space images, it is determined that the π-stacking direction of ZnPc (which is the long axis of the nanocrystals) lies perpendicular to the rubbing direction.

The remaining diffraction spots are attributed to C_{60}-molecules crystallizing in a cubic structure with a lattice constant a = 1.4061 nm.[70] The determined contact plane of the C_{60}-crystallites is a rather unusual one, namely the ($21\bar{1}$). The molecular modelling of the ZnPc/C_{60}-interface is shown in side view in Fig. 8.4 b. It illustrates that at the interface, the ball-shaped C_{60}-molecules are embedded into the hollows formed by ZnPc-molecules. The azimuthal alignment of the two molecules in respect to each other leads to a "line-on-line"

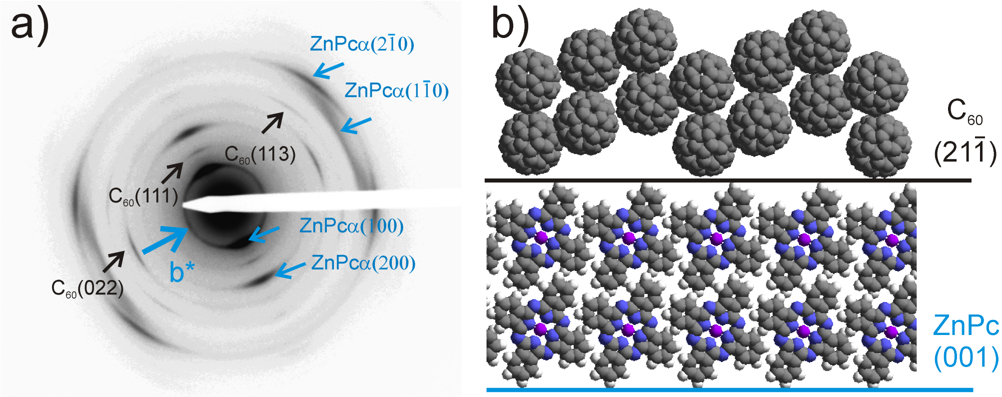

Figure 8.4: *a) Electron diffraction pattern of a ZnPc/C_{60}-biilayer (t_{ZnPc}= 40 nm, $t_{C_{60}}$= 10 nm). Both molecules are deposited at T_{sub}= 115 °C b) Molecular modelling of the ZnPc/C_{60}-interface in the side view.*

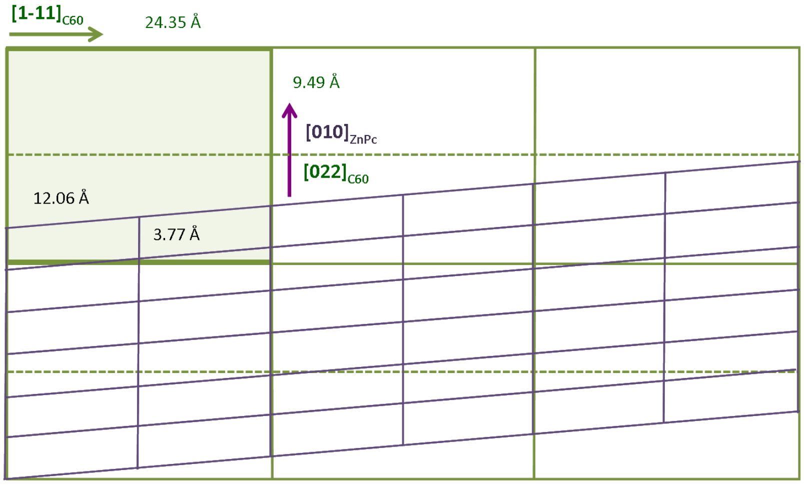

Figure 8.5: *Inplane epitaxial relationship between the ZnPc and C_{60} crystallites at the interface observed for a T_{sub} of 115 °C for both molecules. Purple lines correspond to the ZnPc- and green lines to C_{60}- lattice.*

epitaxial relationship: the [022] direction of C_{60} crystallites is aligned parallel to the ZnPc[010]-direction (Fig. 8.5).

8.3.2 Case 2 – ZnPc: T_{sub}= 170 °C, C_{60}: T_{sub}= 115 °C

To observe how C_{60} molecules crystallize on a template layer of the ZnPc β-phase, the ZnPc-layer was grown at an elevated T_{sub} of 170 °C. For the subsequent deposition of C_{60} substrate temperature was decreased again to 115 °C.

The peaks measured in the UV/VIS absorption at 631 nm and 736 nm (Fig. 8.6 a) indicate that although T_{sub} was increased to 170 °C the major part of the film still crystallizes in the α-phase. The measurements parallel and perpendicular to the rubbing direction of the PC layer show that the ZnPc crystal-

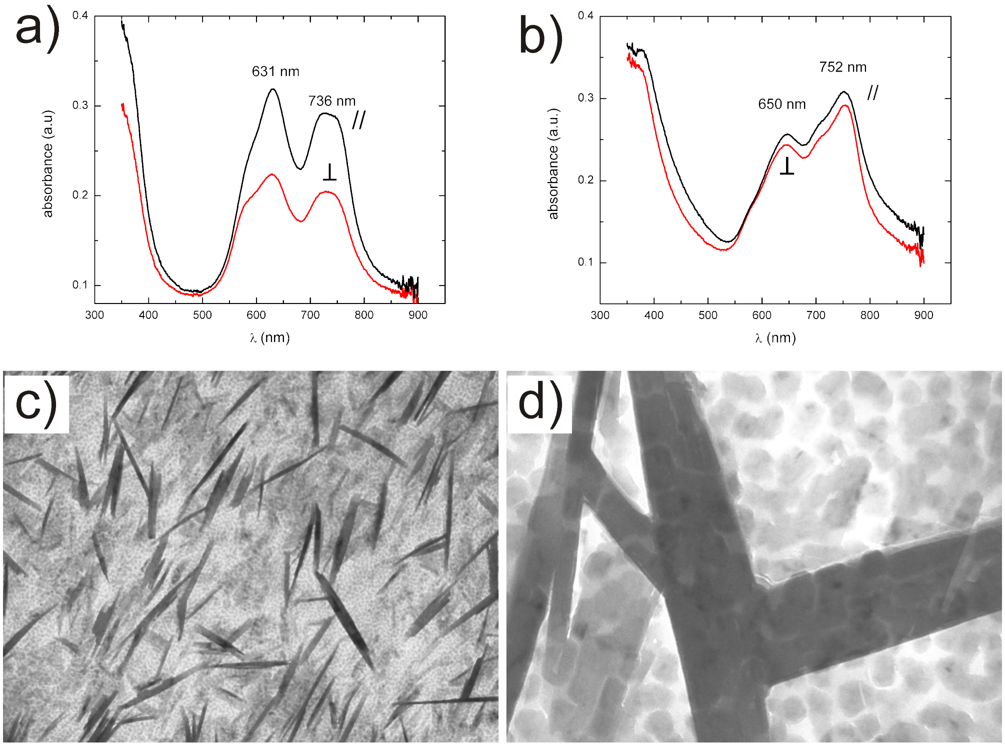

Figure 8.6: *a) UV/VIS absorption spectra for a ZnPc/C*$_{60}$*-bilayer (*t_{ZnPc}*=40 nm,* $t_{\mathrm{C}_{60}}$*=20 nm). ZnPc-layer was deposited at* T_{sub}*= 170 °C and* C_{60}*= 115°. Absorption is measured parallel (∥) and perpendicular (⊥) to the rubbing direction of PC. b) UV-vis absorption spectra after 10 minutes exposure to acetone. c)-d) Bright field images of the corresponding ZnPc/C*$_{60}$*-bilayer after 10 minutes exposure to acetone.*

lites exhibit a predominant in-plane orientation. To promote the crystallization of the β-phase, the prepared film was additionally treated by solvent-annealing. First, the films were exposed to dichloromethane (CH_2Cl_2), which is reported to induce a transition from the α to the β phase. Short exposure times (2-30 min) have not shown any affect on the structural properties of the films. After an additional exposure time of 120 min, the structure have changed to the β-phase, although at the high price of damaging and dissolving the film.

The same procedure was applied with another solvent, namely aceton. Figure 8.6 b shows the absorption spectrum for a film which was exposed for 10 minutes to aceton. Here, the peak positions of maximum absorption are shifted to higher values (650 nm and 752 nm), which are characteristic for the β-phase. Again, absorption measurements parallel and perpendicular to the rubbing direction of PC were performed. Contrary to the solvent-untreated film (Fig. 8.6) nearly no optical anisotropy was observed pointing to a loss of the in-plane order. The morphology observed in the bright field images (Fig. 8.6 c-d) further supports this result. The needle-like bundles are typically observed for β-crystallites of ZnPc.[63] As clearly visible, they do not show strongly pronounced in-plane order.

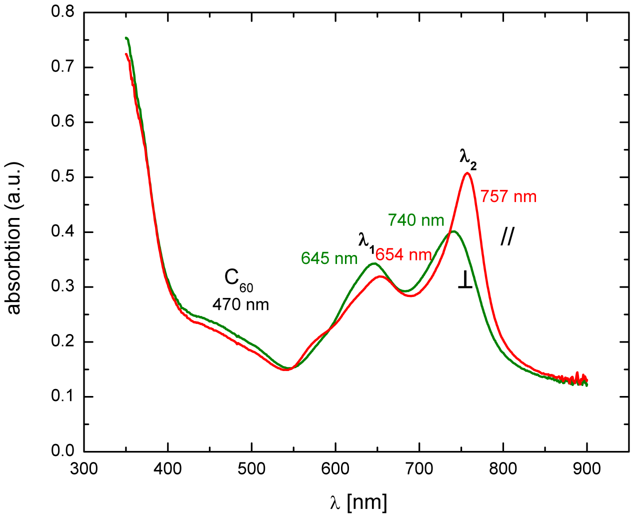

Figure 8.7: *a) UV-vis absorption spectra for a ZnPc/C_{60}-bilayer (d_{ZnPc} = 40nm, $t_{C_{60}}$=20 nm). The ZnPc layer was deposited at 200 °C, C_{60} layer at 115 °C. Absorption is measured parallel (‖) and perpendicular (⊥) to the rubbing direction of PC.*

In conclusion, we have observed that solvent-annealing using CH_2Cl_2 or acetone induces a phase transition from the α- to the β-phase, but at a high price of losing in-plane alignment. This is at variance with the report of Vergant et al. (2011).[63] Possible reasons for this may be the incorrect annealing time or the used solvent concentration.

8.3.3 Case 3 – ZnPc: T_{sub}= 200 °C, C_{60}: T_{sub}= 115 °C

To receive well-aligned β-ZnPc crystallites with in-plane order, T_{sub} was further increased to 200 °C during the deposition of the ZnPc layer. For the subsequent deposition of the C_{60} layer, the substrate was cooled down to 115 °C.

The absorption spectra for these films reveal that the α-phase is still present but predominately the β-phase is formed (Fig. 8.7). The absorption intensity measured for the direction parallel and perpendicular to the rubbing direction of the PC layer shows highly developed anisotropy, pointing towards an in-plane alignment of the β-ZnPc crystallites. Interestingly, parallel to the PC rubbing direction the intensity peaks are stronger shifted towards the β-phase (λ_1= 757 nm, λ_2= 654 nm) than in the direction perpendicular to it (λ_1= 740 nm, λ_2= 645 nm). This result suggests that the β-crystallites are preferentially formed parallel to the α-crystallites.

Bright field images (Fig. 8.8 a, b) confirm that the typical needle-like structures of the β-phase exhibit in-plane alignment which was missing in the case

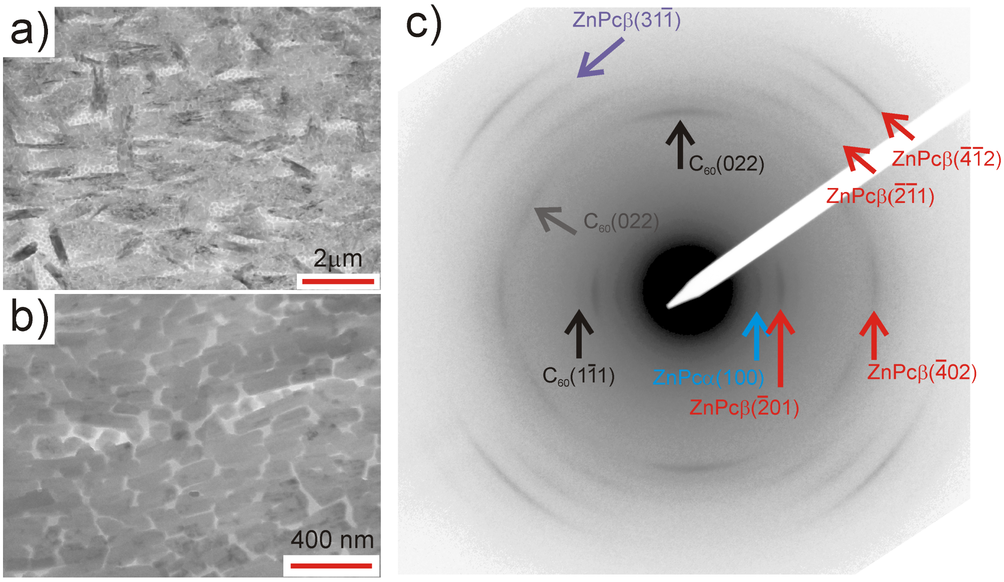

Figure 8.8: *a)-b) Bright field images of ZnPc/C_{60}-bilayer with t_{ZnPc}= 40 nm and $t_{C_{60}}$= 20 nm. The ZnPc layer was deposited at 200 °C and the C_{60} layer at 115 °C. c) The corresponding electron diffraction pattern.*

of the films exposed to acetone vapour (Fig. 8.6 c,d). Furthermore, in Fig. 8.8 b it is evident that the C_{60}-crystallites adopt the in-plane alignment of the ZnPc-crystallites. The morphology observed here is different to that in films of the same C_{60} thickness but deposited on top of the α-polymorph (see Fig. 8.2 c). On the α-ZnPc layer C_{60}, crystallites coalesce to elongated aggregates of an approximate length of 200 nm. The hemispherical shape of the individual crystallites forming aggregates is still visible. Contrary, on the β-ZnPc layer coherent crystallites with lengths of 200 nm are formed, which exhibit sharply defined contours. This behaviour can be linked to the structural properties of the β-crystallites. It has been observed that β-crystallites are formed only when α-crystallites have reached certain threshold dimensions (achieved by increasing the T_{sub}).[63] Therefore, β-crystallites exhibit inherently larger dimensions, in particular significantly larger widths than α-crystallites. This leads to better defined C_{60}-crystallites growing on top of it.

The corresponding electron diffraction (Fig. 8.8 c) clearly differs from that observed for films deposited at T_{sub}= 115 °C (s. Fig. 8.4 a). Still, there are diffraction contributions attributed to the (001) contact plane of the α-structure. Further, interplanar distances are observed which are characteristic for the β-polymorph. This diffraction pattern can be explained by two different contact planes being slightly tilted from the (001) net plane. The corresponding zone axes are [102] and [112] having a tilt angle of 9° and 4° in respect to the (001) lattice plane, respectively. These two orientations are discussed in detail in Ref. [63]. The remaining diffraction spots can be assigned to C_{60} crystallites with a ($21\bar{1}$) contact plane. However, reflexes attributed to {022}-lattice planes (d_{hkl} = 4.97 Å) appear at additional azimuthal orientations when compared to

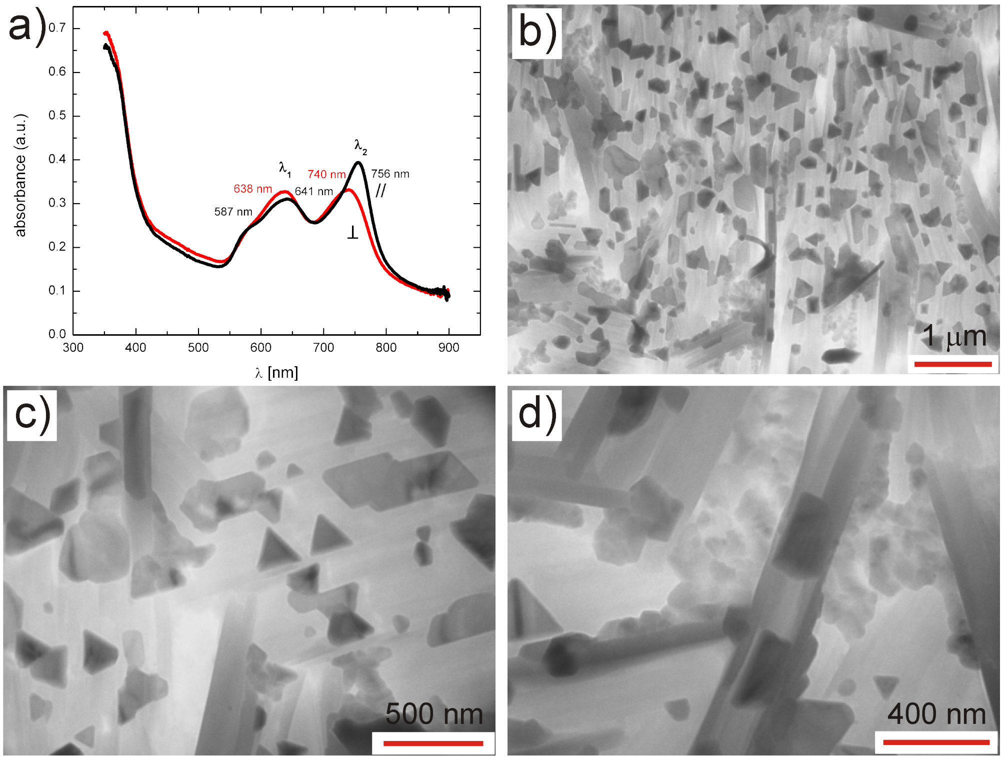

Figure 8.9: *a) UV-vis spectra for a ZnPc/C_{60} bilayer (t_{ZnPc}= 40 nm, $t_{C_{60}}$= 20 nm) both deposited at T_{sub}= 200 °C. Absorption is measured parallel (∥) and perpendicular (⊥) to the rubbing direction of PC. b)-d)Corresponding TEM bright field images showing the morphology of this film.*

Fig. 8.4 a. These spots can be explained with an additional domain of the $(21\bar{1})$ contact plane rotated by 60° in respect to the one present in case 1. Another possible explanation is given by an additional (111) contact plane giving rise to 6 {022} diffraction spots each separated by 60° from each other.

8.3.4 Case 4 – ZnPc: T_{sub}= 200 °C, C_{60}: T_{sub}= 200 °C

In the last case, the ZnPc-layer as well as the C_{60} layer were grown at a substrate temperature of 200 °C. As expected, the absorption spectra show predominately azimuthally aligned β-phase crystallites. (Fig. 8.9 a). In the corresponding bright field images (Fig. 8.9 b-d) the typical morphology of β-crystallites is clearly visible. The morphology of C_{60}, however, has dramatically changed. Here, the crystallites exhibit sharply defined contours which form geometrical shapes like triangles and rectangles.[202]

In the electron diffraction pattern (Fig. 8.10 a), the contributions of the ZnPc are the same as observed in case 3. They stemm from the α- and β- phase with the (001) contact planes. The remaining diffraction spots suggest that C_{60} crystallites exhibit a (111) contact plane as the diffraction spots characteristic for the $(21\bar{1})$ contact plane ({111}, {113}, see Table 8.2) are absent. Contrary

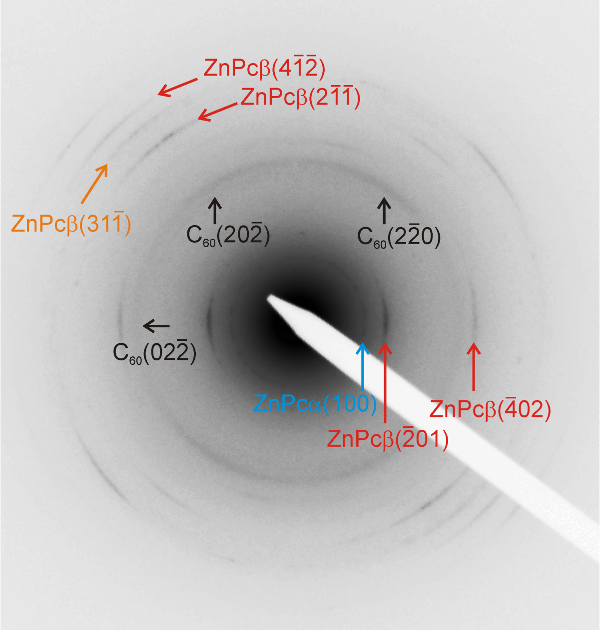

Figure 8.10: *Electron diffraction pattern of a ZnPc/C_{60} bilayer (t_{ZnPc} = 40 nm, $t_{C_{60}}$ = 20 nm) both deposited at T_{sub} = 200 °C.*

to the (21$\bar{1}$) contact plane (Fig. 8.10 b), the (111) contact plane (Fig. 8.10 c) is close-packed and thus leads to well-defined crystallites.

Our results are in agreement with studies of vapor-deposited C_{60} on various substrate surfaces,[73,74,202] where C_{60} molecules crystallizing in the fcc structure align with the (111) lattice plane parallel to substrate surface. Furthermore, the (truncated) triangular morphology is clearly related to crystallites exhibiting the (111) contact plane. In particular Yanagi et al. (1996)[202] observed that this is an orientation preferred at high substrate temperatures; for $T_{sub} \leq 100$ °C "particle like" morphologies are usually found while for $T_{sub} = 200$ °C triangular structures appear.

8.4 Summary

In conclusion, in the observed C_{60}/ZnPc-bilayer systems the structural properties of the C_{60} layer deposited on top of a ZnPc layer strongly depends on the polymorphic phase of the ZnPc crystallites as well as on the substrate temperature:

(i) ZnPc molecules deposited on a PC alignment layer at T_{sub}= 115 C° crystallize in the α-polymorph. They exhibit a unidirectional orientation with the (001) contact plane. Subsequent deposition of C_{60} molecules at the same substrate temperature leads to epitaxially aligned fcc crystallites exhibiting the $(21\bar{1})$ contact plane. This “unusual” contact plane is more favoured than the close-packed (111) lattice plane probably because it enables an epitaxial alignment in respect to the ZnPc-crystallites.

(ii) ZnPc layer prepared at T_{sub}= 170 C° is mainly composed of α-crystallites. Solvent annealing using dichloromethane and acetone induced a phase transition $\alpha \rightarrow \beta$, but the β-crystallites have not show pronounced in-plane orientation.

(iii) Deposition of ZnPc molecules at T_{sub}= 200 °C predominantly yields β-crystallites. They are oriented with the (001)-lattice plane nearly parallel to the substrate and show unidirectional in-plane alignment. C_{60} crystallizes in the fcc structure with the $(21\bar{1})$ contact plane. Additionally formed crystallites with the (111) contact planes cannot be excluded. The morphology of the C_{60}-crystallites is better defined than those grown on ZnPc α-crystallites.

(iv) When the ZnPc as well as the C_{60} layer are prepared at T_{sub}= 200°, the structural and morphological properties of the C_{60} crystallites significantly change. Here, we observe exclusively the (111) contact plane of the fcc structure. The morphology of the crystallites show sharply defined faces forming (truncated) triangles or rectangles.

Bibliography

(1) Hasegawa, T.; Takeya, J. *Science and Technology of Advanced Materials* **Apr. 2009**, *10*, 024314, DOI: 10.1088/1468-6996/10/2/024314.

(2) Norton, P.; Braggins, T.; Levinstein, H. *Physical Review B* **Dec. 1973**, *8*, 5632–5653, DOI: 10.1103/PhysRevB.8.5632.

(3) Dimitrakopoulos, C.; Malenfant, P. *Advanced Materials* **Jan. 2002**, *14*, 99–117, DOI: 10.1002/1521-4095(20020116)14:2<99::AID-ADMA99>3.0.CO;2-9.

(4) Murphy, A. R.; Fréchet, J. M. J. *Chemical Reviews* **Apr. 2007**, *107*, 1066–1096, DOI: 10.1021/cr0501386.

(5) Kelley, T. W.; Muyres, D.; Baude, P. F.; Smith, T. P.; Jones, T. D. In, Materials Research Society: Warrendale, Pa., 2003.

(6) Horowitz, G.; Garnier, F.; Yassar, A.; Hajlaoui, R.; Kouki, F. *Advanced Materials* **Jan. 1996**, *8*, 52–54, DOI: 10.1002/adma.19960080109.

(7) Bao, Z.; Lovinger, A. J.; Dodabalapur, A. *Applied Physics Letters* **1996**, *69*, 3066, DOI: 10.1063/1.116841.

(8) Haddon, R. C.; Perel, A. S.; Morris, R. C.; Palstra, T. T. M.; Hebard, A. F.; Fleming, R. M. *Applied Physics Letters* **1995**, *67*, 121, DOI: 10.1063/1.115503.

(9) Xue, J.; Uchida, S.; Rand, B. P.; Forrest, S. R. *Applied Physics Letters* **2004**, *85*, 5757, DOI: 10.1063/1.1829776.

(10) Peumans, P.; Forrest, S. R. *Applied Physics Letters* **2001**, *79*, 126, DOI: 10.1063/1.1384001.

(11) Peumans, P.; Uchida, S.; Forrest, S. R. *Nature* **Sept. 2003**, *425*, 158–162, DOI: 10.1038/nature01949.

(12) Horowitz, G. *Advanced Materials* **Mar. 1998**, *10*, 365–377, DOI: 10.1002/(SICI)1521-4095(199803)10:5<365::AID-ADMA365>3.0.CO;2-U.

(13) Kippelen, B.; Brédas, J.-L. *Energy & Environmental Science* **2009**, *2*, 251, DOI: 10.1039/b812502n.

(14) Coropceanu, V.; Cornil, J.; Silva Filho, D. A. da; Olivier, Y.; Silbey, R.; Brédas, J. *Chemical Reviews* **Apr. 2007**, *107*, 926–952, DOI: 10.1021/cr050140x.

(15) Facchetti, A. *Materials Today* **Mar. 2007**, *10*, 28–37, DOI: `10.1016/S1369-7021(07)70017-2`.

(16) Forrest, S. R.; Thompson, M. E. *Chemical Reviews* **Apr. 2007**, *107*, 923–925, DOI: `10.1021/cr0501590`.

(17) Koller, G.; Berkebile, S.; Krenn, J. R.; Netzer, F. P.; Oehzelt, M.; Haber, T.; Resel, R.; Ramsey, M. G. *Nano Letters* **June 2006**, *6*, 1207–1212, DOI: `10.1021/nl0606291`.

(18) *International Tables for Crystallography*, 1st ed., Chester, England; Vol. A, DOI: `10.1107/97809553602060000100`.

(19) Schwarzenbach, D., *Crystallography*; John Wiley: New York, 1996.

(20) Shmueli, U; International Union of Crystallography, *Theories and techniques of crystal structure determination*; Oxford University Press: Oxford; New York, 2007.

(21) Martin, R. M., *Electronic structure : basic theory and practical methods*; Cambridge University Press: New York, 2004.

(22) Sormann, H.; Schachinger, E. Theoretische Festkörperphysik, *Lecture notes.*, TU Graz, 2011.

(23) Massa, W., *Kristallstrukturbestimmung*; Teubner: Wiesbaden, 2007.

(24) Brock, C. P.; Dunitz, J. D. *Chemistry of Materials* **Aug. 1994**, *6*, 1118–1127, DOI: `10.1021/cm00044a010`.

(25) Kitajgorodskij, A. I. *Acta Crystallographica* **Apr. 1965**, *18*, 585–590, DOI: `10.1107/S0365110X65001391`.

(26) Kitajgorodskij, A. I., *Molecular Crystals and Molecules*; Academic Press, New York: 1973.

(27) Dauber, P.; Hagler, A. T. *Accounts of Chemical Research* **Apr. 1980**, *13*, 105–112, DOI: `10.1021/ar50148a002`.

(28) Desiraju, G. R.; Gavezzotti, A. *Acta Crystallographica Section B Structural Science* **Oct. 1989**, *45*, 473–482, DOI: `10.1107/S0108768189003794`.

(29) Braga, D.; Grepioni, F.; Maini, L.; Polito, M.; Rubini, K.; Chierotti, M.; Gobetto, R. *Chemistry - A European Journal* **Jan. 2009**, *15*, 1508–1515, DOI: `10.1002/chem.200800381`.

(30) Haleblian, J.; McCrone, W. *Journal of Pharmaceutical Sciences* **Aug. 1969**, *58*, 911–929, DOI: `10.1002/jps.2600580802`.

(31) Mangin, D.; Puel, F.; Veesler, S. *Organic Process Research & Development* **Nov. 2009**, *13*, 1241–1253, DOI: `10.1021/op900168f`.

(32) Bernstein, J *Journal of Physics D: Applied Physics* **Aug. 1993**, *26*, B66–B76, DOI: `10.1088/0022-3727/26/8B/010`.

(33) Price, S. L. *Accounts of Chemical Research* **Jan. 2009**, *42*, 117–126, DOI: `10.1021/ar800147t`.

(34) Price, C. P.; Grzesiak, A. L.; Matzger, A. J. *Journal of the American Chemical Society* **Apr. 2005**, *127*, 5512–5517, DOI: 10.1021/ja042561m.

(35) Ambrosch-Draxl, C.; Nabok, D.; Puschnig, P.; Meisenbichler, C. *New Journal of Physics* **Dec. 2009**, *11*, 125010, DOI: 10.1088/1367-2630/11/12/125010.

(36) Nývlt, J. *Crystal Research and Technology* **1995**, *30*, 443–449, DOI: 10.1002/crat.2170300402.

(37) Campbell, R. B.; Robertson, J. M.; Trotter, J. *Acta Crystallographica* **Mar. 1962**, *15*, 289–290, DOI: 10.1107/S0365110X62000699.

(38) Holmes, D.; Kumaraswamy, S.; Matzger, A.; Vollhardt, K. C. *Chemistry - A European Journal* **1999**, *5*, 3399–3412.

(39) Mattheus, C. C.; Dros, A. B.; Baas, J.; Meetsma, A.; Boer, J. L. d.; Palstra, T. T. M. *Acta Crystallographica Section C Crystal Structure Communications* **Aug. 2001**, *57*, 939–941, DOI: 10.1107/S010827010100703X.

(40) Siegrist, T.; Besnard, C.; Haas, S.; Schiltz, M.; Pattison, P.; Chernyshov, D.; Batlogg, B.; Kloc, C. *Advanced Materials* **Aug. 2007**, *19*, 2079–2082, DOI: 10.1002/adma.200602072.

(41) Schiefer, S.; Huth, M.; Dobrinevski, A.; Nickel, B. *Journal of the American Chemical Society* **Aug. 2007**, *129*, 10316–10317, DOI: 10.1021/ja0730516.

(42) Yoshida, H.; Inaba, K.; Sato, N. *Applied Physics Letters* **2007**, *90*, 181930, DOI: 10.1063/1.2736193.

(43) Nabok, D.; Puschnig, P.; Ambrosch-Draxl, C.; Werzer, O.; Resel, R.; Smilgies, D. *Physical Review B* **Dec. 2007**, *76*, DOI: 10.1103/PhysRevB.76.235322.

(44) Siegrist, T.; Kloc, C.; Schï¿½n, J.; Batlogg, B. *Angewandte Chemie International Edition* **2001**, *40*, 1732–1736.

(45) Della Valle, R. G.; Venuti, E.; Brillante, A.; Girlando, A. *The Journal of Chemical Physics* **2003**, *118*, 807, DOI: 10.1063/1.1527896.

(46) Drummy, L. F.; Martin, D. C. *Adv. Mater.* **2005**, *17*, 903.

(47) Moser, A.; Novák, J.; Flesch, H.; Djuric, T.; Werzer, O.; Haase, A.; Resel, R. *Applied Physics Letters* **2011**, *99*, 221911, DOI: 10.1063/1.3665188.

(48) Djuric, T.; Ules, T.; Flesch, H.; Plank, H.; Shen, Q.; Teichert, C.; Resel, R.; Ramsey, M. G. *Crystal Growth & Design* **Apr. 2011**, *11*, 1015–1020, DOI: 10.1021/cg101230j.

(49) Servet, B.; Horowitz, G.; Ries, S.; Lagorsse, O.; Alnot, P.; Yassar, A.; Deloffre, F.; Srivastava, P.; Hajlaoui, R. *Chemistry of Materials* **Oct. 1994**, *6*, 1809–1815, DOI: 10.1021/cm00046a039.

(50) Siegrist, T.; Fleming, R.; Haddon, R.; Laudise, R.; Lovinger, A.; Katz, H.; Bridenbaugh, P.; Davis, D. *Journal of Materials Research* **Sept. 1995**, *10*, 2170–2173, DOI: 10.1557/JMR.1995.2170.

(51) Horowitz, G.; Bachet, B.; Yassar, A.; Lang, P.; Demanze, F.; Fave, J.; Garnier, F. *Chemistry of Materials* **July 1995**, *7*, 1337–1341, DOI: 10.1021/cm00055a010.

(52) Baker, K; Fratini, A; Resch, T; Knachel, H; Adams, W; Socci, E; Farmer, B *Polymer* **Apr. 1993**, *34*, 1571–1587, DOI: 10.1016/0032-3861(93)90313-Y.

(53) Resel, R.; Koch, N.; Meghdadi, F.; Leising, G.; Athouel, L.; Froyer, G.; Hofer, F. *Crystal Research and Technology* **Jan. 2001**, *36*, 47–54, DOI: 10.1002/1521-4079(200101)36:1<47::AID-CRAT47>3.3.CO;2-O.

(54) Silvers, S. J.; Tulinsky, A. *Journal of the American Chemical Society* **June 1967**, *89*, 3331–3337, DOI: 10.1021/ja00989a036.

(55) Yanagi, H.; Takemoto, K.; Hayashi, S.; Ashida, M. *Journal of Crystal Growth* **Jan. 1990**, *99*, 1038–1043, DOI: 10.1016/S0022-0248(08)80077-2.

(56) Hamor, M. J.; Hamor, T. A.; Hoard, J. L. *Journal of the American Chemical Society* **May 1964**, *86*, 1938–1942, DOI: 10.1021/ja01064a008.

(57) Hazell, A. C. *Acta Crystallographica Section C Crystal Structure Communications* **May 1984**, *40*, 751–753, DOI: 10.1107/S010827018400559X.

(58) He, H. *Acta Crystallographica Section E Structure Reports Online* **Mar. 2007**, *63*, m976–m977, DOI: 10.1107/S1600536807008574.

(59) Guillaud, G.; Simon, J.; Germain, J. *Coordination Chemistry Reviews* **Dec. 1998**, *178-180*, 1433–1484, DOI: 10.1016/S0010-8545(98)00177-5.

(60) Janczak, J.; Kubiak, R. *Journal of Alloys and Compounds* **Dec. 1992**, *190*, 121–124, DOI: 10.1016/0925-8388(92)90187-E.

(61) Brown, C. J. *Journal of the Chemical Society A: Inorganic, Physical, Theoretical* **1968**, 2494, DOI: 10.1039/j19680002494.

(62) Hoshino, A.; Takenada, Y.; Miyaji, H. *Acta. Crystallogr. B* **2003**, *B59*, 393.

(63) Vergnat, C.; Landais, V.; Legrand, J.-F.; Brinkmann, M. *Macromolecules* **2011**, *44*, 3817–3827, DOI: 10.1021/ma200350v.

(64) Robertson, J. M. *Journal of the Chemical Society (Resumed)* **1936**, 1195, DOI: 10.1039/jr9360001195.

(65) J., B. C. *J. Chem. Soc.* **1968**, 2488.

(66) R., S. W. *J. Am. Chem. Soc.* **1977**, *99*, 1101.

(67) Zugenmaier, P; Bluhm, T.; Deslandes, Y; Orts, W.; Hamer, G. English *JOURNAL OF MATERIALS SCIENCE* **1997**, *32*, 5561–5568, DOI: {10.1023/A:1018672423851}.

(68) Krätschmer, W.; Lamb, L. D.; Fostiropoulos, K.; Huffman, D. R. *Nature* **Sept. 1990**, *347*, 354–358, DOI: 10.1038/347354a0.

(69) Hawkins, J. M.; Lewis, T. A.; Loren, S. D.; Meyer, A.; Heath, J. R.; Saykally, R. J.; Hollander, F. J. *Journal of the Chemical Society, Chemical Communications* **1991**, 775, DOI: 10.1039/c39910000775.

(70) Bürgi, H.-B.; Blanc, E.; Schwarzenbach, D.; Liu, S.; Lu, Y.-j.; Kappes, M. M.; Ibers, J. A. *Angewandte Chemie International Edition in English* **1992**, *31*, 640–643, DOI: 10.1002/anie.199206401.

(71) Fleming, R. M.; Siegrist, T.; Marsh, P. M.; Hessen, B.; Kortan, A. R.; Murphy, D. W.; Haddon, R. C.; Tycko, R.; Dabbagh, G.; Mujsce, A. M.; Kaplan, M. L.; Zahurak, S. M. *MRS Proceedings* **Feb. 2011**, *206*, DOI: 10.1557/PROC-206-691.

(72) Li, Z.; Fagan, P. J. *Chemical Physics Letters* **July 1992**, *194*, 461–466, DOI: 10.1016/0009-2614(92)86083-T.

(73) Ichihashi, T.; Tanigaki, K.; Ebbesen, T. W.; Kuroshima, S.; Iijima, S. *Chemical Physics Letters* **Mar. 1992**, *190*, 179–183, DOI: 10.1016/0009-2614(92)85322-2.

(74) Yanagi, H.; Sasaki, T. *Applied Physics Letters* **1994**, *65*, 1222, DOI: 10.1063/1.112949.

(75) Boer, J. L. de; Smaalen, S. van; Petricek, V.; DusekP, M.; Verheijen, M. A.; Meijer, G. *Chemical Physics Letters* **Mar. 1994**, *219*, 469–472, DOI: 10.1016/0009-2614(94)00110-3.

(76) Herman, M. A.; Sitter, H., *Molecular beam epitaxy : fundamentals and current status*; Springer: Berlin; New York, 1996.

(77) Hooks, D. E.; Fritz, T.; Ward, M. D. *Advanced Materials* **Feb. 2001**, *13*, 227–241, DOI: 10.1002/1521-4095(200102)13:4<227::AID-ADMA227>3.0.CO;2-P.

(78) Mannsfeld, S.; Leo, K.; Fritz, T. *Physical Review Letters* **Feb. 2005**, *94*, DOI: 10.1103/PhysRevLett.94.056104.

(79) Resel, R.; Haber, T.; Lengyel, O.; Sitter, H.; Balzer, F.; Rubahn, H. *Surface and Interface Analysis* **Sept. 2009**, *41*, 764–770, DOI: 10.1002/sia.3095.

(80) Koini, M; Haber, T; Werzer, O; Berkebile, S; Koller, G; Oehzelt, M; Ramsey, M; Resel, R *Thin Solid Films* **Nov. 2008**, *517*, 483–487, DOI: 10.1016/j.tsf.2008.06.053.

(81) Sitter, H.; Andreev, A.; Matt, G.; Sariciftci, N. *Synthetic Metals* **June 2003**, *138*, 9–13, DOI: 10.1016/S0379-6779(02)01306-1.

(82) Gusenleitner, S., *Geometric and Electronic Structure of Tetraphenylporphyrin and Tetraphenylporphyrin Pt(II) on Cu(110) and Cu(110)p(2x1)O*, University Graz, 2009.

(83) Djuric, T., *Structural Properties of Rubrene Thin Films Grown on Mica Surfaces*, Graz University of Technology, 2008.

(84) Djuric, T.; Thierry, A.; Grogger, W.; Abd Al-Baqi, S.; Sitter, H.; Resel, R. *Physica E: Low-dimensional Systems and Nanostructures* **Sept. 2009**, *41*, 1718–1722, DOI: 10.1016/j.physe.2009.06.012.

(85) Fultz, B.; Howe, J. M., *Transmission electron microscopy and diffractometry of materials : with numerous exercises*; Springer: Berlin [u.a.], 2005.

(86) Virkar, A. A.; Mannsfeld, S.; Bao, Z.; Stingelin, N. *Advanced Materials* **Sept. 2010**, *22*, 3857–3875, DOI: 10.1002/adma.200903193.

(87) Bernstein, J *Journal of Physics D: Applied Physics* **Aug. 1993**, *26*, B66–B76, DOI: 10.1088/0022-3727/26/8B/010.

(88) Hamor, M. J.; Hamor, T. A.; Hoard, J. L. *Journal of the American Chemical Society* **May 1964**, *86*, 1938–1942, DOI: 10.1021/ja01064a008.

(89) Fleischer, E. B.; Miller, C. K.; Webb, L. E. *Journal of the American Chemical Society* **June 1964**, *86*, 2342–2347, DOI: 10.1021/ja01066a009.

(90) Kwong, R. C.; Sibley, S.; Dubovoy, T.; Baldo, M.; Forrest, S. R.; Thompson, M. E. *Chemistry of Materials* **Dec. 1999**, *11*, 3709–3713, DOI: 10.1021/cm9906248.

(91) Che, C.-M.; Hou, Y.-J.; Chan, M. C. W.; Guo, J.; Liu, Y.; Wang, Y. *Journal of Materials Chemistry* **2003**, *13*, 1362, DOI: 10.1039/b212204a.

(92) Walter, M. G.; Rudine, A. B.; Wamser, C. C. *Journal of Porphyrins and Phthalocyanines* **2010**, *14*, 759, DOI: 10.1142/S1088424610002689.

(93) Bessho, T.; Zakeeruddin, S. M.; Yeh, C.-Y.; Diau, E. W.-G.; Grï¿½tzel, M. *Angewandte Chemie International Edition* **Sept. 2010**, *49*, 6646–6649, DOI: 10.1002/anie.201002118.

(94) Chen, Q.; McDowall, A. J.; Richardson, N. V. *Langmuir* **Nov. 2003**, *19*, 10164–10171, DOI: 10.1021/la035052r.

(95) Checcoli, P *Synthetic Metals* **June 2003**, *138*, 261–266, DOI: 10.1016/S0379-6779(02)01308-5.

(96) Scudiero, L.; Barlow, D. E.; Mazur, U.; Hipps, K. W. *Journal of the American Chemical Society* **May 2001**, *123*, 4073–4080, DOI: 10.1021/ja0100726.

(97) Buchner, F.; Schwald, V.; Comanici, K.; Steinrï¿½ck, H.-P.; Marbach, H. *ChemPhysChem* **Feb. 2007**, *8*, 241–243, DOI: 10.1002/cphc.200600698.

(98) Auwärter, W.; Weber-Bargioni, A.; Brink, S.; Riemann, A.; Schiffrin, A.; Ruben, M.; Barth, J. V. *ChemPhysChem* **Feb. 2007**, *8*, 250–254, DOI: 10.1002/cphc.200600675.

(99) Jung, T. A.; Schlittler, R. R.; Gimzewski, J. K. *Nature* **Apr. 1997**, *386*, 696–698, DOI: 10.1038/386696a0.

(100) Moresco, F; Meyer, G.; Rieder, K.; Ping, J.; Tang, H.; Joachim, C. *Surface Science* **Feb. 2002**, *499*, 94–102, DOI: 10.1016/S0039-6028(01)01803-9.

(101) Buchner, F.; Kellner, I.; Hieringer, W.; Görling, A.; Steinrück, H.-P.; Marbach, H. *Physical Chemistry Chemical Physics* **2010**, *12*, 13082, DOI: 10.1039/c004551a.

(102) Donovan, P.; Robin, A.; Dyer, M. S.; Persson, M.; Raval, R. *Chemistry - A European Journal* **Sept. 2010**, *16*, 11641–11652, DOI: 10.1002/chem.201001776.

(103) Barlow, D. E.; Scudiero, L.; Hipps, K. W. *Langmuir* **May 2004**, *20*, 4413–4421, DOI: 10.1021/la0358791.

(104) Buchner, F.; Comanici, K.; Jux, N.; Steinrï¿½ck, H.; Marbach, H. *Journal of Physical Chemistry C* **Sept. 2007**, *111*, 13531–13538, DOI: 10.1021/jp074448z.

(105) Yanagiya, S.-i.; Wakamatsu, H.; Nishikata, O.; Inoue, T. *Japanese Journal of Applied Physics* **Nov. 2004**, *43*, 7722–7724, DOI: 10.1143/JJAP.43.7722.

(106) Haber, T.; Oehzelt, M.; Resel, R.; Andreev, A.; Thierry, A.; Sitter, H.; Smilgies, D.; Schaffer, B.; Grogger, W.; Resel, R. *Journal of Nanoscience and Nanotechnology* **Mar. 2006**, *6*, 698–703, DOI: 10.1166/jnn.2006.131.

(107) Kern, K.; Niehus, H.; Schatz, A.; Zeppenfeld, P.; Goerge, J.; Comsa, G. *Physical Review Letters* **Aug. 1991**, *67*, 855–858, DOI: 10.1103/PhysRevLett.67.855.

(108) Salzmann, I.; Resel, R. *Journal of Applied Crystallography* **Nov. 2004**, *37*, 1029–1033, DOI: 10.1107/S002188980402165X.

(109) Kraus, W.; Nolzeb, G. *Journal of Applied Crystallography* **June 1996**, *29*, 301–303, DOI: 10.1107/S0021889895014920.

(110) Lutterotti, L.; Bortolotti, M.; Ischia, G.; Lonardelli, I.; Wenk, H. *Zeitschrift für Kristallographie Supplements* **Nov. 2007**, *2007*, 125–130, DOI: 10.1524/zksu.2007.2007.suppl_26.125.

(111) Zuo, J.; Mabon, J. *Microsc Microanal 10(Suppl 2)* **2004**.

(112) Klapetek, P; Necas, D; Anderson, C, *Gwyddion user guide (2011)*.

(113) Hayashi, S; Ikuno, H; Yanagi, H; Ashida, M *Journal of Crystal Growth* **Sept. 1992**, *123*, 35–41, DOI: 10.1016/0022-0248(92)90007-6.

(114) Ashida, M.; Yanagi, H.; Hayashi, S.; Takemoto, K. *Acta Crystallographica Section B Structural Science* **Feb. 1991**, *47*, 87–91, DOI: 10.1107/S0108768190008904.

(115) Yanagi, H.; Okamoto, S. *Applied Physics Letters* **1997**, *71*, 2563, DOI: 10.1063/1.119331.

(116) Webb, L. E.; Fleischer, E. B. *The Journal of Chemical Physics* **1965**, *43*, 3100, DOI: 10.1063/1.1697283.

(117) Becker, E. D.; Bradley, R. B.; Watson, C. J. *Journal of the American Chemical Society* **Sept. 1961**, *83*, 3743–3748, DOI: 10.1021/ja01479a002.

(118) Hayashi, S; Yanagi, H; Ueda, Y; Fujiyoshi, Y; Ashida, M *Ultramicroscopy* **Feb. 1993**, *49*, 308–317, DOI: 10.1016/0304-3991(93)90237-R.

(119) Yanagi, H; Shibutani, T. *Thin Solid Films* **Aug. 2003**, *438-439*, 33–38, DOI: 10.1016/S0040-6090(03)00748-X.

(120) Last, J. A.; Hooks, D. E.; Hillier, A. C.; Ward, M. D. *The Journal of Physical Chemistry B* **Aug. 1999**, *103*, 6723–6733, DOI: 10.1021/jp984101j.

(121) Teugels, L. G.; Avila-Bront, L. G.; Sibener, S. J. *The Journal of Physical Chemistry C* **Feb. 2011**, *115*, 2826–2834, DOI: 10.1021/jp1108398.

(122) Lutz, M; Feenstra, R; Mooney, P; Tersoff, J; Chu, J *Surface Science* **Sept. 1994**, *316*, L1075–L1080, DOI: 10.1016/0039-6028(94)91208-4.

(123) Teichert, C *Physics Reports* **Aug. 2002**, *365*, 335–432, DOI: 10.1016/S0370-1573(02)00009-1.

(124) Klauk, H.; Gundlach, D.; Nichols, J.; Jackson, T. *IEEE TRANSACTIONS ON ELECTRON DEVICES* **June 1999**, *46*.

(125) Nelson, S. F.; Lin, Y.; Gundlach, D. J.; Jackson, T. N. *Applied Physics Letters* **1998**, *72*, 1854, DOI: 10.1063/1.121205.

(126) Minakata, T.; Imai, H.; Ozaki, M.; Saco, K. *Journal of Applied Physics* **1992**, *72*, 5220, DOI: 10.1063/1.352004.

(127) Laquindanum, J. G.; Katz, H. E.; Lovinger, A. J.; Dodabalapur, A. *Chemistry of Materials* **Jan. 1996**, *8*, 2542–2544, DOI: 10.1021/cm9603664.

(128) Dimitrakopoulos, C. D.; Brown, A. R.; Pomp, A. *Journal of Applied Physics* **1996**, *80*, 2501, DOI: 10.1063/1.363032.

(129) Ruiz, R.; Mayer, A. C.; Malliaras, G. G.; Nickel, B.; Scoles, G.; Kazimirov, A.; Kim, H.; Headrick, R. L.; Islam, Z. *Applied Physics Letters* **2004**, *85*, 4926, DOI: 10.1063/1.1826229.

(130) Haas, U.; Haase, A.; Maresch, H.; Stadlober, B.; Leising, G. *2004 4TH IEEE INTERNATIONAL CONFERENCE ON POLYMERS AND ADHESIVES IN MICROELECTRONICS AND PHOTONICS* **2004**.

(131) Jentzsch, T; Juepner, H.; Brzezinka, K.-W.; Lau, A *Thin Solid Films* **Mar. 1998**, *315*, 273–280, DOI: 10.1016/S0040-6090(97)00797-9.

(132) Söhnchen, S.; Lukas, S.; Witte, G. *The Journal of Chemical Physics* **2004**, *121*, 525, DOI: 10.1063/1.1760076.

(133) Mannsfeld, S. C. B.; Virkar, A.; Reese, C.; Toney, M. F.; Bao, Z. *Advanced Materials* **June 2009**, *21*, 2294–2298, DOI: 10.1002/adma.200803328.

(134) Bouchoms, I.; Schoonveld, W.; Vrijmoeth, J; Klapwijk, T. *Synthetic Metals* **July 1999**, *104*, 175–178, DOI: 10.1016/S0379-6779(99)00050-8.

(135) Kalihari, V.; Ellison, D. J.; Haugstad, G.; Frisbie, C. D. *Advanced Materials* **Aug. 2009**, *21*, 3092–3098, DOI: 10.1002/adma.200900362.

(136) Amassian, A.; Pozdin, V. A.; Desai, T. V.; Hong, S.; Woll, A. R.; Ferguson, J. D.; Brock, J. D.; Malliaras, G. G.; Engstrom, J. R. *Journal of Materials Chemistry* **2009**, *19*, 5580, DOI: 10.1039/b907947e.

(137) Heringdorf, F. J. Meyer zu; Reuter, M. C.; Tromp, R. M. *Nature* **Aug. 2001**, *412*, PMID: 11484047, 517–520, DOI: 10.1038/35087532.

(138) France, C. B.; Schroeder, P. G.; Parkinson, B. A. *Nano Letters* **July 2002**, *2*, 693–696, DOI: 10.1021/nl025567n.

(139) Lukas, S.; Söhnchen, S.; Witte, G.; Wöll, C. *ChemPhysChem* **Feb. 2004**, *5*, 266–270, DOI: 10.1002/cphc.200300892.

(140) Yamane, H.; Yoshimura, D.; Kawabe, E.; Sumii, R.; Kanai, K.; Ouchi, Y.; Ueno, N.; Seki, K. *Physical Review B* **Oct. 2007**, *76*, DOI: 10.1103/PhysRevB.76.165436.

(141) Müller, K.; Kara, A.; Kim, T.; Bertschinger, R.; Scheybal, A.; Osterwalder, J.; Jung, T. *Physical Review B* **June 2009**, *79*, DOI: 10.1103/PhysRevB.79.245421.

(142) Martínez-Blanco, J.; Ruiz-Osés, M.; Joco, V.; Sayago, D. I.; Segovia, P.; Michel, E. G. *Journal of Vacuum Science & Technology B: Microelectronics and Nanometer Structures* **2009**, *27*, 863, DOI: 10.1116/1.3013855.

(143) Nabok, D.; Puschnig, P.; Ambrosch-Draxl, C. *Physical Review B* **June 2008**, *77*, DOI: 10.1103/PhysRevB.77.245316.

(144) Berkebile, S.; Koller, G.; Fleming, A.; Puschnig, P.; Ambrosch-Draxl, C.; Emtsev, K.; Seyller, T.; Riley, J.; Ramsey, M. *Journal of Electron Spectroscopy and Related Phenomena* **Aug. 2009**, *174*, 22–27, DOI: 10.1016/j.elspec.2009.04.001.

(145) Ules, T., *The initial stages of growth of conjugated molecules*, Diploma Thesis, KFU Graz, 2009.

(146) Oehzelt, M.; Resel, R.; Suess, C.; Friedlein, R.; Salaneck, W. R. *The Journal of Chemical Physics* **2006**, *124*, 054711, DOI: 10.1063/1.2150826.

(147) Kiyomura, T; Nemoto, T; Yoshida, K; Minari, T; Kurata, H; Isoda, S *Thin Solid Films* **Oct. 2006**, *515*, 810–813, DOI: 10.1016/j.tsf.2005.12.228.

(148) Al-Mahboob, A.; Sadowski, J.; Nishihara, T.; Fujikawa, Y.; Xue, Q.; Nakajima, K.; Sakurai, T. *Surface Science* **Mar. 2007**, *601*, 1304–1310, DOI: 10.1016/j.susc.2006.12.064.

(149) Irie, S *Applied Surface Science* **Apr. 1997**, *113-114*, 310–315, DOI: 10.1016/S0169-4332(96)00950-6.

(150) Mannsfeld, S.; Fritz, T. *Physical Review B* **June 2005**, *71*, DOI: 10.1103/PhysRevB.71.235405.

(151) Zhang, F.; Xu, Z.; Liu, X.; Zhao, S.; Lu, L.; Wang, Y.; Xu, X. *Superlattices and Microstructures* **June 2009**, *45*, 612–617, DOI: 10.1016/j.spmi.2009.03.007.

(152) Fleming, A. J.; Netzer, F. P.; Ramsey, M. G. *Journal of Physics: Condensed Matter* **Nov. 2009**, *21*, 445003, DOI: 10.1088/0953-8984/21/44/445003.

(153) Oehzelt, M.; Grill, L.; Berkebile, S.; Koller, G.; Netzer, F. P.; Ramsey, M. G. *ChemPhysChem* **Aug. 2007**, *8*, 1707–1712, DOI: 10.1002/cphc.200700357.

(154) *Organic Nanostructures for Next Generation Devices*; Al-Shamery, K., Rubahn, H., Sitter, H., Eds.; Springer Berlin Heidelberg: Berlin, Heidelberg, 2008; Vol. 101.

(155) Berkebile, S; Koller, G; Hlawacek, G; Teichert, C; Netzer, F; Ramsey, M *Surface Science* **Dec. 2006**, *600*, L313–L317, DOI: 10.1016/j.susc.2006.06.044.

(156) Kury, P; Roos, K.; Thien, D.; Möllenbeck, S; Wall, D; Hoegen, M. Horn-von; Heringdorf, F. Meyer zu *Organic Electronics* **2008**, 461–465, DOI: 10.1016/j.orgel.2008.02.006.

(157) Leising, G.; Tasch, S.; Meghdadi, F.; Athouel, L.; Froyer, G.; Scherf, U. *Synthetic Metals* **Aug. 1996**, *81*, 185–189, DOI: 10.1016/S0379-6779(96)03751-4.

(158) Noda, T.; Ogawa, H.; Noma, N.; Shirota, Y. *Journal of Materials Chemistry* **1999**, *9*, 2177–2181, DOI: 10.1039/a902800e.

(159) Mikami, T.; Yanagi, H. *Applied Physics Letters* **1998**, *73*, 563, DOI: 10.1063/1.121856.

(160) Katz, H. E. *Journal of Materials Chemistry* **1997**, *7*, 369–376, DOI: 10.1039/a605274f.

(161) Simbrunner, C.; Nabok, D.; Hernandez-Sosa, G.; Oehzelt, M.; Djuric, T.; Resel, R.; Romaner, L.; Puschnig, P.; Ambrosch-Draxl, C.; Salzmann, I.; Schwabegger, G.; Watzinger, I.; Sitter, H. *Journal of the American Chemical Society* **Mar. 2011**, *133*, 3056–3062, DOI: 10.1021/ja109729e.

(162) Plank, H.; Resel, R.; Purger, S.; Keckes, J.; Thierry, A.; Lotz, B.; Andreev, A.; Sariciftci, N.; Sitter, H. *Physical Review B* **Nov. 2001**, *64*, DOI: 10.1103/PhysRevB.64.235423.

(163) Plank, H; Resel, R.; Andreev, A; Sariciftci, N.; Sitter, H. *Journal of Crystal Growth* **Apr. 2002**, *237-239*, 2076–2081, DOI: 10.1016/S0022-0248(01)02313-2.

(164) Plank, H; Resel, R.; Sitter, H.; Andreev, A; Sariciftci, N.; Hlawacek, G.; Teichert, C.; Thierry, A.; Lotz, B. *Thin Solid Films* **Oct. 2003**, *443*, 108–114, DOI: `10.1016/S0040-6090(03)01021-6`.

(165) Lengyel, O.; Satka, A.; Haber, T.; Kovac, J.; Sitter, H.; Resel, R. *Crystal Research and Technology* **Jan. 2008**, *43*, 44–49, DOI: `10.1002/crat.200711047`.

(166) Müllegger, S; Winkler, A *Surface Science* **Mar. 2006**, *600*, 1290–1299, DOI: `10.1016/j.susc.2006.01.018`.

(167) Balzer, F.; Rubahn, H. *Applied Physics Letters* **2001**, *79*, 3860, DOI: `10.1063/1.1424071`.

(168) Piaggi, A.; Lanzani, G.; Bongiovanni, G.; Mura, A.; Graupner, W.; Meghdadi, F.; Leising, G.; Nisoli, M. *Physical Review B* **Oct. 1997**, *56*, 10133–10137, DOI: `10.1103/PhysRevB.56.10133`.

(169) Quochi, F. *Journal of Optics* **Feb. 2010**, *12*, 024003, DOI: `10.1088/2040-8978/12/2/024003`.

(170) Balzer, F.; Rubahn, H. *Advanced Functional Materials* **Jan. 2005**, *15*, 17–24, DOI: `10.1002/adfm.200400367`.

(171) Biscarini, F.; Zamboni, R.; Samorí, P.; Ostoja, P.; Taliani, C. *Physical Review B* **Nov. 1995**, *52*, 14868–14877, DOI: `10.1103/PhysRevB.52.14868`.

(172) Kankate, L.; Balzer, F.; Niehus, H.; Rubahn, H. *Thin Solid Films* **Nov. 2009**, *518*, 130–137, DOI: `10.1016/j.tsf.2009.06.003`.

(173) Viville, P.; Lazzaroni, R.; Luc Brédas, J.; Moretti, P.; Samorí, P.; Biscarini, F. *Advanced Materials* **Jan. 1998**, *10*, 57–60, DOI: `10.1002/(SICI)1521-4095(199801)10:1<57::AID-ADMA57>3.0.CO;2-0`.

(174) Simbrunner, C.; Hernandez-Sosa, G.; Oehzelt, M.; Djuric, T.; Salzmann, I.; Brinkmann, M.; Schwabegger, G.; Watzinger, I.; Sitter, H.; Resel, R. *Physical Review B* **Mar. 2011**, *83*, DOI: `10.1103/PhysRevB.83.115443`.

(175) Campione, M.; Raimondo, L.; Moret, M.; Campiglio, P.; Fumagalli, E.; Sassella, A. *Chemistry of Materials* **Oct. 2009**, *21*, 4859–4867, DOI: `10.1021/cm901463u`.

(176) Moret, M.; Borghesi, A.; Campione, M.; Fumagalli, E.; Raimondo, L.; Sassella, A. *Crystal Research and Technology* **Aug. 2011**, *46*, 827–832, DOI: `10.1002/crat.201000581`.

(177) Simbrunner, C.; Quochi, F.; Hernandez-Sosa, G.; Oehzelt, M.; Resel, R.; Hesser, G.; Arndt, M.; Saba, M.; Mura, A.; Bongiovanni, G.; Sitter, H. *ACS Nano* **Oct. 2010**, *4*, 6244–6250, DOI: `10.1021/nn1018889`.

(178) Simbrunner, C. et al. *ACS submitted* **2012**, *XX*.

(179) Hinderhofer, A.; Frank, C.; Hosokai, T.; Resta, A.; Gerlach, A.; Schreiber, F. *The Journal of Chemical Physics* **2011**, *134*, 104702, DOI: `10.1063/1.3557476`.

(180) Jones, R, *Soft condensed matter*; Oxford University Press: Oxford, 2002.

(181) Stølen, S., *Chemical thermodynamics of materials : macroscopic and microscopic aspects*; J. Wiley: Hoboken NJ, 2004.

(182) Salzmann, I.; Duhm, S.; Heimel, G.; Oehzelt, M.; Kniprath, R.; Johnson, R. L.; Rabe, J. P.; Koch, N. *Journal of the American Chemical Society* **Oct. 2008**, *130*, 12870–12871, DOI: 10.1021/ja804793a.

(183) Salzmann, I.; Duhm, S.; Heimel, G.; Rabe, J. P.; Koch, N.; Oehzelt, M.; Sakamoto, Y.; Suzuki, T. *Langmuir* **July 2008**, *24*, 7294–7298, DOI: 10.1021/la800606h.

(184) Callister, W. D., *Materials science and engineering : an introduction*; John Wiley & Sons: New York, 2007.

(185) Vegard, L. *Zeitschrift für Physik* **July 1931**, *71*, 465–472, DOI: 10.1007/BF01340080.

(186) Vogel, J.; Salzmann, I.; Duhm, S.; Oehzelt, M.; Rabe, J. P.; Koch, N. *Journal of Materials Chemistry* **2010**, *20*, 4055, DOI: 10.1039/b927594k.

(187) Kankate, L.; Balzer, F.; Niehus, H.; Rubahn, H. *The Journal of Chemical Physics* **2008**, *128*, 084709, DOI: 10.1063/1.2839296.

(188) Lecláre, P.; Surin, M.; Viville, P.; Lazzaroni, R.; Kilbinger, A. F. M.; Henze, O.; Feast, W. J.; Cavallini, M.; Biscarini, F.; Schenning, A. P. H. J.; Meijer, E. W. *Chemistry of Materials* **Nov. 2004**, *16*, 4452–4466, DOI: 10.1021/cm049673x.

(189) Dissado, L. A. *Journal of Physics C: Solid State Physics* **Jan. 1974**, *7*, 463–480, DOI: 10.1088/0022-3719/7/2/025.

(190) Hutchison, C. A.; Mangum, B. W. *The Journal of Chemical Physics* **1961**, *34*, 908, DOI: 10.1063/1.1731693.

(191) Sacconi, L; Ciampolini, M; Speroni, G. *Journal of the American Chemical Society* **1965**, *87*, 3102–3106.

(192) Vaida, M.; Shimon, L. J. W.; Weisinger-Lewin, Y.; Frolow, F.; Lahav, M.; Leiserowitz, L.; Mcmullan, R. K. *Science* **Sept. 1988**, *241*, 1475–1479, DOI: 10.1126/science.241.4872.1475.

(193) Xiao, K.; Liu, Y.; Yu, G.; Zhu, D. *Applied Physics A: Materials Science & Processing* **Aug. 2003**, *77*, 367–370, DOI: 10.1007/s00339-003-2169-6.

(194) Tang, C. W. *Applied Physics Letters* **1986**, *48*, 183, DOI: 10.1063/1.96937.

(195) Mori, T.; Mitsuoka, T.; Ishii, M.; Fujikawa, H.; Taga, Y. *Applied Physics Letters* **2002**, *80*, 3895, DOI: 10.1063/1.1481540.

(196) Qiu, Y.; Gao, Y.; Wei, P.; Wang, L. *Applied Physics Letters* **2002**, *80*, 2628, DOI: 10.1063/1.1468894.

(197) Pettersson, L. A. A.; Roman, L. S.; Inganaís, O. *Journal of Applied Physics* **1999**, *86*, 487, DOI: 10.1063/1.370757.

(198) Gebeyehu, D.; Brabec, C.; Padinger, F.; Fromherz, T.; Hummelen, J.; Badt, D.; Schindler, H.; Sariciftci, N. *Synthetic Metals* **Mar. 2001**, *118*, 1–9, DOI: `10.1016/S0379-6779(00)00276-9`.

(199) Shaheen, S. E.; Brabec, C. J.; Sariciftci, N. S.; Padinger, F.; Fromherz, T.; Hummelen, J. C. *Applied Physics Letters* **2001**, *78*, 841, DOI: `10.1063/1.1345834`.

(200) Brinkmann, M.; Pratontep, S.; Chaumont, C.; Wittmann, J. *Macromolecules* **Dec. 2007**, *40*, 9420–9426, DOI: `10.1021/ma702227f`.

(201) Vergnat, C.; Uttiya, S.; Pratontep, S.; Kerdcharoen, T.; Legrand, J.; Brinkmann, M. *Synthetic Metals* **Feb. 2011**, *161*, 251–258, DOI: `10.1016/j.synthmet.2010.11.029`.

(202) Yanagi, H.; Doumi, S.; Sasaki, T.; Tada, H. *Journal of Applied Physics* **1996**, *80*, 4990, DOI: `10.1063/1.363543`.